Transverse Confinement in Lasers

Graeme Kerr Harkness

Thesis submitted for the degree of

Doctor of Philosophy

in the Department of Physics and Applied Physics

University of Strathclyde

September 29, 1994

Abstract

We divide lasers into two classes, depending on their aspect ratio : defined to be the ratio of the width of the transverse beam to the characteristic scale of the pattern comprising it. We have studied, theoretically, the transition from large to small aspect ratio systems by considering the effects of transverse boundaries on the pattern forming behaviour of the laser equations.

Specifically, we have considered the effects of transverse reflecting boundaries, gain guiding, and curved cavity mirrors on the travelling waves found in the infinitely extended system. We have shown that there is a transition between travelling wave behaviour and a boundary dominated régime and have gone some way to characterising this transition by using the pump strength as a parameter.

As a special case we have considered gain guiding in a solid state microchip laser and have shown that such a confinement mechanism provides a very effective suppression for higher order transverse modes.

Acknowledgments

So many people have helped me throughout the course of my Ph.D it would be impossible to mention them all by name.

Special thanks go to my parents for their tireless support and encouragement throughout my years of education, to my friends in the department and all over the world, and to Willie Firth, my supervisor, for all his support and good ideas!

Contents

Chapter 1

Introduction

The theory of transverse effects in lasers falls into two main camps. The distinction is provided by the concept of *aspect ratio*, defined to be the ratio of the transverse width of the laser output to the dominant spatial scale of the pattern which comprises it. An equivalent description is in terms of the *Fresnel number* of the system, essentially the number of transverse modes the laser can support.

The two camps have much in common. They both rely heavily on the Maxwell-Bloch equations which describe the interaction of a light field with an ensemble of two-level atoms. However, when we consider transverse effects these equations are too complicated to be studied in their raw form and important simplifications must be made, assuming the laser field to be almost monochromatic – the laser is assumed to operate on only one longitudinal mode.

Most modern laser systems fall into the class of *small aspect ratio* systems. Their output can be expressed in terms of only a few empty cavity modes – in most cases *Gauss-Laguerre* or *Gauss-Hermite* modes[1]. This is no accident ; the design of laser cavities, the pumping mechanisms and the use of intra-cavity apertures ensures that, at most, only a few transverse modes can be excited. Consequently, the field in the Maxwell-Bloch equations can be expanded as a superposition of these modes and, in this way, their interaction can be studied[2]. This approach has been particularly useful in describing 'real lasers'. Experiments designed to test the theories use complicated detection schemes to extract information about the very fast dynamics involved – as an example see Coates *et al.*[3]. The transverse modes have a nonlinear coupling and so only a small number are required before very complicated spatio-temporal behaviour can be observed – see Brambilla *et al.*[4] and *op. cit.* This is a problem for laser designers since, for many applications, they would like an output of good beam quality. To ensure this, they usually force their systems to operate on only the fundamental Gaussian mode. One problem with this technique is that it does not easily scale to high powers. The limiting factor in many laser systems is the so called *damage threshold* of the gain medium – a large pump power focussed into a small mode volume can lead to damage of the material. A way out of this problem is to increase the transverse cross-section of the laser, use a broader pump beam and pump a larger volume in the gain medium. The drawback is that this inevitably leads to the excitation of higher order transverse modes and eventually to poor beam quality. To understand, and ultimately to control, such complicated transverse output is the goal of much theoretical work.

For this study, the 'small aspect ratio' theories, based on modes, are at a disadvantage because, when the laser has a large cross-section, the number of modes required to describe its dynamics becomes prohibitively large. Numerical simulation, using the modes as a basis, is still possible but, without analysis to guide our understanding, little can be learned.

The study of *large aspect ratio* systems has followed an entirely different theoretical approach. The Maxwell-Bloch equations are studied assuming plane parallel mirrors and an infinitely extended gain profile. This does not, however, mean that the field is assumed to be a plane wave ; it is free to develop whatever transverse structure it likes, unhindered by boundary effects. The benefits of this approach are fourfold. Firstly, the laser equations can be reduced to normal forms[5, 6], emphasising analogies between lasers and other pattern forming systems in optics and nonlinear science in general. Such analogies readily allow cross-fertilisation of ideas and analysis techniques[7, 8]. Secondly, the laser is favoured among pattern forming systems in that its equations have exact solutions[9] in the form of transverse travelling waves. This suggests an analysis in terms of Fourier modes and allows an even more detailed analysis than is usually possible. Thirdly, the constraint on the system being infinitely extended can be relaxed by considering the boundaries as perturbations[7, 10]. Lastly, the systems produce beautiful patterns – very therapeutic for a Ph.D student!

Figure 1.1 gives an overview of these approaches and gives some indication of the spectrum of aspect ratios which are 'understood' in the literature. In this thesis we hope to illuminate a little the areas 'not understood' by studying the transition between behviours characterised by 'boundary induced modes' and Fourier modes. These 'boundary induced modes' need not be cavity modes because it is not necessarily the cavity mirrors which confine the field transversely ; another possibility is that the mirrors are flat and the *gain* is of finite transverse extent. *Gain guiding*, as it is called, is relatively unstudied[11, 12] when compared to cavity modes, perhaps reflecting the fact that curved mirror cavities are far more widely used than flat mirror ones. There are however some laser systems, for example microchip lasers[13], which may rely on such guiding mechanisms for their stability. In chapter 2 we study the modes induced by a transversely varying gain.

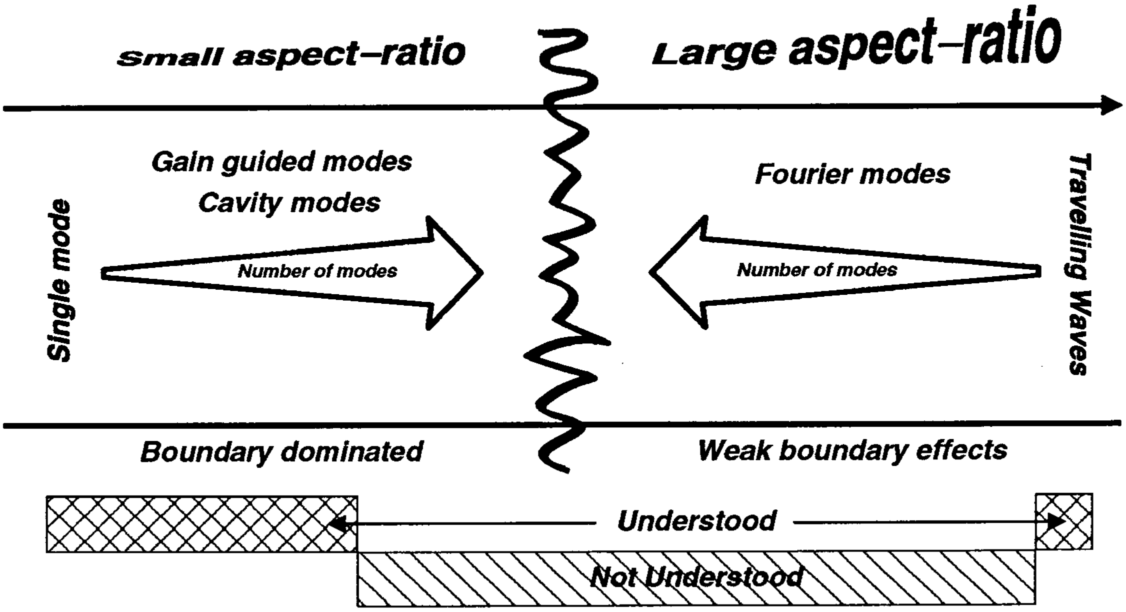

Figure 1.1: A diagrammatic description of laser theories – from small aspect ratio, single cavity mode to infinitely extended systems showing travelling waves.

In chapter 3 we move to the other end of the 'aspect ratio spectrum' (as defined in figure 1.1) to study the travelling waves found in infinitely extended laser systems. Drawing on analogies between pattern formation in lasers and in other fields we will follow the methods used there to describe the laser patterns, their stability and defects. Our understanding will be driven by the coupling of analytical results and those from numerical simulations.

Calling on the results of the previous chapters we attempt, in chapter 4, to bridge some of the gap between small and large aspect ratio lasers. We will do this, following the approach developed in other pattern forming systems, by studing the effects of transverse boundary conditions on the patterns of the infinitely extended system. We will consider transverse reflecting boundaries, those imposed by gain guiding and those forced by curved cavity mirrors.

Before starting a more thorough exposé of these subjects, I feel I should clarify the meaning of 'we' in this thesis. In the most part it is intended to mean 'you, the reader' and 'I'. It sounded awfully pretentious to be saying 'I' all the time! Even using 'we' defined in this way I feel I am doing somewhat of a disservice to my collaborators in this work and so I hope its use does not offend anyone!

Chapter 2

Gain Guiding in Lasers

2.1 Introduction

There has recently been an explosion of work on lasers using solid state materials as their active media. Such lasers are not, in fact, a new idea – the first lasers ever to work used flashlamp pumped ruby as their gain medium – but the materials used today are, more and more, being engineered for use specifically as laser gain media for given applications. Typical examples are Nd:YAG (Yttrium Aluminium Garnet doped with Neodimium ions), LNP (Lithium Neodimium Tetra-Phosphate), Ti:Sapphire and other such weird and wonderful concoctions. These materials have many advantages. They can be pumped very efficiently at wavelengths easily accessible by current, high powered diode lasers ; the materials store this pump energy very well making them ideal for Q-switching ; they have a very broad gain bandwidth, allowing great flexibility in tuning and allowing them to sustain very short pulses. Using advanced mode-locking techniques solid state lasers have been shown to generate pulses only a few optical cycles long (13fs). The materials often have good thermal properties allowing them to dissipate heat generated in the pumping process.

Trends towards miniaturisation have resulted in a lot of interest in *microchip* or *cube lasers*[13, 14, 15, 16, 17, 18]. Such devices consist of a thin slice or slab of solid state gain material – operation has been demonstrated with such materials as Nd:YAG, Nd:YVO$_4$, LNP and Yb:YAG, to name but a few. The laser is truly miniature in that the length of its active medium is typically less that 1mm. The cavity mirrors are coated directly onto the surface of the slab giving a very short plane-parallel cavity and, since the lasing wavelength is of the order of 1μm, the fractional free spectral range is very large. Such devices are typically end-pumped using a diode laser, or a collection of them, either focussed into the medium or simply butted onto the end. A schematic diagram of a microchip laser is shown in figure 2.1.[1]

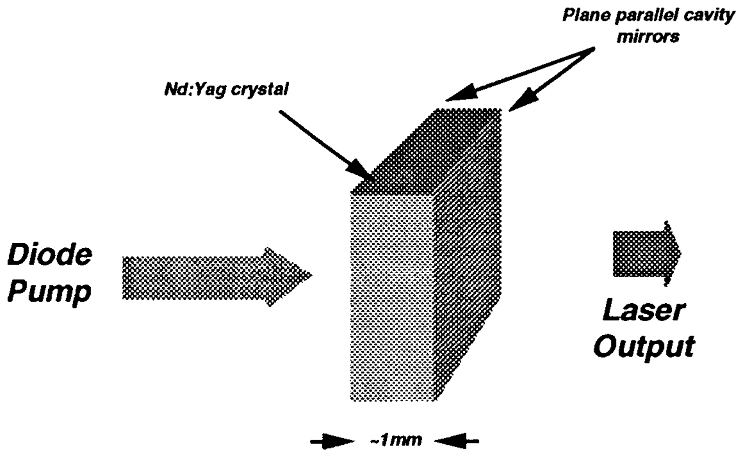

Figure 2.1: A schematic drawing of an end pumped microchip solid state laser with plane parallel cavity mirrors.

What do experimentalists observe when they make such lasers? They observe them to have almost exclusively continuous wave output implying that they lase on only a single longitudinal mode – not surprising since the free spectral range is usually larger than the gain bandwidth. The lasers are very efficient and are easy to set up because there is no alignment of the mirrors to be done. Despite the fact that the laser cavity is, at first glance, unstable the lasers operate very readily on a fundamental mode which is TEM$_{00}$ like.

The formation of transverse modes in a plane parallel cavity might be explained in a number of ways. The description which fits best depends a lot on the details of the

---

[1] *The 'microchip' principle has recently been raised to new levels of complexity by butting a nonlinear crystal onto the output mirror of the laser and finally, through second harmonic generation, producing output in the green.[19] A very complicated miniature device!!*

experimental setup. One such explanation is that, in our description of the cavity, we have failed to take account of the finite transverse extent of the gain region. Obviously, the system should only lase in a region of the transverse plane where the laser is pumped – that is where energy is being input. In other regions, the laser should be off. The 'on' and the 'off' state should connect smoothly and so there will be some sort of evanescent field in the unpumped region. Figure 2.2 shows a very simple picture of this *gain guiding*.

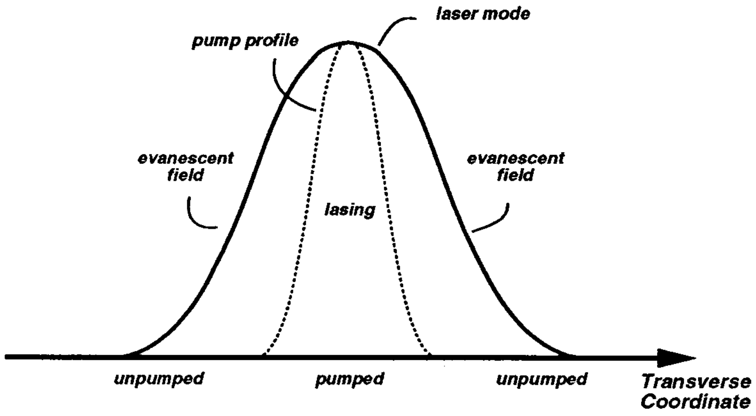

Figure 2.2: A schematic diagram of the mechanism for gain guiding in a microchip laser.

Other mechanisms, based on pump induced thermal effects, have been proposed [18, 20] to explain the stabilisation of the cavity in microchip lasers. The end pumping of the microchip causes heating of the gain medium and, through its *linear thermal dispersion* dn/dT, this can produce a transversely varying refractive index. Heating of the crystal also causes thermal expansion through its *linear thermal expansivity* dL/dT. The change in the optical length of the cavity, nL, can be expressed in terms of these:

$$\frac{d(nL)}{dT} = L\frac{dn}{dT} + n\frac{dL}{dT}.$$

Depending on the sign and magnitude of dn/dT, this change in optical path length can be guiding or anti-guiding. The exponents of the "thermal lensing" theory need to come up with two separate explanations for these two cases,

1. Zayhowski[20] has proposed a scheme applicable to materials, such as Nd:YAG, with $dn/dT > 0$. The pumping induces, in the gain medium, a temperature distribution which is peaked at the centre of the pump and decreases into the wings. The induced refractive index sets up a waveguide in the medium which helps to confine the laser field.
2. MacKinnon *et al.*[18] proposed a different scheme to explain their experiment consisting of an LNP microchip. LNP has a $dn/dT < 0$ and so the induced refractive index distribution in the gain medium should cause the laser field to diverge ; it cannot stabilise the plane-parallel cavity. LNP is a stoichiometric material meaning, in this case, that the pump beam is absorbed within a small volume at the input to the microchip. MacKinnnon *et al.*showed, by interferometric measurements, that such localised absorption of the pump light causes the input facet of the microchip to 'bulge' forming a mini-cavity with curved mirrors.

The exact mechanism for the formation of the transverse modes in microchip lasers is very dependent on the type of gain medium being used – it is still not fully understood for all systems. These points aside, the study of gain guided modes is interesting in its own right. In this chapter we will ignore such thermal effects and study these modes in the context of a microchip laser.

2.2 Equation for the Stationary State

Our starting point is the Maxwell-Bloch equations already derived in appendix A:

$$\begin{aligned} \nabla_T^2 F &+ \frac{iTkF}{L} + \frac{2ik}{c}\frac{\partial F}{\partial t} - \frac{2\delta_{cl} k}{c} F = 2igkR && (2.1) \\ \frac{\partial R}{\partial t} &= -i\delta_{al} R + \gamma_\perp F D - \gamma_\perp R && (2.2) \\ \frac{\partial D}{\partial t} &= -\frac{\gamma_\|}{2}\left[F R^* + F^* R\right] - \gamma_\| \left[D - D_o\right]. && (2.3) \end{aligned}$$

The equations describe the interaction of a laser field, F, with the electric dipole allowed transition in an ensemble of two-level atoms. The atoms are described by their material polarisation, R, and their population inversion, D. The *paraxial* and *slowly varying envelope* approximations are inherent in the equations' derivation. The field has been assumed to have a frequency, ω_l, close to a single longitudinal mode of a plane-parallel cavity ; the difference in frequency is characterised by the detuning parameter, $\delta_{cl} = (\omega_c - \omega_l)$. The laser frequency is detuned away from the atomic resonance by the quantity, $\delta_{al} = (\omega_a - \omega_l)$. The cavity is of length L and has an output coupler with intensity transmittivity T. The laser field has a longitudinal wavevector k and its diffraction is described by the term ∇_T^2. The atomic polarisation has a decay rate $\gamma_\perp$ and the population inversion decays to its steady state value, D_o, at a rate $\gamma_\parallel$.

The equations have been derived under the mean-field assumptions made in appendix A. Only a single longitudinal mode should be excited – which is exactly what is observed experimentally[13]. The cavity mirrors should be plane and parallel – exactly our situation. The cavity losses should be small allowing us to apply the mean field limit – mirror reflectivities in these lasers are of the order of 99% or higher.

The first thing we do is to rescale these equations slightly – the main reason is to scale the frequencies to the free spectral range so that we have an idea of how far we are tuning the laser with respect to the longitudinal mode separation. We write

$$\begin{aligned} \delta_{al} &\longrightarrow -\frac{c\delta_l}{2L}, \\ \delta_{cl} &\longrightarrow \frac{c(\delta_c - \delta_l)}{2L} \end{aligned}$$

where L is the length of the laser cavity. This scaling of the frequencies means that δ_l represents the laser field frequency and δ_c the longitudinal cavity mode frequency both with reference to the gain line centre. In this scaling the free spectral range is 2π, that is a change of 2π in δ_l or δ_c means that we move on to the next longitudinal mode. In scaling the frequencies this way it is convenient to scale the transverse coordinates,

$$(x, y) \rightarrow \sqrt{\frac{L}{k}}(x', y'),$$

and the time to the cavity round trip time,

$$\frac{\partial}{\partial t} \rightarrow \frac{c}{2L}\frac{\partial}{\partial \tau}.$$

Performing these scalings gives

$$\begin{aligned}
\frac{\partial F}{\partial \tau} &= i\nabla_{T'}^2 F - TF + i(\delta_l - \delta_c)F + \chi R \qquad (2.4)\\
\beta\frac{\partial R}{\partial \tau} &= i\beta\delta_l R + FD - R \qquad (2.5)\\
\frac{\partial D}{\partial \tau} &= -\frac{2L\gamma_{\|}}{c}\left[(FR^* + F^*R)/2 + D - D_o\right] \qquad (2.6)
\end{aligned}$$

where, to simplify the notation, we have defined a dimensionless bandwidth factor

$$\beta = \frac{c}{2L\gamma_{\perp}},$$

and the dimensionless pump parameter, the gain per cavity pass, is

$$\chi = 2gL.$$

Let's now consider the steady states of these equations by setting the time derivatives equal to zero. Solving for the steady state polarisation,

$$R = \frac{FD}{1 - i\beta\delta_l},$$

allows us to find the steady state population inversion,

$$D = D_o\,\frac{1 + \beta^2\delta_l^2}{1 + \beta^2\delta_l^2 + |F|^2},$$

and substituting these into (2.4), looking also for a steady state electric field, $\partial F/\partial\tau =$

0, gives the steady state field equation

$$\left[\nabla^2_{T'} + iT + \delta_l - \delta_c + \chi D_o(x',y')\,\frac{\beta\delta_l - i}{\beta^2\delta_l^2 + 1 + |F|^2}\right] F(x',y') = 0$$

Microchip lasers are usually pumped by diode lasers or by other solid state lasers and care is usually taken to ensure that the gain profile set up in the medium is Gaussian, or at least cylindrically symmetric. Under such conditions it is usually convenient to take advantage of this symmetry and to expand the field in functions of a similar symmetry. We will follow the example of the Gaussian-Laguerre functions described in appendix B and write the field as a product of a real intensity, a cylindrically symmetric part and a complex exponential in the angular direction,

$$F(x',y') = \sqrt{I}\,R(r)\,e^{im\phi}.$$

In this description, I is proportional to the intensity of the output at beam centre, r and ϕ are the transverse polar coordinates, and $R(r)$ gives the mode shape normalised so that if we write $R(r) = M(r)r^{|m|}$ then $M(0) = 1$; m is the angular mode index. This gives the working equation for this chapter

$$\left[\frac{d^2}{dr^2} + \frac{1}{r}\frac{d}{dr} - \frac{m^2}{r^2} + iT + \delta_l - \delta_c + \chi D_o(r)\,\frac{\beta\delta_l - i}{\beta^2\delta_l^2 + 1 + I|R(r)|^2}\right] R(r) = 0. \quad (2.7)$$

In equation (2.7) there are four unknowns: three real parameters, I, δ_l and χ, and the complex mode profile function $R(r)$. By fixing the value of one of the parameters we can solve (2.7) for the other two and the mode profile. To find mode thresholds, for example, we should set $I = 0$ and solve equation (2.7) for δ_l , χ and $R(r)$. A general choice of δ_l and χ results in a profile, $R(r)$, which diverges as $r \rightarrow \infty$ and only certain choices result in bounded profiles. These choices correspond to the laser frequencies and pump thresholds for each transverse mode operating independently.

2.3 Analytical solution

It would be nice if we could solve the ordinary differential equation (2.7) exactly to obtain the laser threshold, frequency and intensity. This is indeed possible but only in the limiting case of a few special pump profiles, D_o. For the profile we would like to study, a Gaussian, no such analytical solution is known. Our approach will be to study first the pump profiles which do allow an analytical solution and to use these results to tell us what we might expect from a numerical analysis of this equation for the Gaussian pump.

2.3.1 Plane Wave

We consider a pump profile which is uniform in space, that is $D_o = 1$. We consider also a laser field uniform in space and so we neglect the transverse derivatives in equation (2.7) to give [2]

$$iT + \delta_l - \delta_c + \chi \frac{\beta\delta_l - i}{\beta^2\delta_l^2 + 1 + I} = 0.$$

Separating the real and imaginary parts of this equation and solving for δ_l and I gives

$$\delta_l = \frac{\delta_c}{1 + T\beta} \tag{2.8}$$

$$I = \frac{\chi}{T} - 1 - \left(\frac{\beta\delta_c}{1 + T\beta}\right)^2 . \tag{2.9}$$

Equation (2.8) is the standard mode pulling formula expressing the lasing frequency as a weighted average of the cavity and atomic frequencies. Equation (2.9) gives the laser intensity as a function of the pumping χ and the cavity detuning δ_c. The threshold condition, that is the pump value, $\chi = \chi_t$, which gives $I = 0$, can easily be

---

[2] *Note that a plane wave pump need not necessarily lead to a plane wave field. The dependence of the variables on the transverse coordinates for a plane pump will be taken into account in chapter 3 and, for the moment, we consider only a plane wave output field.*

found from this expression:

$$\chi_t = T\left[1+\left(\frac{\beta\delta_c}{1+T\beta}\right)^2\right].$$

This plane wave model shows a linear relationship between the laser frequency and cavity detuning, a quadratic threshold versus detuning curve, and above threshold, a linear relationship between the laser intensity and pump power. The laser frequency is independent of pump power. Figure 2.3 summarises these results.

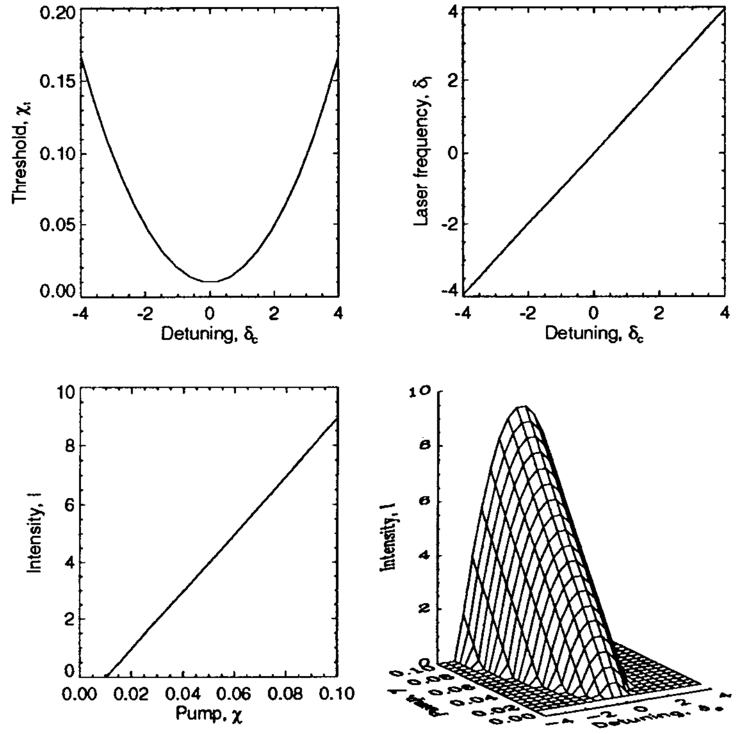

Figure 2.3: A summary of the results of the plane wave analysis.

2.3.2 Quadratic Pump Profile

The plane wave model gives a description of the basic features of a laser's operation, for example the existence of a detuning dependent threshold. However, in our study we would like to capture the effects produced by the transverse structure of the field. In fact, we'd like to consider a Gaussian pump profile, $D_o(r) = \exp(-\gamma r^2)$, which we can expand in a Taylor series to first order[21],

$$D_o(r) = 1 - \gamma r^2.$$

The parameter γ is a measure of the width of the pump, with $\gamma = 0$ corresponding to a plane pump. Using such a pump profile has the benefit that we break the pump's uniformity in the transverse direction. It has the drawback that for radii, $r > \sqrt{1/\gamma}$, the gain goes negative and eventually diverges. This divergence of the pump to $-\infty$ does not produce any unphysical divergences in the field since such an infinite loss simply forces the field to zero.

Inserting the expression for D_o into equation (2.7) and considering only the threshold problem, $I = 0$, we obtain

$$\left[\frac{d^2}{dr^2} + \frac{1}{r}\frac{d}{dr} - \frac{m^2}{r^2} + iT + \delta_l - \delta_c + \frac{\chi\,(1-\gamma r^2)}{\beta\delta_l + i}\right] R(r) = 0 \tag{2.10}$$

which we can solve analytically. Equation 2.10 has solutions of Gauss-Laguerre form

$$R(r) = e^{-\lambda r^2}\, f(r)\, r^{|m|}. \tag{2.11}$$

Here, the polynomial

$$f(r) = \sum_{j=0}^{j=p} a_j\, \lambda^j\, r^{2j}, \tag{2.12}$$

(p, m) are the radial and angular mode indices respectively, the complex parameter $\lambda = X - iY$ and $a_0, \ldots, a_n$ are constants normalised so that $a_0 = 1$. Y is a variable which is a measure of the phase front curvature of the transverse laser field. Substituting (2.11) and (2.12) into (2.10), separating real and imaginary parts and solving in terms of Y gives

$$X = \frac{\gamma}{8Y}(4qY + T) \tag{2.13}$$

$$\delta_l = \frac{X^2 - Y^2}{2\beta XY} \tag{2.14}$$

$$\delta_c = \delta_l + \frac{4}{\gamma}\left(X^2 - Y^2\right) - 4qX \quad (2.15)$$

$$\chi = \frac{4}{\gamma}\left[\beta\delta_l(X^2 - Y^2) + 2XY\right] \quad (2.16)$$

where $q = 2p + |m| + 1$ and the the first few constants a_i are shown in table 2.1.

p	a_1	a_2	a_3	a_4
0	0	0	0	0
1	$\frac{-2}{1+\|m\|}$	0	0	0
2	$\frac{-4}{1+\|m\|}$	$\frac{4}{(1+\|m\|)(2+\|m\|)}$	0	0
3	$\frac{-6}{1+\|m\|}$	$\frac{12}{(1+\|m\|)(2+\|m\|)}$	$\frac{-8}{(1+\|m\|)(2+\|m\|)(3+\|m\|)}$	0
4	$\frac{-8}{1+\|m\|}$	$\frac{24}{(1+\|m\|)(2+\|m\|)}$	$\frac{-32}{(1+\|m\|)(2+\|m\|)(3+\|m\|)}$	$\frac{16}{(1+\|m\|)(2+\|m\|)(3+\|m\|)(4+\|m\|)}$

Table 2.1: The constants, a_i, in the quadratic pump solution.

These equations show that the values for the thresholds and frequencies of the modes depend only on the value of q and so modes with equal values of q have degenerate threshold and tuning curves. So, for example, the modes $(p, m) = (0, 2)$ and $(1, 0)$ are degenerate. Modes (p, m) and $(p, -m)$ are also degenerate because of the rotational invariance of the pump profile. These degeneracies are also present in the Gauss-Laguerre description of empty cavity modes already considered in appendix B.

Figure 2.4 shows graphs computed from these formulae for typical microchip laser parameters. They show the variation of the pump threshold and laser frequency with cavity detuning for various widths of pump beam. In a gain guided system, the shape of the laser mode is determined by a balance between the effects of diffraction, causing the beam to diverge, and the localisation of the gain, confining the beam. A narrower pump beam will try to make the laser modes narrower and, as we saw in the study of empty cavity modes (appendix B), narrower beams diffract more. This relative broadening due to diffraction reduces the overlap between the mode and the pump, increasing the threshold for lasing. In the study of cavity modes, we also saw that narrow beams get a frequency shift associated with their transverse confinement, the narrower the beam, the more the frequency shift. Both these threshold and frequency effects are easily seen in the quadratic pump profile results in figure 2.4.

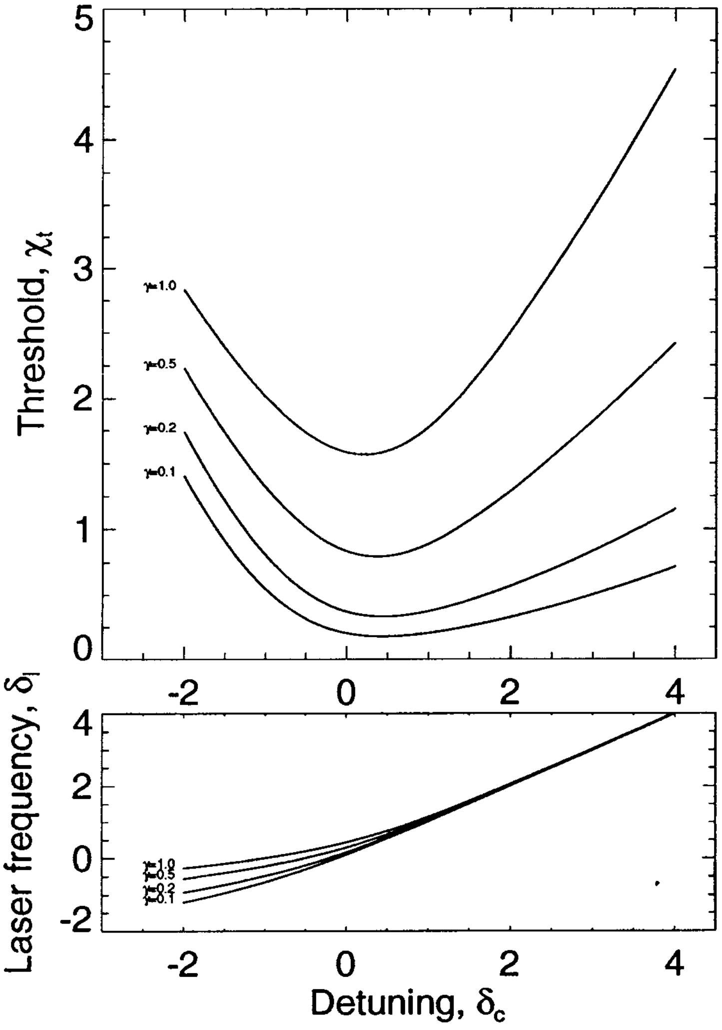

Figure 2.4: Scaled pump threshold, χ_t*, versus scaled cavity detuning,* δ_c *for a quadratic pump profile and various pump widths, characterised by* γ*. Parameters are* $T = 0.01$ *and* $\beta = 1$.

Notice that, in contrast with the plane wave model, the tuning curves are no longer linear and the threshold curves are asymmetric about their minima. This can be explained as follows. Consider the term in equation (2.10), the gain and dispersion induced by the atomic resonance

$$\frac{\chi\left(1-\gamma r^2\right)}{\beta\delta_l + i}.$$

The imaginary part of this term represents the frequency dependent gain and the real part is a frequency dependent dispersion – or refractive index change. Figure 2.5 shows a plot of this refractive index change versus frequency and the transverse coordinate, r. For laser frequencies greater than the atomic frequency, $\delta_l > 0$, the gain produces a positive change in refractive index. Since the pump varies transversely it induces a transverse 'hump' in the refractive index which acts as a weak waveguide helping to confine the laser field within the pump, enhancing mode-pump overlap and reducing the threshold. Conversely, for $\delta_l < 0$, because of the opposite sign of the index change, the pumping induces a transverse dip in the refractive index spreading the beam and leading to an increased threshold. This idea is verified by the fact that

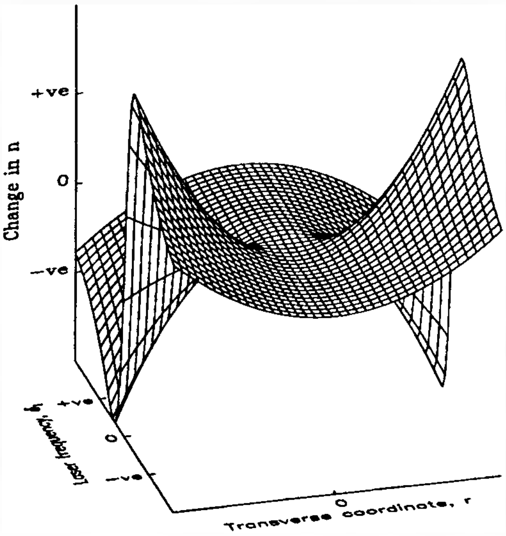

Figure 2.5: The dispersion – that is the change in refractive index, n – induced near the atomic resonance as a function of the laser frequency, δ_l, and the transverse coordinate, r. For $\delta_l > 0$, the pump induces a guiding refractive index profile ; for $\delta_l < 0$, the refractive index profile is anti-guiding.

the value of Y changes with laser frequency and, consequently, so does the phase front curvature. Large curvatures, indicating large diffraction losses, are observed for $\delta_l < 0$ and, conversely, for $\delta_l > 0$ the wave fronts are flatter and diffraction losses smaller.

We have derived formulae for the thresholds and frequencies of all the transverse modes of the quadratic pump system. Unfortunately, these formulae consider only one transverse mode at a time – that is to say that the thresholds we find are for the instability of the 'off' state to a particular transverse mode. We will address this problem later in section 2.4.3.

Firth *et al.*[21, 22] have used a variational method to find the best-fit Gauss-Laguerre mode to the solution of the problem with a Gaussian gain variation. They have shown that the quadratic pump approximation is similar to the variational method if δ_c is displaced by $(4p + 2m + 1)\gamma$, shifting the threshold and tuning curves in figure 2.4. The value of λ in (2.11) is similarly shifted implying that the variational method gives broader modes. This is to be expected since the quadratic pump profile has a large, unphysical loss for $r > \sqrt{1/\gamma}$.

We now make some remarks about the dependence of the thresholds on the width of the pump profile, that is how they change with γ. On the left of figure 2.6, we have plotted the thresholds for the first four gain guided modes as a function of γ. The results show that, as γ is made smaller, that is the pump becomes closer to a plane wave, the threshold is decreased[3]. On the right of the figure we have plotted the quantity $MD(\gamma) = (\chi_t)_{ho}/(\chi_t)_{00} - 1$, where $(\chi_t)_{ho}$ is the threshold for the higher order modes and $(\chi_t)_{00}$ is that for the (0,0) mode. The quantity MD, connoting 'mode discrimination', gives an estimate of how susceptible the fundamental mode is to the intrusion of ones of higher order. In the limit $\gamma \longrightarrow 0$, the limit of large aspect-ratio, the modes become degenerate and the discrimination is poor. This process of higher order mode intrusion will be considered in more detail later in this chapter and also in chapter 3.

---

[3] *Remember that the threshold computed here is proportional to the required intensity at the center of the pump beam, not to its total power.*

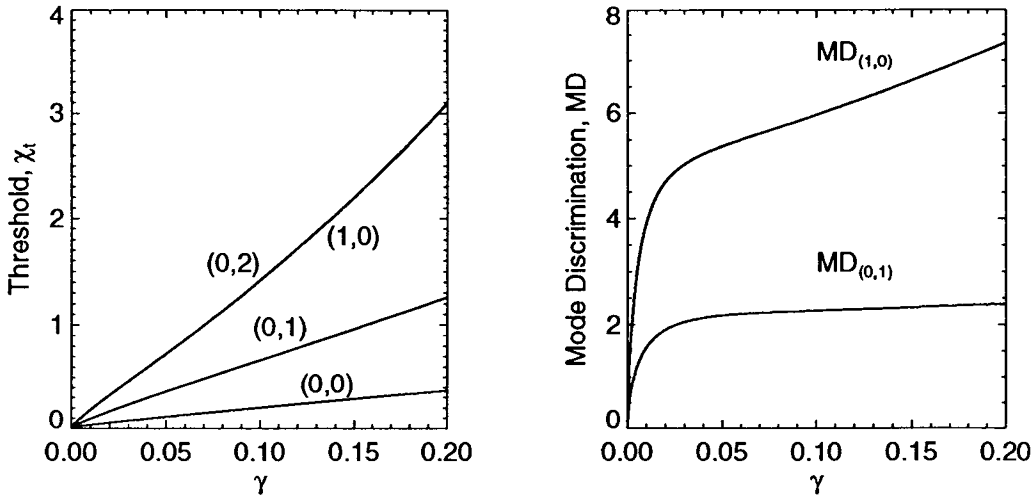

Figure 2.6: On the left, the thresholds for the first four transverse modes as a function of γ. The thresholds decrease with γ. On the right, the 'mode discrimination' – discussed in the text – as a function of γ.

2.3.3 sech^2 pump profile

It has very recently been shown[23] that, in one cartesian transverse dimension x, a pump profile $D_o = \mathrm{sech}^2(\gamma x)$ also leads to exact solutions. Like the quadratic pump solution discussed above, they are defined parametrically. They look very exciting because they seem to show many features of an exact numerical simulation with Gaussian gain.

2.4 Numerical Solution – Gaussian Pump

The quadratic pump profile used in the last section is useful in so far as it lets us study the threshold problem, away from the plane wave limit, without relying on numerical analysis. The quadratic profile is, however, not a good approximation to a Gaussian for large radii and, as we shall see, a Gaussian pump profile, $D_o(r) = e^{-\gamma r^2}$, introduces several new and important phenomena. Unfortunately, in this case, we will have to consider a numerical solution to equation (2.7).

The procedure we use for numerical solution of this equation follows the prescription already outlined in section 2.2. By imposing the relevant boundary conditions on the field in equation (2.7), we can solve for any two of the unknowns, I, χ, and δ_l, and the mode profile, $R(r)$, as a function of the other unknown and the system parameters.

2.4.1 Laser Threshold

As an example, let's consider the problem of finding the laser thresholds, just as we did for the quadratic pump. The procedure we will describe can be used equally well for finding the modes and intensities above threshold, as we will describe later. For the moment, we put $I = 0$ into equation (2.7) to obtain

$$\left[\frac{d^2}{dr^2} + \frac{1}{r}\frac{d}{dr} - \frac{m^2}{r^2} + iT + \delta_l - \delta_c + \frac{\chi\, e^{-\gamma r^2}}{\beta\delta_l + i}\right] R(r) = 0. \tag{2.17}$$

We now have two unknowns, χ and δ_l – note that in the case of finding intensities above threshold, the unknowns would be I and δ_l. If we choose arbitrary values for χ and δ_l, the equation (2.17) is simply an ordinary differential equation for the mode profile, $R(r)$. However, as figure 2.7 shows, such an arbitrary choice usually leads to a mode profile which diverges as r tends to infinity. Only a discrete set of χ and δ_l values leads to profiles which converge. The elements of this set are distinguished by the number of maxima the mode profiles have for a radius, r, in the interval $[0, \infty)$. We define $p + 1$ to be this number of maxima. This will become clearer in section 2.4.3. Our numerical problem is to find this set. The first problem we see is that it is impractical to use a boundary condition at infinity in a numerical computation. To circumvent this problem we can use a trick based on the fact that the term $D_o(r) = e^{-\gamma r^2}$ in equation (2.17) (and in equation (2.7)) becomes negligible for radii $r \gg \sqrt{1/\gamma}$. In fact, in that limit, equation (2.17) becomes

$$\left[\frac{d^2}{dr^2} + \frac{1}{r}\frac{d}{dr} - \frac{m^2}{r^2} + iT + \delta_l - \delta_c\right] R_o(r) = 0.$$

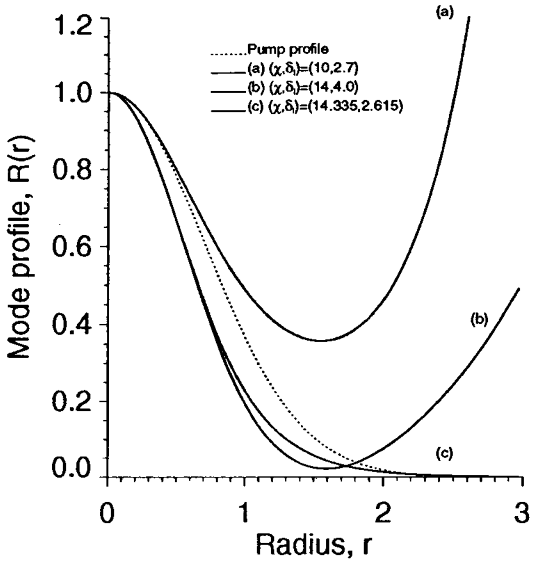

Figure 2.7: An example of the mode profiles obtained from equation (2.17) for some arbitrary values of χ and δ_l. Other system parameters are, $T = 1$, $\beta = 1$, $\gamma = 1$, $\delta_c = 4$.

This is a complex form of Bessel's equation, which has an exponentially decaying solution

$$R_o(r) = J_m\left(r\sqrt{iT + \delta_l - \delta_c}\right) + iY_m\left(r\sqrt{iT + \delta_l - \delta_c}\right)$$

where J_m and Y_m are Bessel functions of the first and second kind respectively, both of order m. Since all mode profiles which will converge must do so according to this solution, we can modify the convergence condition to be that the mode profile, $R(r)$ must tend to $R_o(r)$ when the radius $r \gg \sqrt{1/\gamma}$. The similarity of the functions R and R_o can be tested by evaluation of their *Wronskian*, defined

$$W = \begin{vmatrix} R_o & R \\ R'_o & R' \end{vmatrix},$$

where the prime indicates differentiation with respect to r. The Wronskian is zero if and only if the functions can be linearly scaled so that they match exactly – see, for example, reference [24].

In summary then, to find the threshold pump, χ, and laser frequency, δ_l, follow the algorithm:

1. Choose trial values for χ and δ_l ; use the results of the quadratic pump analysis, for example.
2. Integrate equation (2.17) out to some radius where the pump is negligible, say $r' = \sqrt{8/\gamma}$.
3. Evaluate the Wronskian of the mode $R(r')$ and the 'no–pump' solution, $R_o(r')$.
4. If the Wronskian is not zero, choose a new χ and δ_l to try to make the Wronskian zero.
5. Go back to step 2.

Now, a slight aside to discuss the intricacies of point number 4 in the above prescription. Simplifying the problem, we have a function $W(\chi, \delta_l)$ whose zeros we require to find. This process can be attempted in a number of ways, as described in Numerical Recipes[25], for example. General routines for finding the roots of nonlinear functions could form whole Ph.D. theses ; suffice it to say that the ease of finding such roots depends strongly on the shape of the given function. Most routines work iteratively and the probability of converging successfully can be greatly enhanced by choosing a good starting point for the process. As described in the prescription above, the quadratic pump analysis or the "variational gaussian" method[21, 22] give good starting estimates for χ and δ_l. Given this, we have used a Newton method from Numerical Recipes[25] to successively improve this estimate. Another method of finding roots of nonlinear functions is to re-cast the problem as a single nonlinear function whose zeros are at the roots. Routines to find minima of this function can then be employed. We used a "downhill simplex method", aptly named `AMOEBA` in Numerical Recipes[25], to do just this. The downhill simplex method is slower but is more robust to inaccuracies in the starting guess.

Figure 2.9 shows the threshold pump and laser frequency versus cavity detuning, that is χ and δ_l versus δ_c, for the lowest order transverse mode, $(p, m) = (0, 0)$. Also shown are typical transverse mode profiles. The curves show similar features to those of the quadratic pump profile, except that the profiles decay exponentially rather than as a Gaussian. To emphasise this point, figure 2.8 shows the mode profiles plotted on a log-linear scale. As in the case of the quadratic pump shape, the threshold curves are asymmetric due to the pump–induced guiding or anti–guiding. Figure 2.9 shows that the modes are indeed broader for negative cavity detunings, where the mode is index anti–guided.

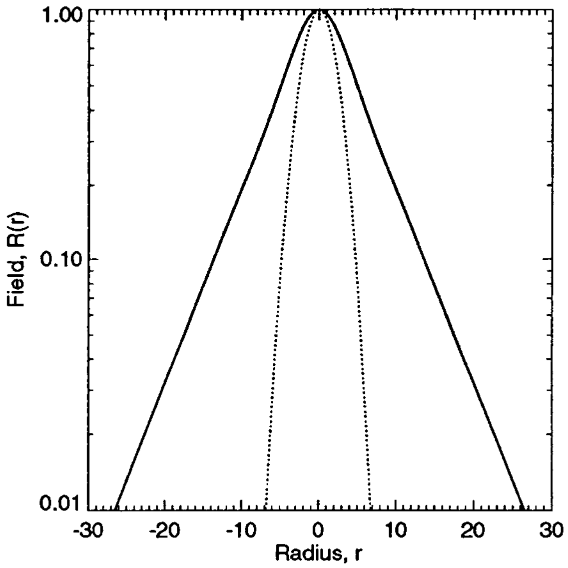

Figure 2.8: A modes profile obtained for a gaussian gain profile plotted on a log-linear scale. The mode profile decays in the wings as an exponential.

2.4.2 Laser Intensity

To find the laser intensity and frequency above threshold we follow a similar procedure to that above. We fix a value of the pump, χ, in equation (2.7) and find the I and δ_l which make the Wronskian zero. The results in figure 2.10 show that above threshold the intensity of the $(0,0)$ mode increases essentially linearly with pump power. Unlike the plane wave model the laser frequency does change a little with pump power. The laser tunes down in frequency by about 2% of the free spectral range for this range of pump powers. As the pumping is increased the gain tends to saturate, reducing slightly its guiding effect. This means that the gain guided mode becomes broader

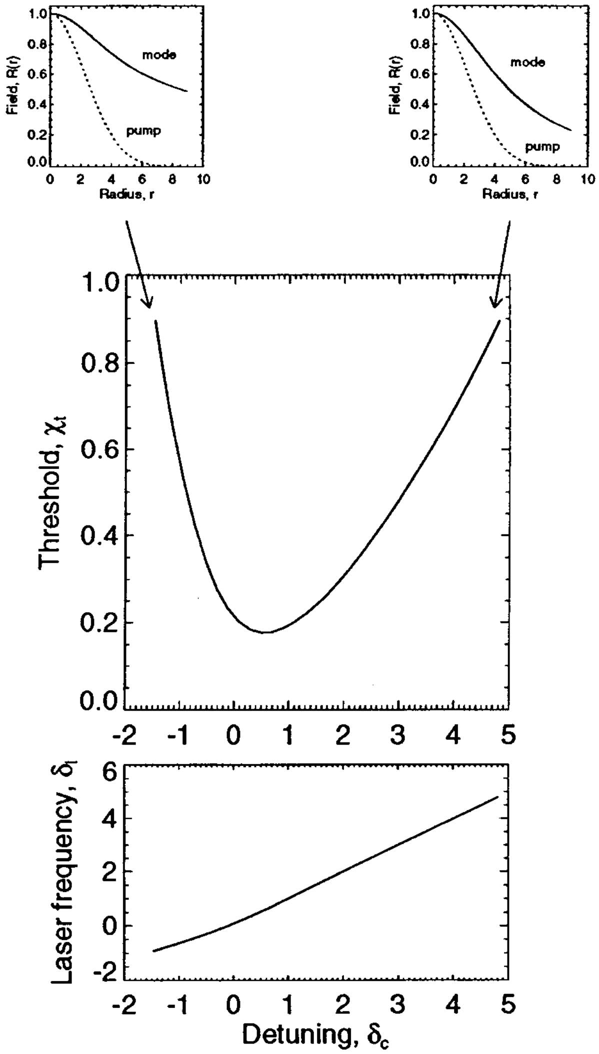

Figure 2.9: Threshold and tuning curves for the laser with a Gaussian pump profile. Also shown are the transverse mode profiles and pump intensity profiles for two cavity detunings. Parameters are $T = 0.01$, $\beta = 1$, $\gamma = 0.1$.

and closer in frequency to those of the empty cavity.

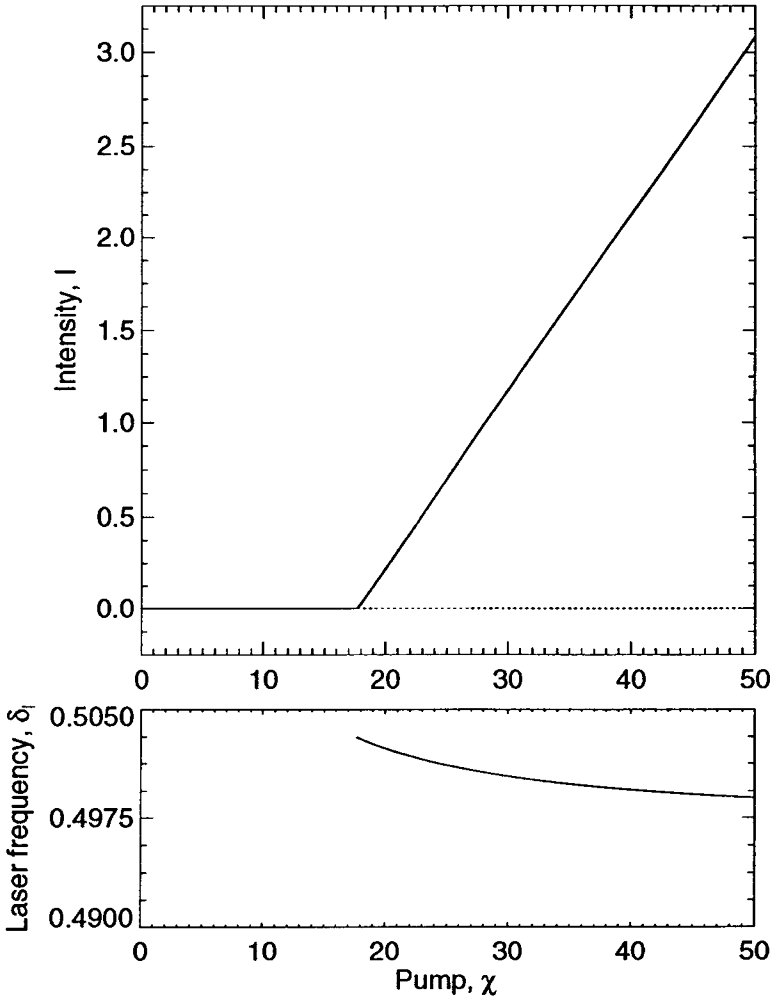

Figure 2.10: Scaled output intensity and laser frequency versus input pump power for a Gaussian pump profile. Parameters are the same as in figure 2.9 with $\delta_c = 0.47$.

2.4.3 Higher Order Modes

Consider now the thresholds for higher order Gauss-Laguerre type modes of the gain guided system. The procedure for finding these is exactly the same as in section 2.4.1 and we insert the m value of the mode we want into equation (2.17) and find the values of χ and δ_l giving a mode profile which undergoes p inflections before decaying to zero. The thresholds for the first four modes operating independently are shown in figure 2.11 and the corresponding mode profiles are shown in figure 2.12. We saw already that for the quadratic pump, modes with equal values of $q = 2p + |m| + 1$ were degenerate in threshold and in frequency. This degeneracy is broken in the case of the Gaussian pump. The degeneracy of modes with opposite sign of m remains unbroken because we have not broken the rotational invariance of the pump.

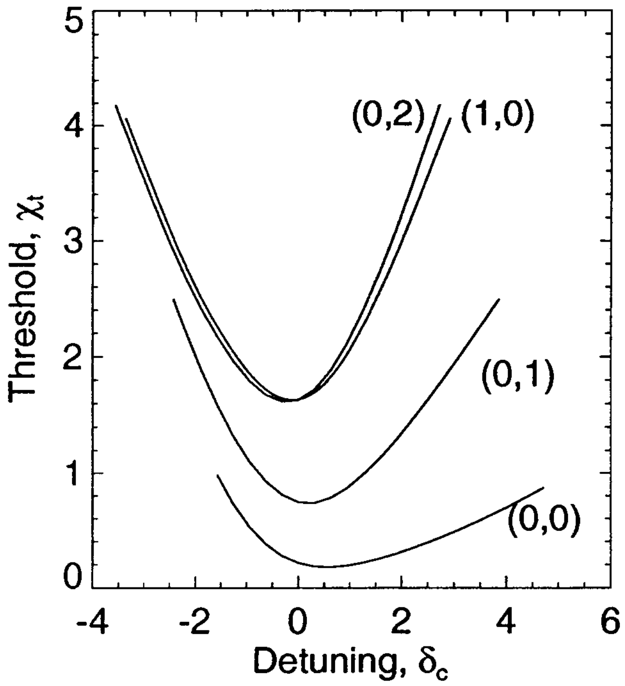

Figure 2.11: Pump threshold versus cavity detuning for higher order transverse modes operating independently of each other.

2.5 Stability of modes

Until now, we have only considered thresholds for transverse modes operating independently of one another. As mentioned already in section 2.3.2 the thresholds we find are for the instability of the 'off' state to a particular transverse mode and not the stability of a mode to any other.

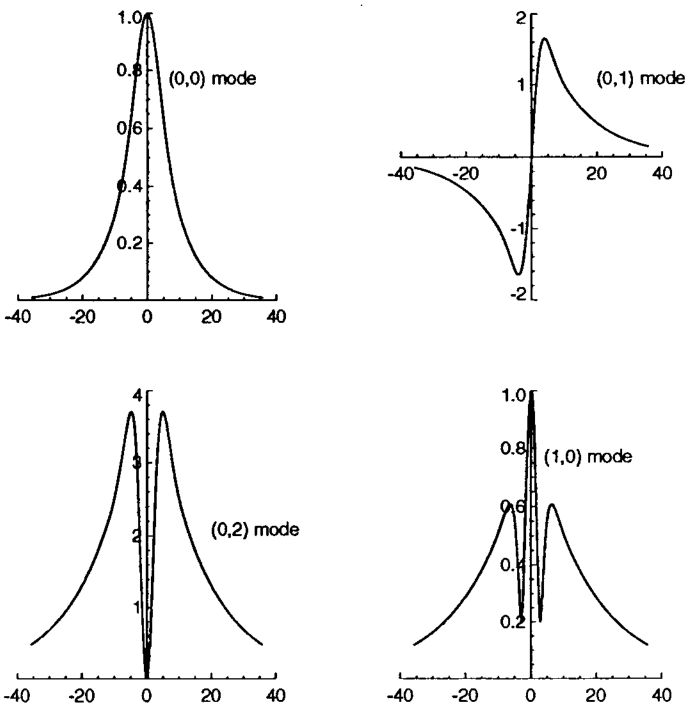

Figure 2.12: The transverse mode shapes of the four lowest order transverse modes of the gain guided system. The modes are assumed to be operating independently.

To make this a little clearer, let's consider a thought experiment involving a microchip laser. We'll consider a setup in which we can start the input pump power off at zero and slowly ramp it up and let's consider the experimental parameters corresponding to figure 2.11. With the pump off, the laser will be off and as we increase the pump above the threshold for the $(0,0)$ mode, that mode will switch on. As the pump power is increased further, the $(0,0)$ mode will grow in intensity as described in section 2.4.2. Consider now that, for some strange reason, the laser cannot or will not operate on the $(0,0)$ mode. Now, the laser will not switch on until the pump crosses the threshold for operation of the next mode in figure 2.11, the $(0,1)$ mode. This is the threshold we have found for the $(0,1)$ mode. What we have *not* found is the threshold for simultaneous operation of the $(0,0)$ and $(0,1)$ modes. Finding this is the main aim of this section.

Here we address the problem of finding thresholds for the co-existence of gain guided transverse modes. The first competition takes place between the $(0,0)$ mode and the $(0,1)$ mode and so these are the ones we will consider. The calculation of this threshold will give an indication as to the stability of the $(0,0)$ mode to perturbations.

All the work done until now has assumed that there is only one frequency present in the system, that is that there is only one transverse mode lasing. In order to treat two modes we have to go back to the Maxwell–Bloch equations and rederive the equations for the stationary states.

Consider the following perturbation expansions of the field, polarisation and population inversion

$$\begin{aligned} F &= F_s + F_+ e^{i\Omega\tau} + F_- e^{-i\Omega\tau} && (2.18)\\ R &= R_s + R_+ e^{i\Omega\tau} + R_- e^{-i\Omega\tau} && (2.19)\\ D &= D_s + D_+ e^{i\Omega\tau} + D_- e^{-i\Omega\tau}. && (2.20)\end{aligned}$$

In this expansion we intend the s subscript to indicate a stationary solution – we'll consider it to be the $(0,0)$ mode ; the $+$ and $-$ subscripts represent small perturbations to this stationary solution. The small perturbations will be the $(0,1)$ mode just as it starts to lase also. We allow for the perturbations to be at a frequency different from the stationary solution – just as one would expect for different transverse modes. We must require, however, that this frequency difference, $\Omega \ll 2\pi$, in order to stay within the mean field assumptions made in deriving the Maxwell-Bloch equations. Note also that $D_- = D_+^*$ to keep D real.

Substituting the expansions (2.18)–(2.20) into equation (2.6), linearising in the perturbing amplitudes and separating parts oscillating at different frequencies gives

$$\begin{aligned} \frac{\partial D_s}{\partial\tau} &= -\frac{2L\gamma_\parallel}{c}\left[(F_s R_s^* + F_s^* R_s)/2 + D_s - D_o\right] && (2.21)\\ \frac{\partial D_+}{\partial\tau} + i\Omega D_+ &= -\frac{2L\gamma_\parallel}{c}\left[(F_+ R_s^* + F_s R_-^* + F_-^* R_s + F_s^* R_+)/2 + D_+ - D_o\right] && (2.22)\end{aligned}$$

and a corresponding expression for D_-. If we choose the correct frequency offset, Ω, then not only will the $\partial D_s/\partial\tau = 0$, but $\partial D_+/\partial\tau = 0$ also. In this case, we solve equation (2.22) for D_+,

$$D_+\left(\underbrace{1+\frac{i\beta\Omega\gamma_\perp}{\gamma_\|}}_{(a)}\right) = D_o - (F_+R_s^* + F_sR_-^* + F_-^*R_s + F_s^*R_+)/2.$$

For a typical solid state microchip laser $\beta \approx 1$, $\gamma_\perp \approx 10^{10}$, $\gamma_\| \approx 10^5$ and, as we will see, $\Omega \approx 10^{-2}$. For these parameters, the term marked (a) is very large indeed, approximately 10^3. This means that, in parameter regimes where we will work, the values of D_+ and D_- will be very small. From now on, we will neglect them in our perturbation expansion,

$$D_+ = D_- \to 0$$

What does this mean from a physical point of view? The coupling of the modes is very important in their competition. This approximation means that so long as the modes are separated in frequency by more than $\gamma_\|$ then there are no coherent couplings between them – they will couple only through their sharing of the available gain.

Using our new ansatz about D_+ and D_-, we substitute the expansions (2.18) – (2.20) into the scaled Maxwell–Bloch equations (2.4) – (2.6) and solving for the steady state field perturbation, F_+, gives

$$\left[\nabla^2_{T'} + iT + \delta_l - \Omega - \delta_c + \chi D_o\,\frac{1+\beta^2\delta_l^2}{\beta^2\delta_l^2+1+|F_s|^2}\,\frac{1}{\beta(\delta_l-\Omega)+i}\right]F_+ = 0.$$

There is an equivalent expression for F_-. Going back to cylindrical coordinates and reinserting $D_o = \exp\left(-\gamma r^2\right)$ gives the working equation

$$\begin{aligned}\Bigg[\frac{d^2}{dr^2} \;+\; &\frac{1}{r}\frac{d}{dr} + \frac{m^2}{r^2} + iT + \delta_{l00} - \Omega - \delta_c + \\ &\chi e^{-\gamma r^2}\,\frac{1+\beta^2\delta_{l00}^2}{\beta^2\delta_{l00}^2+1+I_{00}|R_{00}|^2}\,\frac{1}{\beta(\delta_{l00}-\Omega)+i}\Bigg]R_{01}(r) = 0.\end{aligned} \tag{2.23}$$

We have rewritten δ_l as δ_{l00} to make clearer the distinction between frequencies referring to the active $(0,0)$ mode and to the perturbing $(0,1)$ mode for which the equation applies. This equation is, basically, the two mode equivalent of equation (2.17) and we can find the threshold for the simultaneous operation of the two modes in a similar way to that demonstrated already. The situation is slightly complicated by the existence of the terms $I_{00}|R_{00}(r)|^2$ and δ_{l00} which involve the intensity, mode profile and frequency of the lasing $(0,0)$ mode at the value of the pump, χ.

The method for finding, from equation (2.23), the pump threshold and frequency for the intruding $(0,1)$ mode is similar to those above. We choose an arbitrary χ and Ω, find the intensity, I_{00}, mode profile $R_{00}(r)$, and frequency, δ_{l00}, of the $(0,0)$ mode at this pump value from equation (2.7) and then numerically integrate equation (2.23) until we match onto the analytical solution, $R_o(r)$ in equation (2.18), where the pump is negligible. We iterate this process using a nonlinear minimisation routine to find the 'physical' choice of χ_t and Ω which ensures a match of these two solutions.

As we have already encountered, minimisation of a general nonlinear function usually requires a good estimate of the position of the minimum. In our case, to ensure convergence of the `AMOEBA` method, the initial guess at χ_t and Ω must be good. In the section on thresholds for modes operating independently we could use the quadratic pump results, for example, as an initial guess. In this case, we have no such luxury. One method we have used is as follows:

- We notice that if $I_{oo} = 0$ in equation (2.23) then we obtain the threshold equation for the $(0,1)$ mode operating independently. We can use the quadratic pump approximation to give us an estimate for its threshold and frequency.
- Define a 'multiplying factor', η, which varies between 0 and 1 and use it to pre-multiply I_{oo} in equation (2.23). By changing η in small steps between 0 and 1, we can slowly deform the independent $(0,1)$ problem into the one with simultaneous operation. Since the problem is deformed in small steps the previously computed (χ, δ_l) is a good estimate of the (χ, δ_l) at the next step in η.[4]

---

[4] *In fact, when we apply the method, we usually find that some extrapolation of previously computed points produces a much more effective starting guess.*

Figure 2.13 shows the threshold for the $(0,1)$ mode versus η where $\eta = 0$ corresponds to no gain saturation by the $(0,0)$ mode and $\eta = 1$ is the gain correctly saturated. The figure shows that the threshold for intrusion of the $(0,1)$ mode is very high indeed. In fact the curve diverges so rapidly that it appears that above a certain value of η it may be impossible to excite the higher order modes. What is the reason for this remarkable stability?

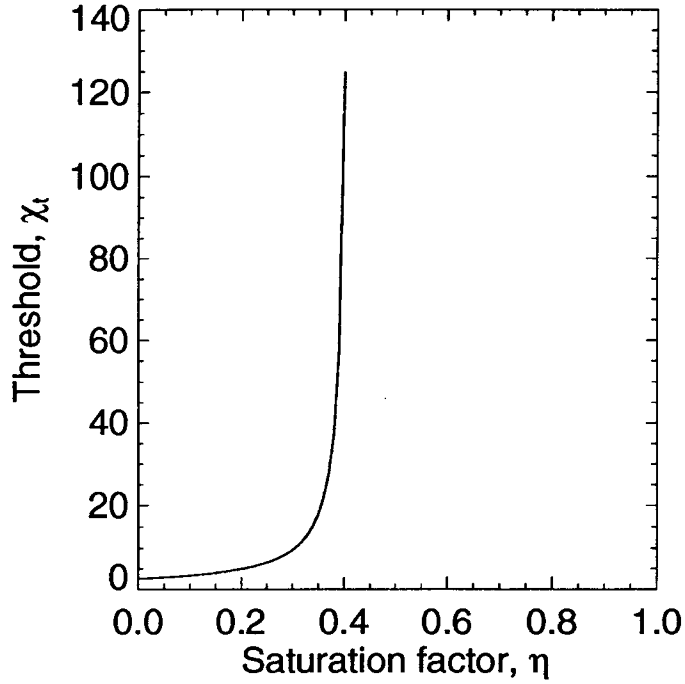

Figure 2.13: The pump threshold for simultaneous operation of the $(0,1)$ *and* $(0,0)$ *modes versus the* η *parameter which describes the extent to which the* $(0,0)$ *mode saturates the gain. The value* $\eta = 1$ *is the 'correct' saturation.*

We showed, in section 2.4.1 that, for typical microchip laser parameters, the $(0,0)$ mode extends well out into the wings. A microchip laser has a very high finesse cavity, meaning low losses. When lasing, the gain always balances the losses and so, in such a laser, the gain must be very weak and hence so must be the gain guiding. This weak guiding doesn't confine the $(0,0)$ mode very well and so it saturates the gain right out into the wings of the transverse plane leaving no gain for competing modes. To illustrate this point, consider the gain available for the $(0,1)$ mode when the $(0,0)$ mode is active. The relevant term in equation (2.23) is

$$\chi e^{-\gamma r^2} \frac{1+\beta^2\delta_{l00}^2}{\beta^2\delta_{l00}^2+1+I_{00}|R_{00}|^2} \frac{1}{\beta(\delta_{l00}-\Omega)+i} \tag{2.24}$$

In the simplifying approximation of $\delta_{loo} = \Omega = 0$ we plot this gain versus the radius, r, in the transverse plane and the pump power, χ ; figure 2.14 shows the resulting surface. Increasing the pump power, χ, in equation (2.24) is balanced by the corresponding increase in the intensity of the $(0,0)$ mode, I_{oo}, and so produces very little net increase in available gain.

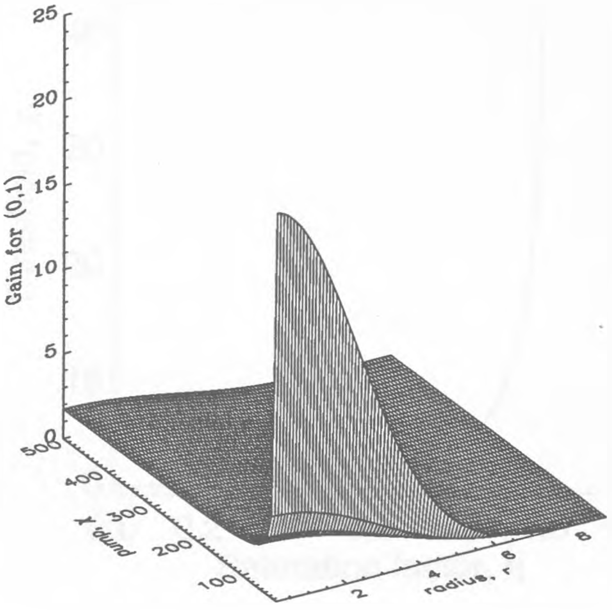

Figure 2.14: The gain available for the $(0,1)$ *mode when the* $(0,0)$ *mode is active plotted versus radius in the transverse plane,* r*, and pump intensity,* χ*.*

What laser parameters should we change in order to be able to excite higher order modes? In the section on empty cavity modes we showed that, for a plane-plane cavity, the modes were degenerate. We might expect that as we make the pump beam broader, tending to infinity, the modes would again become degenerate, and hence excitable. Another argument for this is that the broad shape of the $(0,0)$ mode is formed as a balance between diffraction of the field and its confinement due to the gain guiding. If the pump beam is made broader we'd expect weaker diffraction and to obtain a $(0,0)$ mode which is narrower in relation to the pump. This narrower mode will saturate the gain less effectively than before and so we may be able to excite the higher order modes.

Figure 2.15 is similar to figure 2.13 but has a pump beam which is twice as wide. It shows that there now exists a value of the pump power for which the $(0,0)$ and $(0,1)$ modes can co-exist. Figure 2.16 shows, for the broader pump, the threshold for this co-existence versus the cavity detuning. Also plotted is the threshold for the $(0,0)$ mode. The figure shows that for a certain range of cavity detunings it is possible for the modes to co-exist but that the pump threshold is very high, approximately 20 times above the first laser threshold. Furthermore, the range of cavity detunings where the higher order mode exists is not a range where the laser is likely to be used practically since the first threshold there is roughly 8 times higher than at its minimum value. The higher order modes exist in a range of cavity detunings in which we might

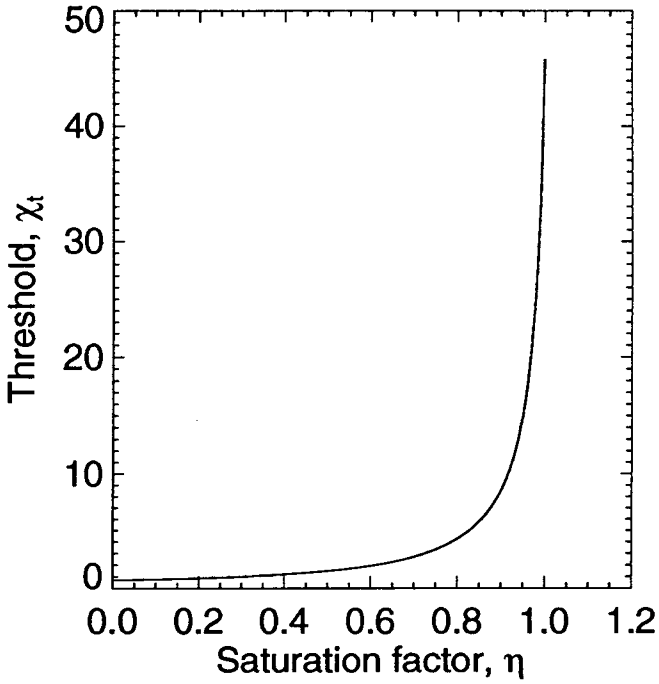

Figure 2.15: The pump threshold for simultaneous operation of the $(0,1)$ *and* $(0,0)$ *modes versus* η *for a pump beam twice as broad as in figure 2.13. Parameters are* $T = 0.01$, $\beta = 1$, $\gamma = 0.025$, $\delta_c = 4.37$.

also expect to see strong competition between different longitudinal modes. Such competition has been studied by Firth *et al.*[22] within the confines of the parabolic pump approximation but, here, we have not considered such effects.

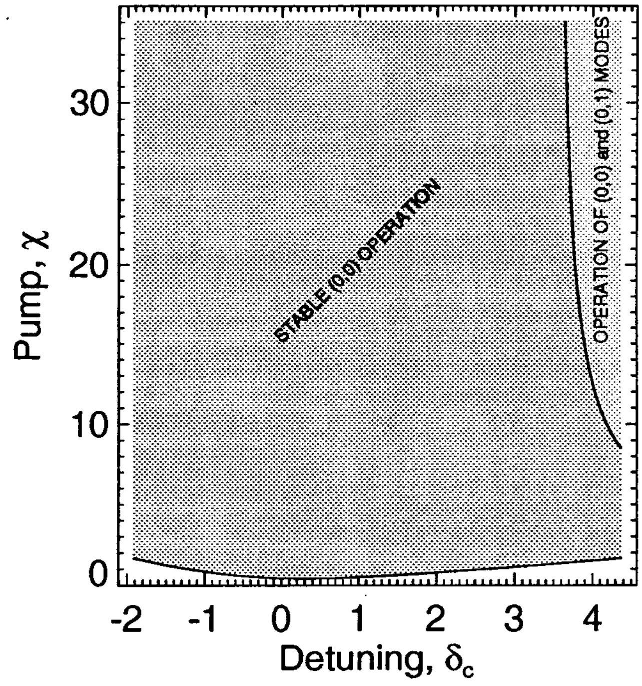

Figure 2.16: The pump threshold for simultaneous operation of the $(0,1)$ *and* $(0,0)$ *modes versus* η *for a pump beam twice as broad as in figure 2.13. Parameters are* $T = 0.01$, $\beta = 1$, $\gamma = 0.025$.

2.6 Curved Mirrors

To summarise, the main results for gain guided modes in a plane-parallel cavity are as follows:

- Although a plane-parallel laser cavity is, by the usual definition, an unstable resonator, a cylindrically symmetric gain profile can stabilise the cavity, leading to transverse modes of Gauss-Laguerre type.

- In contrast to standard Gauss-Laguerre modes, the field in the wings decays as an exponential rather than as a Gaussian.
- For high finesse laser cavities used in microchip lasers, the fundamental (0,0) mode has very broad wings, allowing it to effectively saturate all the available gain. This suppresses the higher order transverse modes.

We can now ask the question, does this work have any relevance to cavities with curved mirrors? It is possible, in fact, to extend this work so as to be valid for more general laser systems, possibly with curved cavity mirrors. We need to rewrite the equation for the laser field in an optical cavity of the type shown in figure B.1. It has been shown[2] that application of the mean field model to such a cavity has the effect of modifying the transverse laplacian in the field equation (2.1):

$$\nabla_T^2 \rightarrow \tan^{-1}\gamma_c \left[\frac{1}{\gamma_c}\nabla_T^2 - \frac{4\gamma_c k^2}{L^2} r^2 \right]$$

where γ_c depends on the cavity geometry,

$$\gamma_c = \frac{1}{\sqrt{2R_o/L - 1}}$$

for the cavity in figure B.1. It is interesting to note that the term proportional to r^2 enters the field equation in just the same way as a transversely varying refractive index would. These variations in refractive index tend to confine the field near the centre of the cavity, just as one would expect for curved cavity mirrors.

Following the same procedure as we did already in section 2.2, that is rescaling the frequencies and transverse coordinates and looking for steady states of the resulting scaled Maxwell-Bloch equations, gives a new working equation for the more complicated cavity

$$\left\{ \tan^{-1}\gamma_c \left[\frac{1}{\gamma_c}\left(\frac{d^2}{dr^2} + \frac{1}{r}\frac{d}{dr} - \frac{m^2}{r^2} \right) - 4\gamma_c r^2 \right] + iT + \delta_l - \delta_c + \right. \qquad (2.25)$$

$$\left. \chi D_o(r) \frac{\beta\delta_l - i}{\beta^2\delta_l^2 + 1 + I|R(r)|^2} \right\} R(r) = 0.$$

Let's consider some limiting cases of the above equation. Firstly, let's take the limit of a plane-parallel cavity, $\gamma_c \longrightarrow 0$, under which equation (2.25) reduces, as expected, to the one in the previous sections. Next, consider the limit of a plane pump, $D_o(r) \longrightarrow 1$ and the threshold problem, $I = 0$. In this case, the equation has exact solutions for the threshold, χ_t and frequency, δ_l of the mode given by the indices (p, m)

$$\begin{aligned}\delta_l &= \frac{\delta_c + 4(2p + |m| + 1)\tan^{-1}\gamma_c}{1 + T\beta} \\ \chi_t &= 1 + \beta^2\delta_l^2.\end{aligned}$$

The corresponding mode functions are the Gauss-Laguerre modes

$$R = (2\gamma_c r^2)^{\frac{|m|}{2}} L_p^{|m|}\left(2\gamma_c r^2\right) \exp\left(-\gamma_c r^2\right).$$

Note that the parameter γ_c is scaled in exactly the same way as the γ we used in previous sections to represent the Gaussian pump.

Putting these assumption aside we can use this new working equation (2.25) to find the modes of the combined pump/cavity system. Given a set of system parameters and the widths of the gain profile, γ, and of the fundamental gaussian mode in the cavity, γ_c, we can use a procedure similar to that used in the previous sections to compute mode profiles and thresholds. Figure 2.17 shows the results of this method for a cavity which is 'nearly planar', that is to say the cavity has a fundamental mode much bigger than the gain profile. We have also plotted the mode profiles for the extrema of δ_c in this plot. Compare this figure to figure 2.9 for the purely gain guided case. Recall in section 2.3.2 how we described the index guiding and anti-guiding set up by the pump and therefore how the confinement of the mode depended strongly on the laser frequency. Such features are also visible here. Notice that for $\delta_l > 0$ the pump induced index guiding helps to confine the mode within the fundamental cavity mode. For $\delta_l < 0$ the pump induces an anti-guiding index profile which, as we saw in previous sections, causes the field to spread out into the wings of the transverse plane. In a purely gain guiding system, the mode diffracts with nothing to confine it and so has the characteristic exponential tails. In that combined gain/cavity system the mode diffracts until it 'sees' the cavity mode and it settles on that.

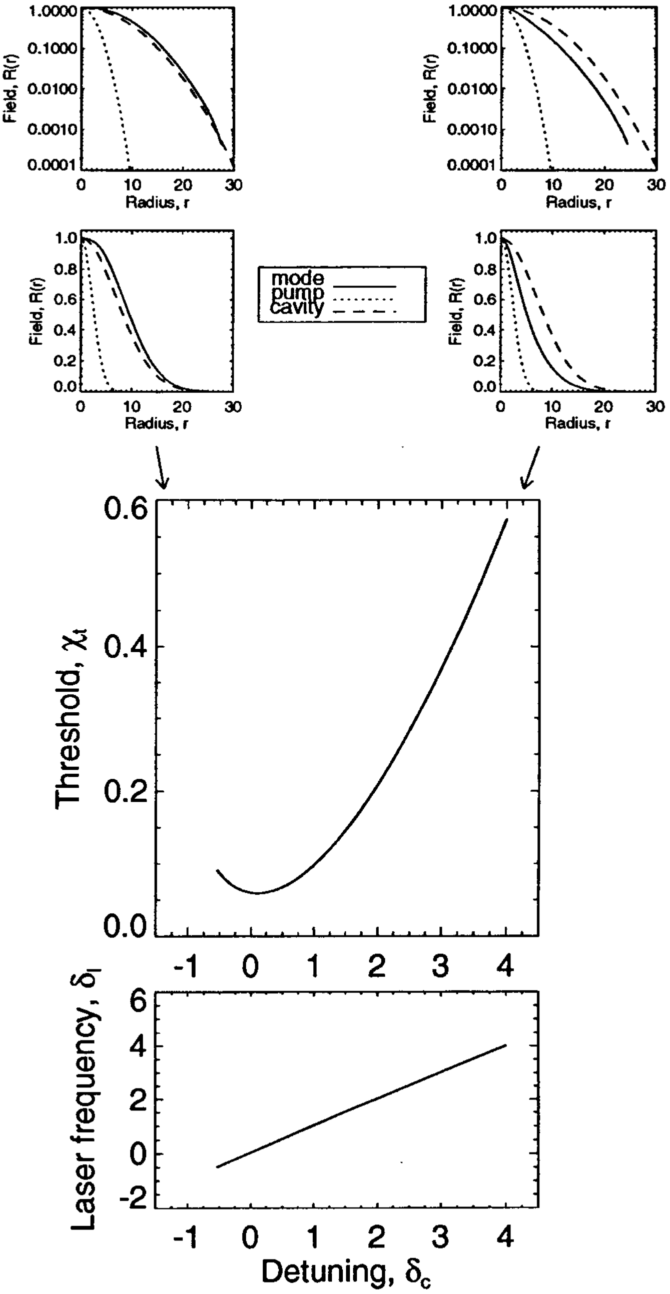

Figure 2.17: The pump threshold and frequency for the combined gain/cavity modes when the fundamental cavity mode is much broader than the gain profile. Parameters are $T = 0.01$, $\beta = 1$, $\gamma = 0.1$, $\gamma_c = 0.01$. *Also shown are the mode profiles, plotted on linear-linear and log-linear scales, at either end of the threshold curve shown.*

Chapter 3

Travelling Waves in Lasers

In this chapter we will study the nature of the transverse pattern formation in an infinitely extended laser system. By infinitely extended we mean that no transverse confinement is imposed by either the cavity – the mirrors are flat and parallel – or by a gain profile – it is uniform and infinitely broad.

It was shown recently that, when the cavity frequency is detuned below the atomic resonance frequency, such a system can show an off-axis emission[26]. Such an off-axis emission means that the transverse field profile has a periodic modulation of its phase. In fact, in their 1992 paper, Jakobsen *et al.*[9] showed that the Maxwell-Bloch equations have an *exact* solution of this form – transverse *travelling waves.*

In this chapter we study these travelling wave solutions, their spatial wavelength, their group velocity and their amplitude as a function of the system parameters. We also study their stability and defects. We use all these analyses to predict the patterns which will be selected by the laser when it is switched on.

3.1 Complex Lorenz Equations

In this chapter we will study the laser equations in complex Lorenz form,

$$
\begin{aligned}
\frac{\partial e}{\partial t} &= ia\nabla_T^2 e - \sigma e + \sigma p, && (3.1)\\
\frac{\partial p}{\partial t} &= re - (1 + i\Delta)p - ne, && (3.2)\\
\frac{\partial n}{\partial t} &= -bn + \frac{1}{2}(ep^* + e^*p). && (3.3)
\end{aligned}
$$

We use this scaling rather than the more usual form for the laser equations[2] partly because it will lead to slightly less complicated expressions for various things later on and partly because this is the scaling that most of the work in this field has been done in. It should be noted that, although the Lorenz equations with real coefficients and variables are well known to produce chaotic motion, to obtain chaos in a laser the parameters would have to be given unphysical values.

How do the variables in this scaling correspond to the ones we have seen already? The field, polarisation and population inversion are defined, in terms of the ones derived in appendix A as,

$$
\begin{aligned}
e &= \sqrt{b}Fe^{i\delta_{cl}t}\\
p &= \frac{2gL\sqrt{b}}{T}Re^{i\delta_{cl}t}\\
n &= 2gL(D_0 - D)/T.
\end{aligned}
$$

New system parameters are defined to be

$$
\begin{aligned}
r &= D_0 2gL/T\\
\sigma &= cT/2L\gamma_\perp\\
b &= \gamma_\parallel/\gamma_\perp\\
\Delta &= (\omega_a - \omega_c)/\gamma_\perp\\
a &= c/2L\gamma_\perp.
\end{aligned}
$$

In summary, the equations describe the behaviour of the complex electric field, e, the complex polarisation, p, and the real population inversion, n, in a two-level ring laser operating on a single longitudinal cavity mode and plane cavity mirrors [6]. A mean field approach has been used to remove the dependence of the longitudinal coordinate and so these variables depend only on the transverse coordinates and time [2, 27]. The parameter a represents the strength of diffraction ; σ is the decay rate of the field due to cavity and linear absorption losses ; b is the population decay rate, and Δ is the detuning between the longitudinal cavity mode frequency and atomic resonance, $\Delta = (\omega_a - \omega_c)/\gamma_\perp$. All decay rates, frequencies and time are scaled to the decay rate of the polarisation, $\gamma_\perp$. The transverse coordinates are scaled to the length $(L/k)^{1/2}$ and the strength of the pumping is characterised by the stress parameter, r.

3.2 Linear Analysis

We begin the analysis of these equations by looking for the stationary states. One obvious stationary state is the trivial one, $e = p = n = 0$, which corresponds to the laser being off. We hope that, for some values of the parameters, this solution will become unstable – otherwise the laser will never work!! To test for such an instability we perform a *linear stability analysis* of this solution. This involves writing the variables as a sum of their stationary value and small perturbations, in this case with a given transverse wavevector, $\mathbf{k}$

$$\begin{aligned} e &= 0 + E e^{i\mathbf{k}.\mathbf{r}} e^{\lambda t} \\ p &= 0 + P e^{i\mathbf{k}.\mathbf{r}} e^{\lambda t} \\ n &= 0 + N e^{\lambda t}. \end{aligned}$$

A positive real part of λ corresponds to growth of the perturbations, a negative part to decay. A non-zero imaginary part of λ corresponds to an oscillation towards or away from the stationary solution. We substitute these expressions into the complex Lorenz equations (3.1) – (3.3) and linearise in terms of the perturbing amplitudes,

E, P, and N, to obtain the set of linearised equations

$$\begin{pmatrix} \lambda + iak^2 + \sigma & -\sigma & 0 \\ -r & \lambda + 1 + i\Delta & 0 \\ 0 & 0 & \lambda + b \end{pmatrix} \begin{pmatrix} E \\ P \\ N \end{pmatrix} = \begin{pmatrix} 0 \\ 0 \\ 0 \end{pmatrix}.$$

This is an eigenvalue problem for the growth rate λ which can be solved by expanding the determinant of the matrix. This leads to characteristic equations for the eigenvalues

$$\lambda = -b$$
$$(\lambda + iak^2 + \sigma)(\lambda + 1 + i\Delta) - \sigma r = 0.$$

Because b is a positive quantity, the eigenvalue from the first equation always leads to decay of the perturbations. The second eigenvalue is not quite so easy to analyse. We're interested in finding the values of the parameters for which the 'off' solution changes from being stable to unstable and so it is the sign of the real part of λ which is important. With this in mind, we write $\lambda = u - i\Omega$ and we will consider only the case of $u = 0$, the case of *neutral stability*. When we substitute $\lambda = -i\Omega$ into the equation for the second eigenvalue and solve for the frequency Ω, and pump parameter, r, we obtain the *neutral stability curve*

$$\Omega = \left(\frac{ak^2 + \sigma\Delta}{\sigma + 1}\right) \tag{3.4}$$
$$r = 1 + \left(\frac{ak^2 - \Delta}{\sigma + 1}\right)^2 \tag{3.5}$$

shown in figure 3.1.

At this point it is interesting to make the analogy between these transverse wavevectors and the bases generally used to represent transverse laser dynamics. In cavities with curved mirrors, it has been shown[28] that for a large range of parameters, the empty cavity modes (Gauss-Laguerre or Gauss-Hermite) are the best basis on which to decompose the laser dynamics. Plane-parallel cavities without a gain profile are on the boundary of cavity stability and the most convenient mode basis to use is

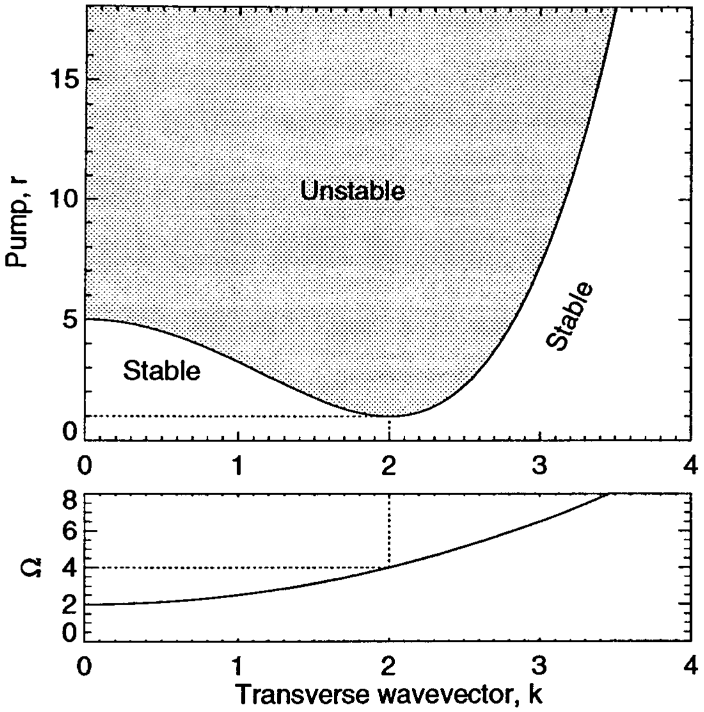

Figure 3.1: Stability diagram for the zero solution. Below the neutral stability curve the zero solution is stable and above the curve, it is unstable. Parameters are $a = 1$; $\sigma = 1$; $\Delta = 4$.

Fourier modes. Note that the Gauss-Laguerre modes, for example, form a discrete basis whereas the Fourier modes are continuous.[1]

So, in laser language, the neutral stability curve gives the first laser threshold for each of these Fourier modes. In this sense it is similar to the threshold curves we produced for gain guided modes in chapter 2. For the parameters chosen for figure 3.1, the transverse wavevector with the lowest threshold is for $k = k_c = 2$ and its threshold value is $r_c = 1$. Let's find, as a function of detuning Δ, which wavevector has the lowest threshold and what its threshold is. It turns out that there is a big difference between the signs of the detuning:

$$\left.\begin{aligned} k_c &= 0 \\ \Omega_c &= \frac{\sigma\Delta}{\sigma+1} \\ r_c &= 1+\frac{\Delta^2}{(\sigma+1)^2} \end{aligned}\right\} \quad \Delta < 0$$

$$\left.\begin{aligned} k_c &= \sqrt{\Delta/a} \\ \Omega_c &= \Delta \\ r_c &= 1 \end{aligned}\right\} \quad \Delta > 0$$

These results are summarised in figure 3.2.

3.2.1 Negative detuning

For $\Delta < 0$ the mode with the lowest threshold is the plane wave, $k_c = 0$. Its threshold and frequency are exactly those derived in section 2.3 in the plane wave analysis. The laser threshold increases from its value at $\Delta = 0$ because the laser is forced to operate at a frequency different from the atomic transition frequency, that is away from the

---

[1] *In chapter 4, for a cavity with curved mirrors, we will do this stability analysis using Gauss-Laguerre modes in place of Fourier modes.*

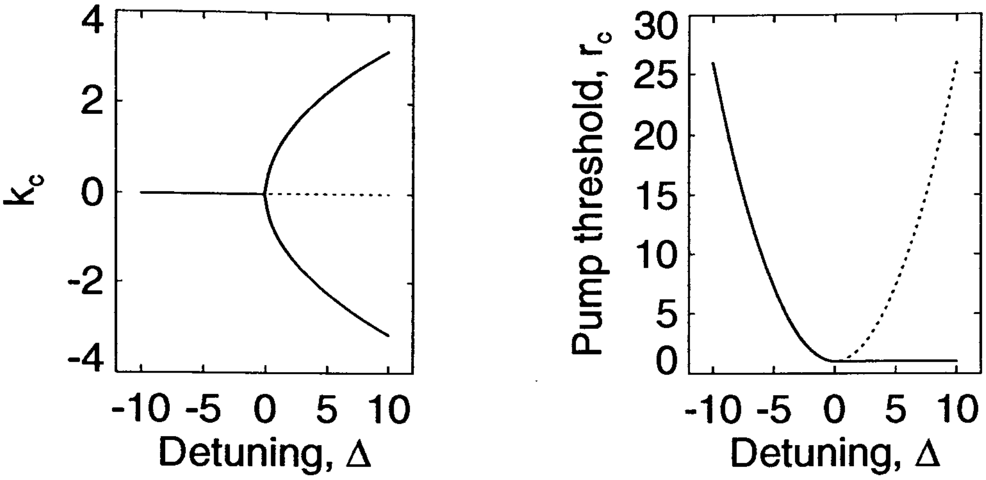

Figure 3.2: The most unstable wavevector, k_c*, as a function of detuning,* Δ*. The laser threshold,* r_c *as a function of detuning. The curves show an asymmetry for positive and negative* Δ*. The dotted lines represent the results of 'standard' plane wave laser theory.*

peak of the gain. Figure 3.3 shows the neutral stability curve for a negatively detuned laser. The figure shows that slightly above threshold a circular band of wavevectors are all above threshold. These modes which are above threshold are known as the *active* modes. The modes below threshold are *passive*[6].

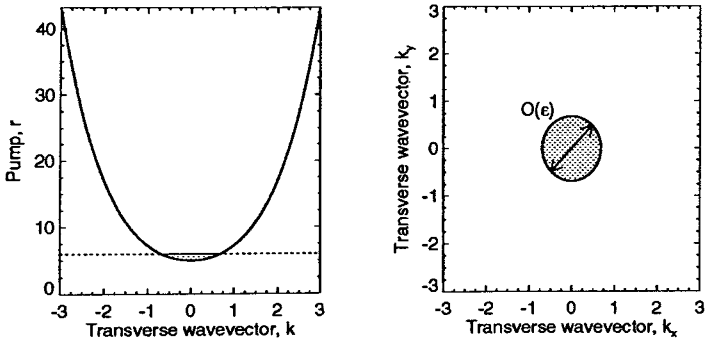

Figure 3.3: The neutral stability curve for negative detunings. Shown also are the transverse wavevectors which are above threshold for a value of the pump 20% *above threshold.*

3.2.2 Positive detuning

For $\Delta > 0$ the mode with the lowest threshold is $k_c = \sqrt{\Delta/a}$. A mode with a nonzero transverse wavevector implies that the laser emits at an angle from the optical axis. The wavevector with the lowest threshold is the one which allows the tilted field to see a cavity exactly resonant with the gain line, $\Omega = \Delta$. To show this by a more physical argument, consider the arrangement of vectors shown in figure 3.4. The vector $\mathbf{k}_{cavity}$ is the longitudinal cavity wavevector we have already used extensively in the derivation of field equations. The vector $\mathbf{k}_c$ is in the transverse plane, that is perpendicular to the cavity wavevector, and is of the correct magnitude, k_c, so that the sum vector, $\mathbf{k}_{atom}$, has a corresponding temporal frequency resonant with the atomic transition frequency, $k_{atom} = \omega_a/c$. Let us now find the condition on $\mathbf{k}_c$ which satisfies these stipulations. Pythagoras' theorem applied to the triangle of wavevectors in figure 3.4 gives

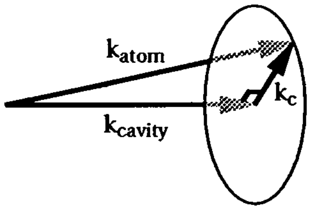

Figure 3.4: The relevant wavevectors in the positively detuned laser. The vector $\mathbf{k}_c$ lies in the transverse plane, that is perpendicular to $\mathbf{k}_{cavity}$. The vector $\mathbf{k}_{atom}$ gives the direction of laser emission. This diagram is not to scale.

$$k_{atom}^2 = k_{cavity}^2 + k_c^2.$$

Under the assumption that $k_c \ll k_{cavity}$ – inherent in the paraxial approximation we have assumed throughout this thesis – we expand in a Taylor series to obtain

$$k_{atom} \approx k_{cavity} + k^2/2k_{cavity}.$$

We now convert the cavity and atomic wavevectors to the equivalent temporal frequencies

$$\frac{\omega_a}{c} \approx \frac{\omega_{cavity}}{c} + \frac{k_c^2 c}{2k_{cavity}}$$

and use the definitions of Δ and a we assumed already to obtain

$$k_c^2 = \frac{\Delta}{a}.$$

This is exactly the expression we found already from the linear analysis, backing up this simple idea of wavevector resonance. Note that the direction of the vector $\mathbf{k}_c$ is not specified, only its magnitude. In figure 3.4, the vector $\mathbf{k}_c$ can lie anywhere on the circle and still give the correct length of the vector, k_{atom}.

Figure 3.5 shows the neutral stability curve for a positively detuned laser and therefore that the active modes form an annulus in k-space, whose radius is k_c – corresponding exactly to the circle shown in figure 3.4. We have been able to predict, from the linear analysis, the threshold for any transverse wavevector and, from that, to infer which wavevectors are above threshold for any given value of the pump parameter. The linear analysis cannot predict which, if any, of these wavevectors will become dominant and characterise the final lasing state. This final state will be determined by a nonlinear competition between the active modes. This competition can be studied through the derivation of *universal amplitude equations* for the system.

3.3 Travelling Wave Solution

We have considered which spatial frequencies grow first under the instability of the nonlasing state. As a further, and important, step, in their 1992 paper Jakobsen *et al.* showed that the Maxwell-Bloch equations have *exact* travelling wave solutions with a general transverse wavevector k_0.

$$e_0 = A \exp\left(i\mathbf{k}_0.\mathbf{r} - i\Omega t\right)$$

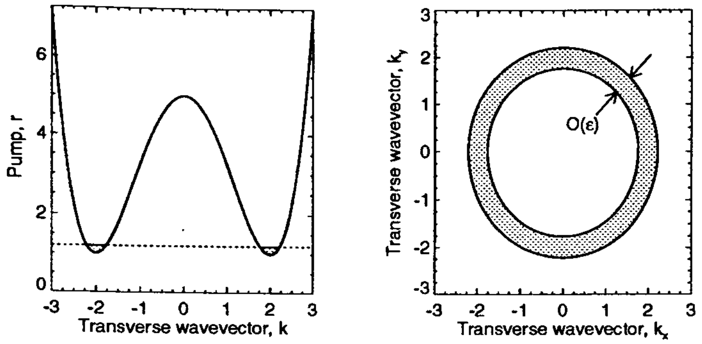

Figure 3.5: The neutral stability curve for positive detunings. Shown also are the transverse wavevectors which are above threshold for a value of the pump 20% *above threshold.*

$$
\begin{aligned}
p_0 &= \Lambda e_0^* \\
n_0 &= r - |\chi|^2
\end{aligned}
$$

with

$$
\begin{aligned}
\Lambda &= 1 - i(\Delta - \Omega), \\
\Omega &= \frac{\sigma\Delta + ak_0^2}{\sigma + 1}, \\
|A|^2 &= bn_0.
\end{aligned}
$$

The existence of these solutions is somewhat novel and by no means expected ; for example, no exact Gaussian solution exists for a cavity with curved mirrors. Note that, just as we would expect, the condition $|A|^2 = 0$ gives the neutral stability curve (3.5). These exact solutions will be very important later on in this chapter when we study the stability of travelling wave solutions.

3.4 Amplitude Equations

The derivation of amplitude equations[7, 10] relies on the fact that the pump parameter, r, is close to its threshold value. This 'closeness' is captured in the definition of a *smallness parameter* $\varepsilon = (r-1)^{1/2}$. Figure 3.6 shows a close-up of the minimum of the neutral stability curve – figure 3.1 – and the wavevectors which can be excited. Because, for ε small and Δ not close to zero, the neutral stability curve is nearly parabolic, the band of active modes is of width $\mathcal{O}(\varepsilon)$. This means that if, for example, we write the laser field at any point in time as an amplitude multiplying a Fourier mode with wavevector k_c,

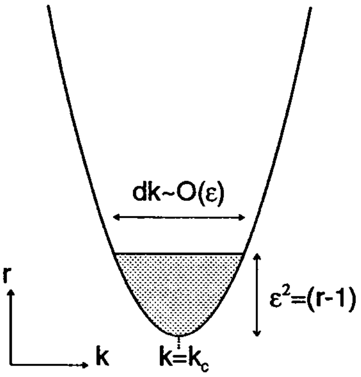

Figure 3.6: The band of k-vectors excited close to threshold. The smallness parameter, ε is defined in terms of the distance above threshold and, since the neutral stability curve is nearly parabolic close to its minimum, the width of the unstable band is $\mathcal{O}(\varepsilon)$.

$$e = A(x,t)e^{ik_c x},$$

then the function $A(x,t)$ must be made up of spatial Fourier modes with wavevectors no greater than $dk \approx \varepsilon$. In real space, this means that the function $A(x,t)$ must vary very slowly in space. Another way of looking at it is that the Fourier spectrum of $A(x,t)$ is very narrow and so it must have only slow variations in real space. A similar argument applied in the temporal frequency/time domains can be used to show that $A(x,t)$ must also vary slowly in time.

To obtain amplitude equations which fully describe the dynamics close to threshold we should expand the variables of the problem in all of the active modes. In the laser case and in 1D this is relatively simple and means having an amplitude for the wavevectors $\pm k_c$. In 2D, there is a continuum of active modes at threshold forming a ring in k-space and we would require an infinite number of mode amplitudes. This is formally possible but gives little physical insight. The derivation of amplitude equations in 2D almost always requires the dynamics to be decomposed onto a finite set of active modes. This obviously restricts the classes of patterns which are assumed to be present for the derivation of the amplitude equations.

In this chapter, we will first consider the derivation of amplitude equations for a one transverse dimension laser. These will show the basic features of the nonlinear competition leading to a final pattern. The results of the amplitude equations will be checked by numerical simulation of the complex Lorenz equations. When we try to apply the results of the 1D amplitude equations to describe 2D numerical simulations we will see that, by using these simplified two mode amplitude equations, we have omitted a class of meta-stable 2D solutions. We will rectify this by writing equations for four modes.

3.5 Two mode amplitude equations

Let's now consider the derivation of a set of equations for the amplitudes of the waves travelling along the positive and negative x-directions. The analysis will be much easier if we write the system of Lorenz equations (3.1)–(3.3) in vector form by defining

$$\mathbf{v} = \begin{pmatrix} e \\ p \\ n \end{pmatrix}.$$

The Lorenz system now becomes

$$\frac{\partial \mathbf{v}}{\partial t} = \mathcal{L}\mathbf{v} + \mathbf{N}(\mathbf{v}) \tag{3.6}$$

where $\mathcal{L}$ is a linear operator and $\mathbf{N}$ is the nonlinear part of the equations:

$$\mathcal{L} = \begin{pmatrix} ia\nabla_T^2 - \sigma & \sigma & 0 \\ r & -(1+i\Delta) & 0 \\ 0 & 0 & -b \end{pmatrix}$$

$$\mathbf{N} = \begin{pmatrix} 0 \\ -ne \\ \frac{1}{2}(ep^* + e^*p) \end{pmatrix}.$$

The method now involves expanding the variables and the fundamental control parameter, r, of the problem in *multiple scales*

$$t = T_1 + T_2/\varepsilon + T_3/\varepsilon^2 + \dots \tag{3.7}$$

$$x = X_1 + X_2/\varepsilon + \dots \tag{3.8}$$

$$r = r_c + \varepsilon^2 + \dots \tag{3.9}$$

$$\mathbf{v} = \varepsilon\mathbf{v}_1 + \varepsilon^2\mathbf{v}_2 + \varepsilon^3\mathbf{v}_3 + \dots \tag{3.10}$$

where we regard the T_js and X_js as independent variables. In this way we are separating the problem into a set of problems each varying at a different rate in space and time. If the value of ε is small then these problems will be distinct and the approximations good – if ε is large then this separability will not be justified. Similarly expanding the linear operator and nonlinear terms gives

$$\mathcal{L} = \mathcal{L}_1 + \varepsilon\mathcal{L}_2 + \varepsilon^2\mathcal{L}_3 + \dots = \begin{pmatrix} ia\frac{\partial^2}{\partial X_1^2} - \sigma & \sigma & 0 \\ r_c & -(1+i\Delta) & 0 \\ 0 & 0 & -b \end{pmatrix} +$$

$$\varepsilon \begin{pmatrix} 2ia\frac{\partial}{\partial X_1}\frac{\partial}{\partial X_2} & 0 & 0 \\ 0 & 0 & 0 \\ 0 & 0 & 0 \end{pmatrix} +$$

$$\varepsilon^2 \begin{pmatrix} ia\frac{\partial^2}{\partial X_2^2} & 0 & 0 \\ 1 & 0 & 0 \\ 0 & 0 & 0 \end{pmatrix} + \dots$$

$$\mathbf{N} = \mathbf{N}_1 + \varepsilon\mathbf{N}_2 + \varepsilon^2\mathbf{N}_3 + \ldots = \underline{0} + \varepsilon\begin{pmatrix} 0 \\ -e_1 n_1 \\ \frac{1}{2}(e_1 p_1^* + e_1^* p_1) \end{pmatrix} + \varepsilon^2\begin{pmatrix} 0 \\ -(e_1 n_2 + e_2 n_1) \\ \frac{1}{2}(e_1 p_2^* + e_2 p_1^* + c.c.) \end{pmatrix} + \ldots$$

When we substitute these into (3.6) and separate terms at different orders in ε we obtain

$$\left(\frac{\partial}{\partial T_1} - \mathcal{L}_1\right)\mathbf{v}_1 = \underline{0}, \tag{3.11}$$

$$\left(\frac{\partial}{\partial T_1} - \mathcal{L}_1\right)\mathbf{v}_2 = \mathbf{S}_2, \tag{3.12}$$

$$\left(\frac{\partial}{\partial T_1} - \mathcal{L}_1\right)\mathbf{v}_3 = \mathbf{S}_3, \tag{3.13}$$

where the source terms on the right hand sides

$$\begin{aligned} \mathbf{S}_2 &= -\frac{\partial \mathbf{v}_1}{\partial T_2} + \mathcal{L}_2\mathbf{v}_1 + \mathbf{N}_2, \\ \mathbf{S}_3 &= -\frac{\partial \mathbf{v}_1}{\partial T_3} - \frac{\partial \mathbf{v}_2}{\partial T_2} + \mathcal{L}_3\mathbf{v}_1 + \mathcal{L}_2\mathbf{v}_2 + \mathbf{N}_3. \end{aligned}$$

The problem has now been decomposed into a set of equations, (3.11) – (3.13), each governing variables which vary on a different scale in space and time. The subscript of each variable represents at what scale the variable is considered to vary. For example, the subscript '1' represents the scale of the underlying Fourier mode, that is the scale of k_c. The subscript '2' is used on variables which vary on space/time scales $1/\varepsilon$ times larger/slower than the ones with '1'. The variables with subscript '3' vary on a space and time scale another factor of $1/\varepsilon$ larger, and so on. For this reason, this method of deriving amplitude equations is sometimes known as *multiple scales analysis.*

3.5.1 The Fredholm alternative

Let us now consider the solution of this set of equations at each order. To give us some idea of what to expect, let us consider first a simpler test problem not with operator equations but with a scalar, real, 2 × 2 matrix, M. At the zeroth order, mirroring equation (3.11), we have

$$M\mathbf{X}_1 = \begin{pmatrix} a & b \\ c & d \end{pmatrix} \mathbf{X}_1 = \mathbf{0}. \tag{3.14}$$

If this is to have a nontrivial solution the determinant of M must be zero, implying

$$ad - bc = 0.$$

The operators on the left hand sides of equations (3.11) – (3.13) are all equal and so, in our simplified matrix system, the equation mirroring (3.12) is

$$\begin{aligned} M\mathbf{X}_2 &= \mathbf{S}_2 && (3.15) \\ \Rightarrow \begin{pmatrix} a & b \\ c & d \end{pmatrix} \begin{pmatrix} x_1 \\ y_1 \end{pmatrix} &= \begin{pmatrix} f \\ g \end{pmatrix}. \end{aligned}$$

We hope to require that this equation also has a nontrivial solution. To illuminate the discussion slightly think of the two equations to be representing straight lines in the (x_1, y_1) plane:

$$\begin{aligned} y_1 &= f/b - ax_1/b \\ y_2 &= g/d - cx_1/d. \end{aligned}$$

A solution to these simultaneous equations is obtained where the lines cross. One possibility to ensure that the lines do cross is to require that their gradients are different, that is

$$a/b \neq c/d$$

or, rearranging,

$$ad - bc \neq 0.$$

However, when we considered the homogeneous equation (3.14) we explicitly showed that this was not the case ; that is to say that these two lines are parallel. The only other possibility to obtain a crossing of the lines is for them to be coincident ; that is that

$$f/b = g/d.$$

If we use $ad = bc$ to rearrange this condition slightly we obtain

$$cf - ag = 0. \tag{3.16}$$

Now, as a bit of a leap of faith, consider the homogeneous adjoint problem

$$M^{\dagger}\tilde{\mathbf{X}} = \begin{pmatrix} a & c \\ b & d \end{pmatrix} \begin{pmatrix} \tilde{x} \\ \tilde{y} \end{pmatrix} = \mathbf{0}$$

whose solutions lie along the vector

$$\begin{pmatrix} \tilde{x} \\ \tilde{y} \end{pmatrix} = \begin{pmatrix} c \\ -a \end{pmatrix}.$$

We now see that the condition, equation (3.16), for a non-trivial solution for $\mathbf{X}_2$ in (3.15) is exactly that the scalar product

$$\begin{pmatrix} c \\ -a \end{pmatrix} \cdot \begin{pmatrix} f \\ g \end{pmatrix} = \tilde{\mathbf{X}}.\mathbf{S}_2 = 0.$$

The generalisation of this argument to higher-dimensions is not so intuitive but the general result is the same[10]. Given that the homogeneous, multi-dimensional problem

$$M\mathbf{X} = \mathbf{0}$$

has non-trivial solutions, the inhomogeneous problem

$$M\mathbf{X} = \mathbf{S}$$

has non-trivial solutions if and only if

$$\tilde{\mathbf{X}}.\mathbf{S} = 0$$

where $\tilde{\mathbf{X}}$ is a solution of the adjoint problem

$$M^{\dagger}\tilde{\mathbf{X}} = 0.$$

This condition is known as the *Fredholm alternative*[10].

This approach, however, does not leave us with much feeling for the physical reasons behind why the Fredholm theorem is so useful and so necessary in this derivation. For that, let us resort to an analogy from classical mechanics, the weakly driven oscillator given by the equation

$$\left(\frac{\partial^2}{\partial t^2} + \omega^2\right)\theta = \varepsilon \sin \omega t. \tag{3.17}$$

The solution of such a differential equation, analagous to that of equation (3.12), is found by first solving the homogeneous problem,

$$\left(\frac{\partial^2}{\partial t^2} + \omega^2\right)\theta = 0,$$

to obtain, within a phase, the homogeneous solution

$$\theta_h = A \sin \omega t.$$

This process is analagous to the solution of equation (3.11) in the derivation of the amplitude equations. The next stage in solving the differential equation (3.17), analagous to solving equation (3.12) is to find a particular solution, θ_p. Because the right hand side of (3.17) contains terms of the same form as ones in the solution of the homogeneous problem we need a particular solution of the form

$$\theta_p = \frac{-\varepsilon}{2\omega} t \cos \omega t.$$

The solution of the equation (3.17) is then given by $\theta_h + \theta_p$ which has a term which grows linearly, and without bound, in time. This is fine for the classical oscillator but for the solution v_2, in equation (3.12), it is a problem. We have assumed that v_2 is a term in a perturbation expansion of v and so, if v_2 shows such *secular growth* then this expansion will be invalidated after some finite time. The Fredhold alternative requires that source terms at each order have no terms which lead to such growth ; a *solvability condition* follows at each order.

Armed with this information, let's go back and tackle the solution of the operator equations at each order.

3.5.2 Order ε

The equation at order ε, that is equation (3.11), gives the first order solution which we will consider to be a superposition of only waves travelling in the positive and negative x-directions. These are denoted $\mathcal{F}$ and $\mathcal{B}$ to indicate forward and backward travelling waves. This is the place where we neglect the effects of all active modes other than these two. Note that if we consider only one transverse dimension then these are all the active modes. The first order correction

$$\mathrm{v}_1 = \begin{pmatrix} 1 \\ 1 \\ 0 \end{pmatrix} \left[\mathcal{F}(X_2, T_2, T_3) e^{ik_c X_1} + \mathcal{B}(X_2, T_2, T_3) e^{-ik_c X_1} \right] e^{-i\Omega T_1} \qquad (3.18)$$

where $\Omega = \Delta$, $k_c = \sqrt{\Delta / a}$ and $\mathcal{F}$ and $\mathcal{B}$ are functions which can only vary on the long space and time scales. Their variation in time in space is encapsulated by their dependence on the slow space and time scales X_2, T_2 and T_3. This expression for $\mathbf{v}_1$ is just the solution of the linearised Lorenz equations – the solution at threshold – and represents travelling waves in the field and the polarisation.

3.5.3 Order ε^2

At second order we have the equation (3.12)

$$\left(\frac{\partial}{\partial T_1} - \mathcal{L}_1\right)\mathbf{v}_2 = -\frac{\partial \mathbf{v}_1}{\partial T_2} + \mathcal{L}_2\mathbf{v}_1 + \mathbf{N}_2.$$

We now use what we have already learned about the zeroth order solution to obtain

$$\left(\frac{\partial}{\partial T_1} - \mathcal{L}_1\right)\mathbf{v}_2 = \mathbf{S}_2 = -\begin{pmatrix}1\\1\\0\end{pmatrix}\left[\frac{\partial \mathcal{F}}{\partial T_2}e^{ik_cX_1} + \frac{\partial \mathcal{B}}{\partial T_2}e^{-ik_cX_1}\right]e^{-i\Omega T_1} +$$
$$2ia\begin{pmatrix}1\\0\\0\end{pmatrix}\left[ik_c\frac{\partial \mathcal{F}}{\partial X_2}e^{ik_cX_1} - ik_c\frac{\partial \mathcal{B}}{\partial X_2}e^{-ik_cX_1}\right]e^{-i\Omega T_1} +$$
$$\begin{pmatrix}0\\0\\1\end{pmatrix}\left|\mathcal{F}e^{ik_cX_1} + \mathcal{B}e^{-ik_cX_1}\right|^2,$$

where we've called the right hand side of this expression, $\mathbf{S}_2$, to stand for 'source term'. Now comes the clever bit of multiple scales analysis. At this stage, we apply the Fredholm theorem and require that the source term, $\mathbf{S}_2$ is orthogonal to the solution of the adjoint problem

$$\left(\frac{\partial}{\partial T_1} - \mathcal{L}_1\right)^{\dagger}\tilde{\mathbf{v}} = \mathbf{0}.$$

The usual definition of the adjoint operator is given in terms of basis vectors $|X\rangle$ and $|Y\rangle$,

$$\langle Y|M^{\dagger}X\rangle = \langle MY|X\rangle,$$

but in our case, the application of the operator $\left(\frac{\partial}{\partial T_1} - \mathcal{L}_1\right)$ to the vectors $\mathbf{v}_i$ reduce it to matrix form allowing us to use the matrix definition of the adjoint as the conjugate transpose. Doing this leads to the expression for the solution of the adjoint problem

$$\tilde{\mathbf{v}} = \begin{pmatrix} 1 \\ \sigma \\ 0 \end{pmatrix} \left[\mathcal{F}e^{ik_cX_1} + \mathcal{B}e^{-ik_cX_1}\right] e^{i\Omega T_1}.$$

The Fredholm alternative, $\tilde{\mathbf{v}}.\mathbf{S}_2 = \mathbf{0}$, gives the *solvability conditions* at this order

$$\begin{aligned} -(\sigma+1)\frac{\partial \mathcal{F}}{\partial T_2} - 2ak_c\frac{\partial \mathcal{F}}{\partial X_2} &= 0 \\ (\sigma+1)\frac{\partial \mathcal{B}}{\partial T_2} + 2ak_c\frac{\partial \mathcal{B}}{\partial X_2} &= 0. \end{aligned}$$

These expressions give the travelling wave velocities,

$$v_g = \pm\frac{2\sqrt{a\Delta}}{\sigma+1}, \tag{3.19}$$

but do not model any of the effects of growth of the amplitudes or their nonlinear saturation. To include these we must go to the next order in ε. Before doing this, we use equation (3.12) and the solvability conditions to solve for

$$\mathbf{v}_2 = \begin{pmatrix} 0 \\ \left(-\frac{\partial \mathcal{F}}{\partial T_2}e^{ik_cX_1} - \frac{\partial \mathcal{B}}{\partial T_2}e^{-ik_cX_1}\right)e^{-i\Omega T_1} \\ \left(|\mathcal{F}e^{ik_cX_1} + \mathcal{B}e^{-ik_cX_1}|^2\right)/b \end{pmatrix}.$$

We see a correction to the population inversion and the first appearance of the dependence of $\mathcal{F}$ and $\mathcal{B}$ on the slow spatial and temporal scales.

3.5.4 Order ε^3

We now have everything we need to go on to the next order in ε. We follow the same prescription as before, inserting all the know quantities into equation (3.13) to obtain

$$\begin{aligned}
\left(\frac{\partial}{\partial T_1} - \mathcal{L}_1\right)\mathbf{v}_3 \;&=\; \mathbf{S}_3 = -\begin{pmatrix}1\\1\\0\end{pmatrix}\left[\frac{\partial\mathcal{F}}{\partial T_3}e^{+} + \frac{\partial\mathcal{B}}{\partial T_3}e^{-}\right]e^{-i\Omega T_1}\\
&+ \begin{pmatrix}0\\1\\\square\end{pmatrix}\left[\frac{\partial^2\mathcal{F}}{\partial T_2^2}e^{+} + \frac{\partial^2\mathcal{B}}{\partial T_2^2}e^{-}\right]e^{-i\Omega T_1}\\
&+ ia\begin{pmatrix}1\\0\\0\end{pmatrix}\left[\frac{\partial^2\mathcal{F}}{\partial X_2^2}e^{+} + \frac{\partial^2\mathcal{B}}{\partial X_2^2}e^{-}\right]e^{-i\Omega T_1}\\
&+ \begin{pmatrix}0\\1\\0\end{pmatrix}\left[\mathcal{F}e^{+} + \mathcal{B}e^{-}\right]e^{-i\Omega T_1}\\
&- \begin{pmatrix}0\\1\\\square\end{pmatrix}\left[\mathcal{F}\left(|\mathcal{F}|^2 + 2|\mathcal{B}|^2\right)e^{+} + \mathcal{B}\left(|\mathcal{B}|^2| + 2|\mathcal{F}|^2\right)e^{-}\right]e^{-i\Omega T_1}/b
\end{aligned}$$

where, to simplify the notation, we have written e^{+} to represent $e^{ik_cX_1}$ and e^{-} to represent $e^{-ik_cX_1}$. The terms represented by squares, ($\square$), are complicated expressions which will be unimportant to the final result. As before, we apply the Fredholm theorem to the source term in this equation to obtain the solvability conditions at third order

$$-(\sigma+1)\frac{\partial\mathcal{F}}{\partial T_3} + \sigma\frac{\partial^2\mathcal{F}}{\partial T_2^2} + ia\frac{\partial^2\mathcal{F}}{\partial X_2^2} + \sigma\mathcal{F} - \sigma\mathcal{F}(|\mathcal{F}|^2 + 2|\mathcal{B}|^2)/b = 0, \qquad (3.20)$$

$$-(\sigma+1)\frac{\partial\mathcal{B}}{\partial T_3} + \sigma\frac{\partial^2\mathcal{B}}{\partial T_2^2} + ia\frac{\partial^2\mathcal{B}}{\partial X_2^2} + \sigma\mathcal{B} - \sigma\mathcal{B}(|\mathcal{B}|^2 + 2|\mathcal{F}|^2)/b = 0. \qquad (3.21)$$

These expressions govern the evolution of the amplitudes in slow time and space. As expected, they contain essential terms representing linear growth and nonlinear saturation. In principle, we could carry on this expansion to higher powers of ε but the algebra becomes horrendous. The terms relevant to the dynamics are present at this order and corrections at higher order should not change the nature of the solutions obtained.

3.5.5 Unscaling the equations

The equations (3.20) and (3.21) contain derivatives in the slow time and space scales only. We'd like to have an equation with derivatives in real space and time. Accordingly, we use the expansions (3.7)–(3.10), and the solvability condition at second order to unscale these equations. We also note that $\mathcal{F}$ and $\mathcal{B}$ are terms of order $1/\varepsilon$ – see equations (3.10) and (3.18) – and we'd like to deal with terms of order 1. To do this we define new amplitudes

$$\begin{aligned} F &= \varepsilon\mathcal{F} \\ B &= \varepsilon\mathcal{B}. \end{aligned}$$

The equations which emerge are the coupled Newell-Whitehead-Segel equations[6, 9, 29, 30] for the forward and backward travelling wave amplitudes:

$$(\sigma+1)\frac{\partial F}{\partial t} - 2ak_c\frac{\partial F}{\partial x} = \left[ia + \frac{4a^2k_c^2\sigma}{(\sigma+1)^2}\right]\frac{\partial^2 F}{\partial x^2} + \sigma(r-1)F - \frac{\sigma}{b}(|F|^2 + 2|B|^2)F \quad (3.22)$$

$$(\sigma+1)\frac{\partial B}{\partial t} + 2ak_c\frac{\partial B}{\partial x} = \left[ia + \frac{4a^2k_c^2\sigma}{(\sigma+1)^2}\right]\frac{\partial^2 B}{\partial x^2} + \sigma(r-1)B - \frac{\sigma}{b}(|B|^2 + 2|F|^2)B. \quad (3.23)$$

The terms on the left of these equations give the forward or backward travelling nature of the amplitudes. Disturbances in the amplitudes propagate with the group velocity of the travelling waves. The terms involving second order derivatives in space give diffractive and diffusive terms for the amplitudes. Note that the coefficient of diffusion is always positive. The equations contain linear growth terms which, as expected, are proportional to the value of the pump minus its threshold value. The final terms contain the effects of nonlinearity – self-amplitude and cross-amplitude modulation. These are the terms responsible for determining the nature of the nonlinear competition between the forward and backward travelling waves.

3.5.6 Slow scales in x and y

In deriving the amplitude equations thus far, we considered two active modes on the critical circle. Through the procedure of multiple scales analysis we have produced equations for the slowly varying amplitudes of these modes. The amplitudes may vary slowly in time and in space along the direction of the modes themselves – we chose x already. Through the effects of diffraction we should expect that the amplitudes of the modes may also change slowly in the y-direction.

Following Manneville[10], if we assume that $\mathrm{k} = (k_c + \delta k_x)\hat{\mathrm{x}} + \delta k_y \hat{\mathrm{y}}$ then the diffraction operator, $i\nabla^2$, applied to a field with such wavenumbers will lead to terms of the type

$$((k_c + \delta k_x)\hat{\mathrm{x}} + \delta k_y \hat{\mathrm{y}})^2 = k_c^2 + 2k_c\delta k_x + \delta k_x^2 + \delta k_y^2.$$

If we compare the lowest order terms in the perturbations δk_x and δk_y then we see that

$$\delta k_x \sim \delta k_y^2,$$

and so, if the width of the unstable band in the x-direction is of $\mathcal{O}(\varepsilon)$ then the width in the y-direction is $\mathcal{O}(\varepsilon^{1/2})$. This is shown diagrammatically in figure 3.7. Now that

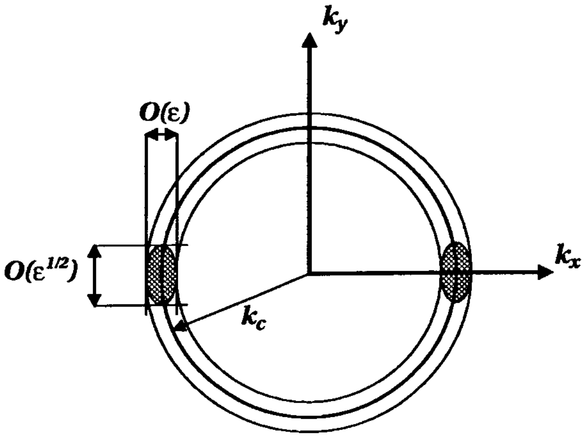

Figure 3.7: The unstable modes for the two mode amplitude equations with slow scales in x and y.

we have found the widths of the unstable band in both directions we can conceivably derive amplitude equations with slow scales in both these directions. The derivation is very similar to that above except that we also expand the y coordinate in multiple scales,

$$y = Y_1 + Y_2/\sqrt{\varepsilon} + \ldots.$$

We make all the substitutions of the expanded variables, separate orders of ε and, at each order derive a solvability condition. The resulting condition at third order is

$$\begin{aligned}
(\sigma+1)\frac{\partial F}{\partial t} &- 2ak_c\frac{\partial F}{\partial x} = \\
& ia\nabla_T^2 F - \frac{\sigma a^2}{(\sigma+1)^2}\left(2ik_c\frac{\partial}{\partial x} + \frac{\partial^2}{\partial y^2}\right)^2 F + \sigma(r-1)F - \frac{\sigma}{b}(|F|^2 + 2|B|^2)F \\
(\sigma+1)\frac{\partial B}{\partial t} &+ 2ak_c\frac{\partial F}{\partial x} = \\
& ia\nabla_T^2 B - \frac{\sigma a^2}{(\sigma+1)^2}\left(2ik_c\frac{\partial}{\partial x} + \frac{\partial^2}{\partial y^2}\right)^2 B + \sigma(r-1)B - \frac{\sigma}{b}(|B|^2 + 2|F|^2)B
\end{aligned}$$

We can see that in the limit $\partial/\partial y \to 0$ then we obtain the amplitude equations already derived, (3.22) and (3.23).

3.6 Nonlinear competition of active modes

In section 3.2.2 our motivation for deriving amplitude equations was that the linear analysis could not describe the nonlinear competition of the active modes. Let us now use the amplitude equations to establish the nature of this nonlinear competition.

To simplify the analysis we will use the spatially independent form of the amplitude equations (3.22) and (3.23)

$$\begin{aligned}
(\sigma+1)\frac{\partial F}{\partial t} &= \sigma(r-1)F - \frac{\sigma}{b}(|F|^2 + 2|B|^2)F, & (3.24) \\
(\sigma+1)\frac{\partial B}{\partial t} &= \sigma(r-1)B - \frac{\sigma}{b}(|B|^2 + 2|F|^2)B. & (3.25)
\end{aligned}$$

The stationary states of this system of coupled ordinary differential equations are shown, symbolically in table 3.1 and graphically in figure 3.8. The stability of these stationary states can be calculated in the usual way and shows that, above threshold, only the travelling wave solutions are stable. This is indicated in the bifurcation diagram in figure 3.8 which shows stable solutions as full lines and unstable ones as dotted lines. Note that the stability analysis of these amplitude equations checks only for stability to perturbations in the direction of the amplitudes themselves.

$\lvert F\rvert^2 = 0$	$\lvert B\rvert^2 = 0$	nonlasing solution
$\lvert F\rvert^2 = b(r-1)/3$	$\lvert B\rvert^2 = b(r-1)/3$	lasing, standing wave solution
$\lvert F\rvert^2 = b(r-1)$	$\lvert B\rvert^2 = 0$	lasing, forward travelling wave solution
$\lvert F\rvert^2 = 0$	$\lvert B\rvert^2 = b(r-1)$	lasing, backward travelling wave solution

Table 3.1: The stationary states of the space independent, two mode, amplitude equations.

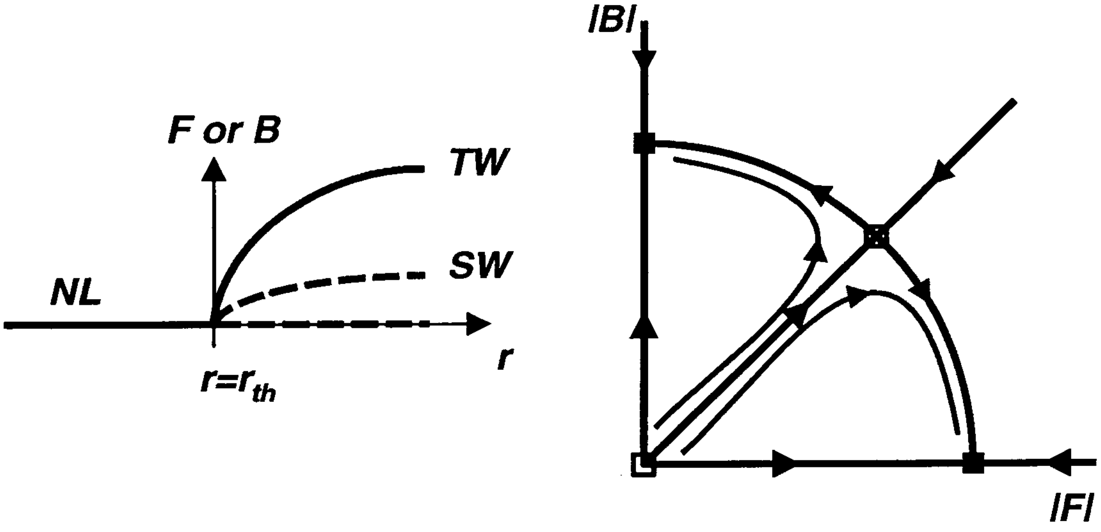

Figure 3.8: On the left, the stationary states of the space independent amplitude equations as a function of the pump parameter, r. The full lines show stable solutions (the travelling waves) ; the dotted lines show unstable solutions (the standing waves and non-lasing state.) On the right, portraits in the ($|F|, |B|$) phase space, showing the trajectories away from unstable solutions and into stable ones.

So, what should we expect to see when the laser is switched on? The linear stability analysis of the nonlasing solution predicts that wavevectors with modulus k_c are unstable and should see growth. As the energy in these modes grows, the amplitude equations for forward and backward travelling waves predict that travelling waves should win out, leading to a final state which consists of only one mode. What physical reasons are there for a travelling wave winning out over a standing wave? A standing wave consists of a field intensity which is modulated in space. In regions where the field intensity is low, the population inversion is not used to the full. A travelling wave, however, has intensity constant in space and so uses the available population inversion as efficiently as is possible. For this reason, the travelling wave is preferred by the laser.

Let's consider a numerical simulation of the complex Lorenz equations with one transverse dimension to see what actually happens. We use periodic boundary conditions and a split-step Fourier method, as described in appendix C, with initial conditions of some noise around the nonlasing solution. The results in figure 3.9 show a 'snapshot' of the modulus of the electric field $|e(x)|$ as a function of x and of the modulus of the Fourier transform of e as a function of k at four values of the time, t. In the early stages of the simulation, the field amplitude is very small – note the scale on the vertical axis of the first plots – and the linear approximation to the equations is good. As predicted by the linear stability analysis, the modes with $k = \pm k_c = \pm 2$ grow. As the simulation proceeds these modes compete and eventually, in this case, the one with $k = -2$ wins out and saturates to a constant value. The mode which does win out is random and depends entirely on the noise in the initial condition.

It is relatively easy to show, from the amplitude equations, that the mode which has a larger value must continue to have a larger value. Consider the space independent amplitude equations (3.24) – (3.25) and write them in a form

$$\frac{\partial F}{\partial t} = G_F\, F$$
$$\frac{\partial F}{\partial t} = G_B\, B$$

where the Gs are intended to connote 'Gain'. These gain terms depend on the system parameters and on the instantaneous values of the forward and backward wave intensities. Consider an initial condition $B = A$ and $F = A + \varepsilon$ where A is some arbitrary, perhaps small, amplitude and ε has a small positive value to indicate a slight excess of forward over backward waves in the initial condition. Given this ansatz we can show that the forward wave has a larger gain than the backward one:

$$G_F - G_B = \sigma\varepsilon(\varepsilon + 2A)/b$$

and so will grow faster. The tiniest imbalance therefore in the initial condition will cause the larger amplitude to grow disproportionately and eventually quash the other.

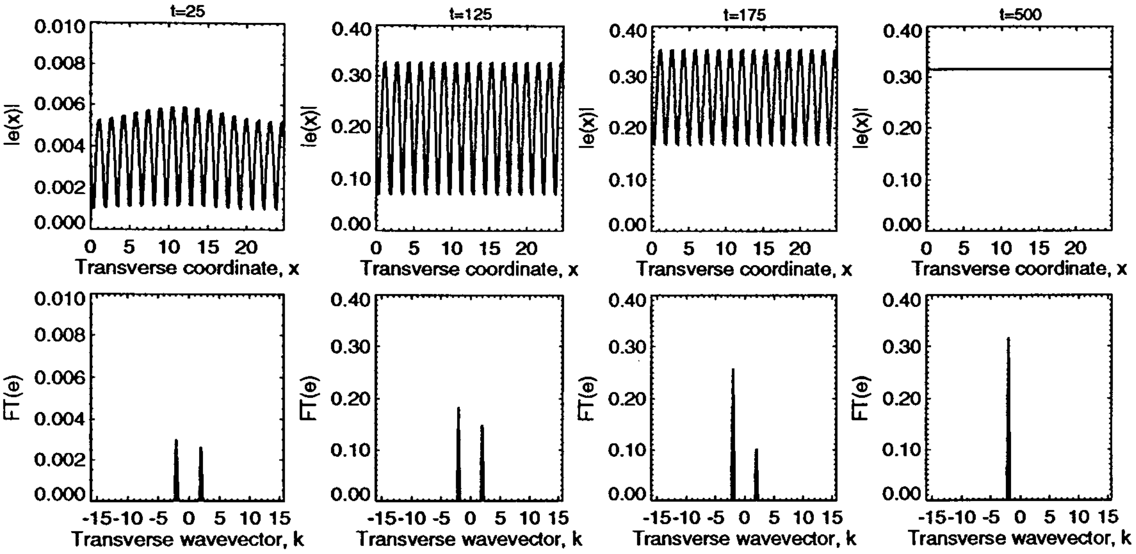

Figure 3.9: The results of a one transverse dimension numerical simulation of the complex Lorenz equations. The boundary conditions are periodic and the initial conditions are noise around zero. Two opposite travelling waves are excited in the linear regime (t=25) ; their amplitudes grow in time (t=125,t=175) ; they undergo a nonlinear competition and, because it had the larger initial amplitude, the one with $k = -2$ wins out (t=500). Parameters are $a = 1$, $b = 1$, $\Delta = 4$, $\sigma = 1$, $r = 1.1$.

The amplitude equations we have derived describe the nonlinear competition of a set of oppositely travelling waves. In two transverse dimensions the linear analysis has shown that a whole ring of k-vectors become active at threshold. The amplitude equations do not describe the coupling and competition between this continuum of modes. On the basis of the results in one dimension we might expect that the ring of active modes might collapse to a single wavevector under nonlinear competition. Figure 3.10 shows the results of a two dimensional numerical simulation of the complex

Lorenz equations. The top row shows the amplitude of the electric field as a function of the transverse coordinates at four points in its time evolution. Black corresponds to low intensity and white to high. The bottom row shows the amplitude of the field's Fourier transform as a function of transverse wavevector. To make the plot clearer we have reversed the grey scale used so that black means high intensity.[2]

The figure shows that an annulus of modes grows out of the linear regime. Almost immediately, the annulus collapses to a thin ring showing that the competition between modes along the same radial vector is decided very quickly. On a slower time scale, the modes on the ring compete and eventually one of them wins out leading to a stable travelling wave solution. This travelling wave solution looks flat in modulus since it is represented by an amplitude multiplying e^{ik_cx}.

It appears that, for these parameter values and boundary conditions anyway, the travelling waves are a stable solution to the complex Lorenz equations. The direction of the travelling waves eventually selected depends critically on the initial conditions in the simulation and is decided by a complicated nonlinear competition of the active modes.

Is a travelling wave the only pattern which can be found in the system? Figure 3.11 shows the asymptotic state of another simulation with the same parameters as figure 3.10 but closer to threshold and for a box of half the size.

The figure shows that a rhomboidal pattern can be excited and is stable. The amplitude equations we have derived already only consider two active modes whereas here there are four. It is possible to derive amplitude equations describing the interaction of four modes on the critical circle in an arrangement shown in figure 3.12.

---

[2] *This is a convention we will use for the rest of this thesis.*

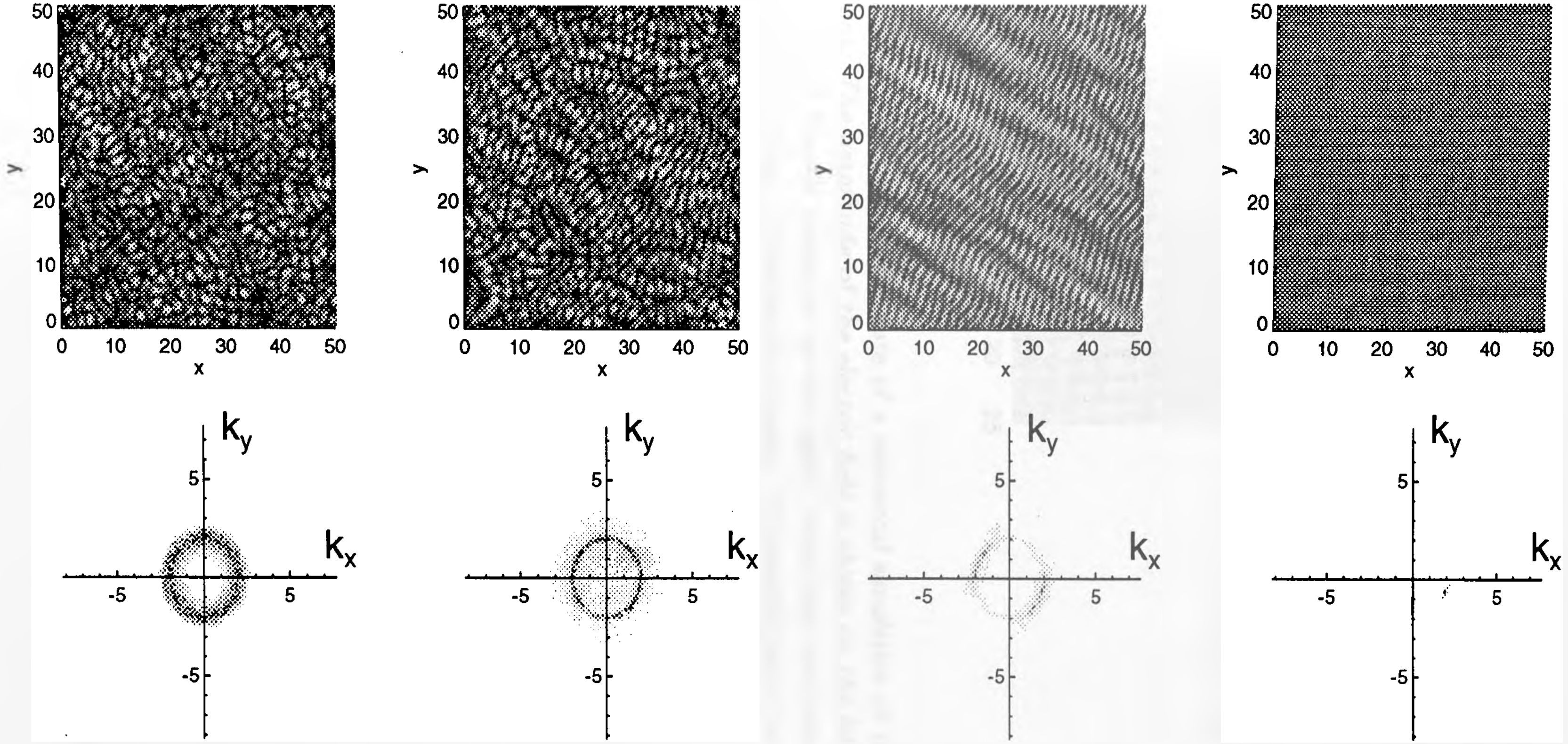

Figure 3.10: The results of a two transverse dimension numerical simulation of the complex Lorenz equations. The top row shows the amplitude of the electric field and the bottom row shows the modulus of the spatial Fourier transform. Parameters are $a = 1$, $b = 1$, $\Delta = 4$, $\sigma = 1$, $r = 2$.

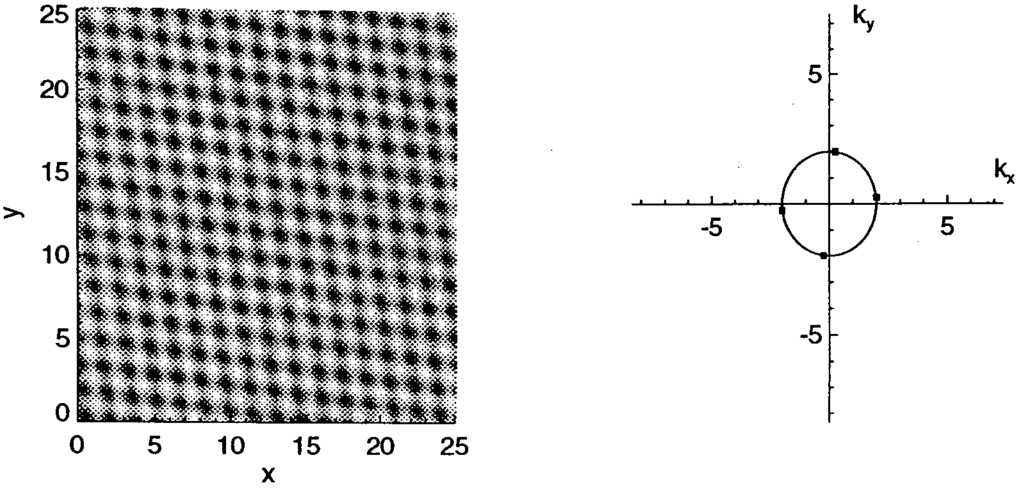

Figure 3.11: The asymptotic state of a numerical simulation of the complex Lorenz equations. The amplitude of the electric field is shown on the left and the modulus of the spatial Fourier transform on the right. Note that the pattern consists of four wavevectors forming a rhombus in k-space. Parameters are $a = 1$, $b = 1$, $\Delta = 4$, $\sigma = 1$, $r = 1.5$.

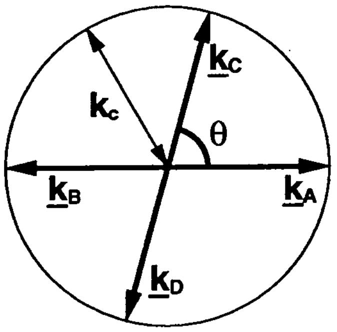

Figure 3.12: The four modes in the amplitude equation calculation.

3.7 Four mode amplitude equations

The derivation of the four mode amplitude equations follows, very closely, the prescription used before for the two mode case. We will use the same notation here but, to simplify the calculation, we'll omit the spatial variation of the amplitudes of the active modes – we'd be able to put them back in later anyway by analogy with the Newell-Whitehead-Segel equations.

By comparison with equation (3.18) we choose a first order solution of the form

$$\mathbf{v}_0 = \begin{pmatrix} 1 \\ 1 \\ 0 \end{pmatrix} \left[\mathcal{A}(T_1,T_2)e^{i\mathbf{k}_A\cdot\mathbf{r}} + \mathcal{B}(T_1,T_2)e^{i\mathbf{k}_B\cdot\mathbf{r}} + \mathcal{C}(T_1,T_2)e^{i\mathbf{k}_C\cdot\mathbf{r}} + \mathcal{D}(T_1,T_2)e^{i\mathbf{k}_D\cdot\mathbf{r}}\right] e^{-i\Omega T_0}$$

where $\Omega = \Delta$, and the vectors $\mathbf{k}_i$ are defined in figure 3.12 and by the relations

$$|\mathbf{k}_A| = |\mathbf{k}_B| = |\mathbf{k}_C| = |\mathbf{k}_D| = k_c,$$
$$\mathbf{k}_A.\mathbf{k}_B = \mathbf{k}_C.\mathbf{k}_D = -k_c^2,$$
$$\frac{\mathbf{k}_A.\mathbf{k}_C}{k_c^2} = \frac{\mathbf{k}_B.\mathbf{k}_D}{k_c^2} = \cos\theta.$$

Just as for the two mode case, the amplitudes must vary on long time scales.

The solvability conditions at second order are

$$\frac{\partial\mathcal{A}}{\partial T_1} = \frac{\partial\mathcal{B}}{\partial T_1} = \frac{\partial\mathcal{C}}{\partial T_1} = \frac{\partial\mathcal{D}}{\partial T_1} = 0$$

and the second order solution is

$$\mathbf{v}_1 = \begin{pmatrix} 0 \\ 0 \\ 1/b \end{pmatrix} \left|\mathcal{A}e^{i\mathbf{k}_A\cdot\mathbf{r}} + \mathcal{B}e^{i\mathbf{k}_B\cdot\mathbf{r}} + \mathcal{C}e^{i\mathbf{k}_C\cdot\mathbf{r}} + \mathcal{D}e^{i\mathbf{k}_D\cdot\mathbf{r}}\right|^2.$$

The nonlinear term at third order contains $e_0 n_1$ and so, for the third order solvability condition, we require to find the components of this which are resonant with one of the wavevectors $\mathbf{k}_i$, where $i \in \{A, B, C, D\}$ Using

$$e_0 n_1 = \left|\mathcal{A}e^{i\mathbf{k}_A\cdot\mathbf{r}} + \mathcal{B}e^{i\mathbf{k}_B\cdot\mathbf{r}} + \mathcal{C}e^{i\mathbf{k}_C\cdot\mathbf{r}} + \mathcal{D}e^{i\mathbf{k}_D\cdot\mathbf{r}}\right|^2 \left[\mathcal{A}e^{i\mathbf{k}_A\cdot\mathbf{r}} + \mathcal{B}e^{i\mathbf{k}_B\cdot\mathbf{r}} + \mathcal{C}e^{i\mathbf{k}_C\cdot\mathbf{r}} + \mathcal{D}e^{i\mathbf{k}_D\cdot\mathbf{r}}\right]/b$$

and with reference to figure 3.12, the nonlinear terms relevant in the solvability condition at third order are ones of the form

$$\begin{array}{rl}
\mathcal{A}\mathcal{A}^*\mathcal{A} & \leftrightarrows\longrightarrow \\
\mathcal{B}\mathcal{B}^*\mathcal{B} & \rightleftarrows\longleftarrow \\
\mathcal{C}\mathcal{C}^*\mathcal{C} & \swarrow\nearrow\nearrow \\
\mathcal{D}\mathcal{D}^*\mathcal{D} & \nearrow\swarrow\swarrow \\
\mathcal{C}\mathcal{D}\mathcal{B}^* & \nearrow\swarrow\longrightarrow \\
\mathcal{C}\mathcal{D}\mathcal{A}^* & \nearrow\swarrow\longleftarrow \\
\mathcal{A}\mathcal{B}\mathcal{D}^* & \rightleftarrows\nearrow \\
\mathcal{A}\mathcal{B}\mathcal{C}^* & \rightleftarrows\swarrow .
\end{array}$$

The amplitude equations come from the solvability condition at third order

$$\begin{aligned}
(\sigma+1)\frac{\partial A}{\partial t} &= \sigma(r-1)A - \frac{\sigma}{b}\left[(|A|^2 + 2|B|^2 + 2|C|^2 + 2|D|^2)A + 2CDB^*\right], \\
(\sigma+1)\frac{\partial B}{\partial t} &= \sigma(r-1)B - \frac{\sigma}{b}\left[(|B|^2 + 2|A|^2 + 2|C|^2 + 2|D|^2)B + 2CDA^*\right], \\
(\sigma+1)\frac{\partial C}{\partial t} &= \sigma(r-1)C - \frac{\sigma}{b}\left[(|C|^2 + 2|A|^2 + 2|B|^2 + 2|D|^2)C + 2ABD^*\right], \\
(\sigma+1)\frac{\partial D}{\partial t} &= \sigma(r-1)D - \frac{\sigma}{b}\left[(|D|^2 + 2|A|^2 + 2|B|^2 + 2|C|^2)D + 2ABC^*\right].
\end{aligned}$$

It is interesting to note that these amplitude equations contain no dependence on the angle between the active modes, $\mathbf{k}_A$ and $\mathbf{k}_B$ (remember that the other two modes are parallel to these but opposite in direction). Terms involving this angle only enter the amplitude equations at fifth order! To third order anyway, the angle is unimportant and rhomboids are just as favoured as squares as any other set of rhomboids. Now, in a similar way as we did for the two mode amplitude equations[31, 32, 33], we find the stationary states of this set of coupled amplitude equations,

1. $A = B = C = D = 0,$
2. $A = \sqrt{b(r-1)}; B = C = D = 0,$
3. $A = B = \sqrt{b(r-1)/3}; C = D = 0,$
4. $A = B = C = \sqrt{b(r-1)/5}; D = 0,$
5. $A = B = C = -D = \sqrt{b(r-1)/5},$
6. $A = B = C = \sqrt{b(r-1)/3}; D = -\sqrt{2b(r-1)/3},$
7. $A = B = C = D = \sqrt{b(r-1)/9}.$

We note that the equations have the symmetry that if the set $\{A, B, C, D\}$ is a solution then so is the set $\left\{Ae^{i\phi_A}, Be^{i\phi_B}, Ce^{i\phi_C}, De^{i\phi_D}\right\}$, so long as the phases obey the relation $(\phi_A + \phi_B) - (\phi_C + \phi_D) = 0$. Another symmetry implies that cyclic permutations of the amplitudes $\{A, B, C, D\}$ in these solutions yield further solutions. For example, there exist travelling wave solutions with each of the amplitudes nonzero in turn and the others zero.

We should now consider the stability of these stationary states by performing linear stability analysis. It turns out that only the travelling wave solutions – 2. – and the rhomboids solutions – 5. – are stable. Let's concentrate now on this solution – 5. – and see what field distribution it gives. For this solution[34], the electric field in the laser is given by

$$e \propto \left[e^{i\mathbf{k}_A\cdot\mathbf{r}} + e^{i\mathbf{k}_B\cdot\mathbf{r}} + e^{i\mathbf{k}_C\cdot\mathbf{r}} - e^{i\mathbf{k}_D\cdot\mathbf{r}}\right] e^{-i\Delta t}.$$

The modulus of this complex expression is

$$\cos^2 \mathbf{k}_A.\mathbf{r} + \sin^2 \mathbf{k}_C.\mathbf{r}$$

and its real part is given by

$$\cos \mathbf{k}_A.\mathbf{r} \cos \Delta t + \sin \mathbf{k}_C.\mathbf{r} \sin \Delta t.$$

The modulus – also the intensity – is a rhomboidal arrangement of bright and dark spots and the real part – indicative of the phase – gives sets of stripes, alternating in time, along the $\mathbf{k}_A$ and then the $\mathbf{k}_C$ directions.

Is this what we have found in the numerical simulation when we observed the rhomboids? Let's go back and re-analyse the data looking, in the real part, for the characteristic flipping between stripes of different orientations. Figure 3.13 shows snapshots in time of the real part of the electric field. The flipping between stripes is very evident.

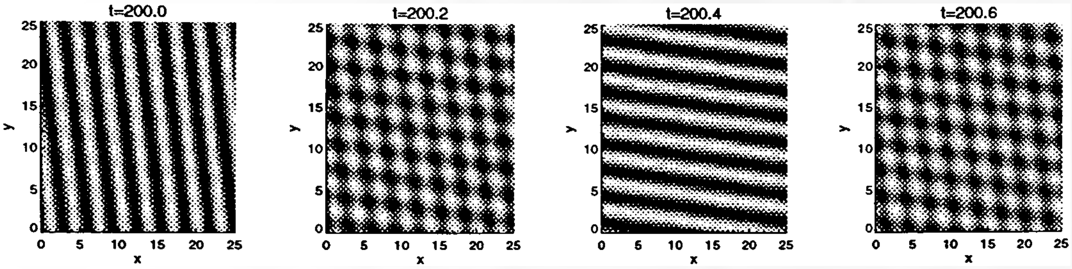

Figure 3.13: The real part of the electric field as a function of the transverse coordinates plotted at the four values of the time shown. The real part shows sets of stripes (or rolls) at an angle whose amplitudes vary sinusoidally in time, always being π out of phase.

3.8 Pattern selection

We have shown that numerical simulations of the complex Lorenz equations can lead to two main types of patterns, travelling waves and rhomboids. Is it possible to assess which of these patterns would be selected when the laser is switched on? It has been shown in other pattern forming systems that deriving a *Lyaponov function* for the system of amplitude equations can give useful information in this respect. Let's consider deriving such a function to represent the four mode amplitude equations. We write the equations in the form

$$\frac{\partial A}{\partial t} = -\frac{\partial F}{\partial A^*},$$

$$\frac{\partial B}{\partial t} = -\frac{\partial F}{\partial B^*},$$
$$\frac{\partial C}{\partial t} = -\frac{\partial F}{\partial C^*},$$
$$\frac{\partial D}{\partial t} = -\frac{\partial F}{\partial D^*},$$

where, by inspection, we see that the function

$$\begin{aligned} F &= \frac{-\sigma(r-1)}{\sigma+1}\left(|A|^2+|B|^2+|C|^2+|D|^2\right)+ \\ & \frac{\sigma}{b(\sigma+1)}\left(\frac{1}{2}(|A|^4+|B|^4+|C|^4+|D|^4)+2|A|^2|B|^2+2|A|^2|C|^2+\right. \\ & \left. 2|A|^2|D|^2+2|B|^2|C|^2+2|B|^2|D|^2+2|C|^2|D|^2+2CDB^*A^*+2ABC^*D^*\right). \end{aligned}$$

The function, F, takes the form of a potential in that stationary solutions of the amplitude equations correspond to points of zero gradient of F. The value of F at these points gives, in some sense, the desirability of the pattern. If a pattern corresponds to a global minimum of the Lyaponov function then it is in some way preferred. Let's compute the value of F for the stationary solutions numbered above as 2. (TW) and 5. (RH),

$$F_{TW} = -\frac{1}{2}\frac{\sigma b}{\sigma+1}(r-1)^2$$
$$F_{RH} = -\frac{2}{5}\frac{\sigma b}{\sigma+1}(r-1)^2.$$

As also shown in figure 3.14, the value of F for travelling waves is indeed smaller than for rhomboids and so we might expect travelling waves to be preferred.

This method is a little woolly and to characterise properly the selection of the pattern we would have to characterise the basins of attraction for the two solutions in an infinite dimensional space of initial conditions. This is beyond the scope of this thesis – and my understanding – but one easier way to study the basins of attraction is to use a physical argument. We can only realistically hope to study the problem in some finite dimensional space and so we choose to restrict ourselves to the four dimensional space represented by the modal amplitudes (A, B, C, D). We hope that these are the

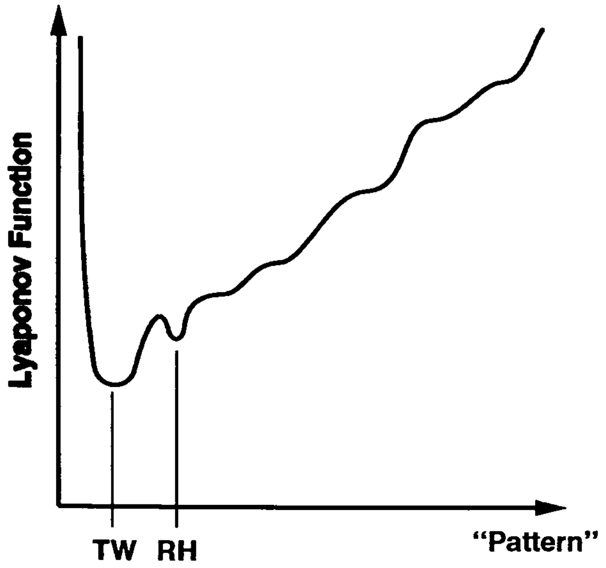

Figure 3.14: A diagrammatic representation of the Lyaponov function, F, based on the four mode amplitude equations. Stationary points of F correspond to stationary states of the amplitude equations with minima being stable. Travelling waves give a global minimum of F and rhomboids give a local minimum.

only important wavevectors on the critical circle and we can hope that all wavevectors not on the critical circle will be damped and will play no role in the dynamics. What's more, we'd like to see which pattern is selected when the laser is first switched on. This means that the initial conditions we need to consider all lie near the origin of this four dimensional space.

To characterise which final pattern is selected for these initial conditions we performed a large number of numerical simulations – in the order of 100000 – of the four mode amplitude equations with random initial conditions close to zero. For each initial condition we kept a note of what the asymptotic state of the system was. The results of this procedure show that the travelling wave solution is chosen about (3.35 ± 0.05) times more often than the rhomboids. This, in some way, backs up the results from the Lyaponov function analysis.

3.9 Stability of Patterns

We have shown that numerical simulations of the complex Lorenz equations can lead to two main types of patterns, travelling waves and rhomboids. By deriving amplitude equations, we have been able to infer their presence, to deduce something about their stability, and say something about how 'preferred' each solution is. The stability analyses we have performed are based on the space independent amplitude equations and so only consider perturbations along the direction of the transverse wavevectors considered in those equations – that is to say that only perturbations to the modal amplitudes are considered.

We can do slightly better than this if we consider instead the equations with the slow spatial variations of the amplitudes included. This allows us to test the stability to perturbations at wavenumbers close to k_c for values of the pump close to threshold – the main assumptions used in the derivation of the amplitude equations.

Another way to do better is to derive what is known as a *phase equation* for the system. This is a technique pioneered by Cross and Newell[35] and relies on the fact that the system of equations have a phase invariance. The variable considered to vary slowly in space and time is then this phase. The analysis of the equation derived in this way, because the travelling wave solutions are exact, leads to a stability analysis valid far from threshold, but still only to perturbations at nearby wavenumbers.

These techniques based on the amplitude equations and the phase equation have been reported by Lega *et al.*[36].

In this section, we discuss the 'best' method of stability analysis[37]. Any time we have an exact solution to a set of equations we can analyse its stability using the standard techniques of linear stability analysis. The drawback of the approach is that, for the travelling waves, the 5×5 matrices whose eigenvalues we require to find are not in a form suitable for direct analysis and so the technique is inevitably numerical.

3.9.1 Full stability analysis

The complex Lorenz equations have the exact travelling wave solutions already given in section 3.3. For clarity we rewrite the solution here,

$$\begin{aligned} e_0 &= A\exp(i\mathbf{k}_0.\mathbf{r} - i\Omega t), \\ p_0 &= \Lambda e_0, \\ n_0 &= r - |\Lambda|^2, \end{aligned}$$

with

$$\begin{aligned} \Lambda &= 1 - i(\Delta - \Omega), \\ \Omega &= \frac{\sigma\Delta + ak_0^2}{\sigma + 1}, \\ |A|^2 &= bn_0. \end{aligned}$$

We can now examine the stability of a travelling wave solution of any wavevector $\mathbf{k}_0$ by considering perturbations E, P and N to the field, polarisation and population inversion respectively. If we insert the expressions $e = e_0(1 + E)$, $p = p_0(1 + P)$, $n = n_0(1 + N)$, into the Lorenz equations and substitute the travelling wave solution given for e_0, p_0 and n_0 then we obtain the equations for the perturbations

$$\begin{aligned} \dot{E} &= ia\nabla^2 E - 2a\mathbf{k}_0.(\nabla E) + \sigma\Lambda(P - E), \\ \dot{P} &= \Lambda^*(E - P) - \frac{n_0}{\Lambda}N, \\ \dot{N} &= -bN + \frac{b}{2}\left[\Lambda(E^* + P) + \Lambda^*(E + P^*)\right]. \end{aligned}$$

We now assume a generic form for the perturbations, namely an amplitude multiplying a particular transverse wavevector. The amplitude of the perturbation is considered small, which has allowed us to linearise the equations above and now find solutions which vary only exponentially in time,

$$\begin{aligned} E &= E_+ \exp(\lambda t + i\mathbf{k}.\mathbf{r}) + E_-^* \exp(\lambda^* t - i\mathbf{k}.\mathbf{r}), \\ P &= P_+ \exp(\lambda t + i\mathbf{k}.\mathbf{r}) + P_-^* \exp(\lambda^* t - i\mathbf{k}.\mathbf{r}), \end{aligned}$$

$$N \;=\; N_+ \exp\left(\lambda t + i\mathbf{k}.\mathbf{r}\right) + N_+^* \exp\left(\lambda^* t - i\mathbf{k}.\mathbf{r}\right).$$

Note that the wavevector $\mathbf{k}$ is relative to the original $\mathbf{k}_0$. We linearise the equations in terms of the perturbation amplitudes to obtain

$$(\lambda\mathcal{I} + \mathcal{M}) \begin{pmatrix} E_+ \\ E_- \\ P_+ \\ P_- \\ N_+ \end{pmatrix} = \underline{0}. \tag{3.26}$$

where

$$\mathcal{M} = \begin{pmatrix} ia\mathbf{k}^2 + 2ia\mathbf{k}_0.\mathbf{k} + \sigma\Lambda & 0 & -\sigma\Lambda & 0 & 0 \\ 0 & -ia\mathbf{k}^2 + 2ia\mathbf{k}_0.\mathbf{k} + \sigma\Lambda^* & 0 & -\sigma\Lambda^* & 0 \\ -\Lambda^* & 0 & \Lambda^* & 0 & n_0/\Lambda \\ 0 & -\Lambda & 0 & \Lambda & n_0/\Lambda^* \\ -b\Lambda^*/2 & -b\Lambda/2 & -b\Lambda/2 & -b\Lambda^*/2 & b \end{pmatrix}.$$

Non-trivial solutions of the matrix equation (3.26) are obtained when the determinant $det(\lambda\mathcal{I}+\mathcal{M}) = 0$. This defines the eigenvalues, λ, of the matrix $\mathcal{M}$. Since the matrix $\mathcal{M}$ is complex and of size 5×5 there are, in general, five complex eigenvalues. These eigenvalues are complicated functions of the system parameters, a, b, σ, Δ, r and also of the wavevectors of the travelling wave whose stability we are testing, $\mathbf{k}_0$, and of the perturbing wave, $\mathbf{k}$. Note that the eigenvalues depend on the angle between the vectors $\mathbf{k}_0$ and $\mathbf{k}$ through the terms which involve their scalar product. For the stability analysis we choose an angle ϕ at which the perturbations will be applied and, in the matrix $\mathcal{M}$ replace the terms $\mathbf{k}_0.\mathbf{k}$ with $k_0 k \cos\phi$. By choosing the system parameters, and values for k_0 and ϕ we can compute the five eigenvalues $\lambda(k)$. If any of the five values of $Re(\lambda(k)) > 0$, perturbations with wavevector k will grow exponentially ; if all five $Re(\lambda(k)) < 0$ the perturbations at that wavevector will decay exponentially. In the following we will be interested in the largest of the five real parts since if it is positive the system is unstable – if it is negative then all the eigenvalues are negative and the system is stable.

Figures 3.15 and 3.16 show the stability of a travelling wave of wavevector k_0 for a given value of the pump parameter, r. The shaded area is the *Busse balloon*[38] – where travelling waves are linearly stable to perturbations. In figure 3.15 the perturbations are assumed to be along the travelling wave's direction ($\phi = 0$) and in figure 3.16 they are assumed to be perpendicular to that direction ($\phi = \pi/2$). For arbitrary angles the Busse balloon always encompasses the intersection of the two balloons shown and so, for a travelling wave to be entirely stable it must lie within the shaded area in both of these diagrams.

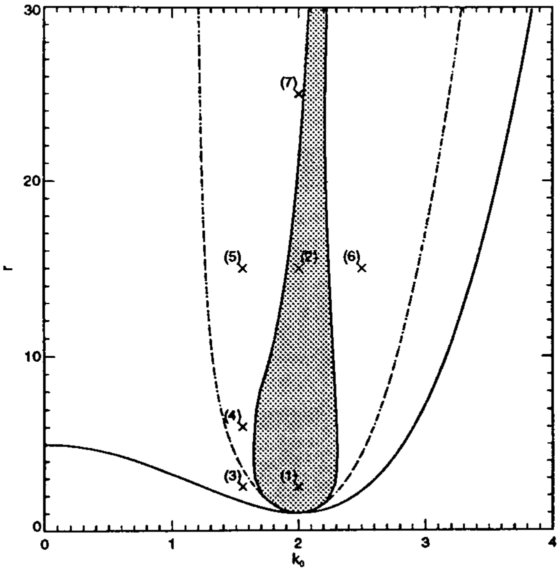

Figure 3.15: The stability of a travelling wave with wavevector k_0 at a pump value r to perturbations at any wavevector parallel to the wave's direction ($\phi = 0$). Parameters are $a = 1$, $b = 1$, $\Delta = 4$, $\sigma = 1$, $\phi = 0$

For the parameters at the position of each cross in the stability diagrams we plot the maximum real part of the eigenvalues of the stability matrix, $\mathcal{M}$, as a function of perturbing wavenumber, k. The results are shown in figure 3.17. In figure 3.18, we show the wavevectors in the 2D transverse plane which are unstable. The grey bands are the unstable wavevectors. A horizontal slice through the centre of one of these diagrams gives the perturbation wavevectors at an angle $\phi = 0$ and a vertical slice

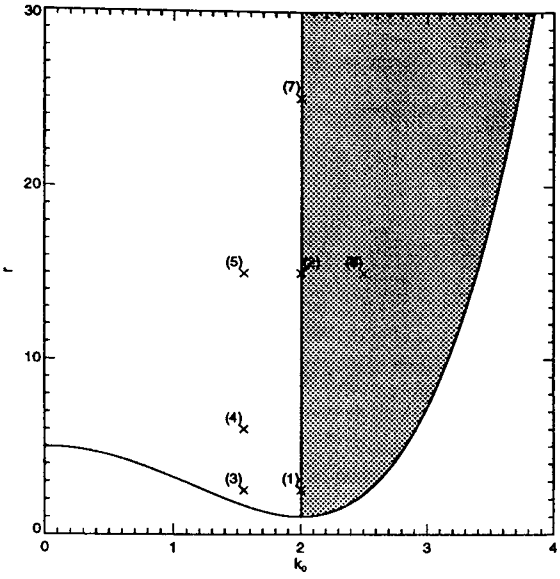

Figure 3.16: The stability of a travelling wave with wavevector k_0 at a pump value r to perturbations at any wavevector perpendicular to the wave's direction ($\phi = \pi/2$). Parameters are $a = 1$, $b = 1$, $\Delta = 4$, $\sigma = 1$, $\phi = \pi/2$

through the centre is for perturbations at an angle $\phi = \pi/2$.

There are some generic features of these spectra which are worthy of comment. Provided we test the stability of a travelling wave which is above threshold the largest eigenvalue is forced to be zero for $k = 0$. The spectrum is also symmetric around this point. The reason for this symmetry is apparent from the form of the matrix $\mathcal{M}(k)$. Consider the transformation $\mathbf{k} \longrightarrow -\mathbf{k}$; by re-ordering the matrix $\mathcal{M}(-k)$ it is possible to show that

$$\det(\lambda^* \mathcal{I} + \mathcal{M}(-k)) = \det(\lambda \mathcal{I} + \mathcal{M}(k)).$$

The transformation $\mathbf{k} \longrightarrow -\mathbf{k}$ has the effect of conjugating the matrix's eigenvalues. This has no affect on the stability (real parts) and reverses the sign of the frequencies associated with each instability (imaginary parts).

We see three distinct forms of instability, namely *Eckhaus*[39], *amplitude*, and *zig-zag*, shown diagramatically in figure 3.19. The Eckhaus instability is to wavevectors along the direction of the travelling wave and is to small wavenumbers. The amplitude

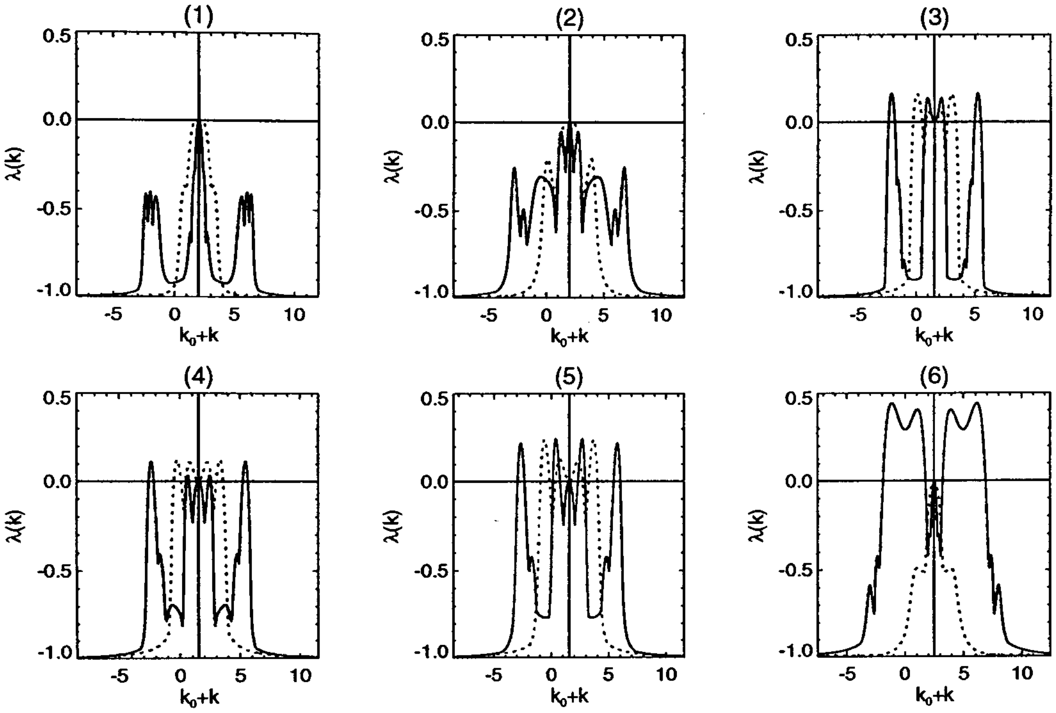

Figure 3.17: Most unstable eigenvalue $\lambda(k)$ *as a function of* $k_0 + k$ *for parameters marked by crosses in the stability diagrams. The full lines are for perturbations at angle* $\phi = 0$ *and the dotted lines for perturbations at angle* $\phi = \pi/2$. *The parameters are* $a = 1$, $b = 1$, $\sigma = 1$, $\Delta = 4$, *(1):* $k_0 = 2$, $r = 2.5$; *(2):* $k_0 = 2$, $r = 15$; *(3):* $k_0 = 1.55$, $r = 2.5$; *(4):* $k_0 = 1.55$, $r = 6$; *(5):* $k_0 = 1.55$, $r = 15$; *(6):* $k_0 = 2.5$, $r = 15$

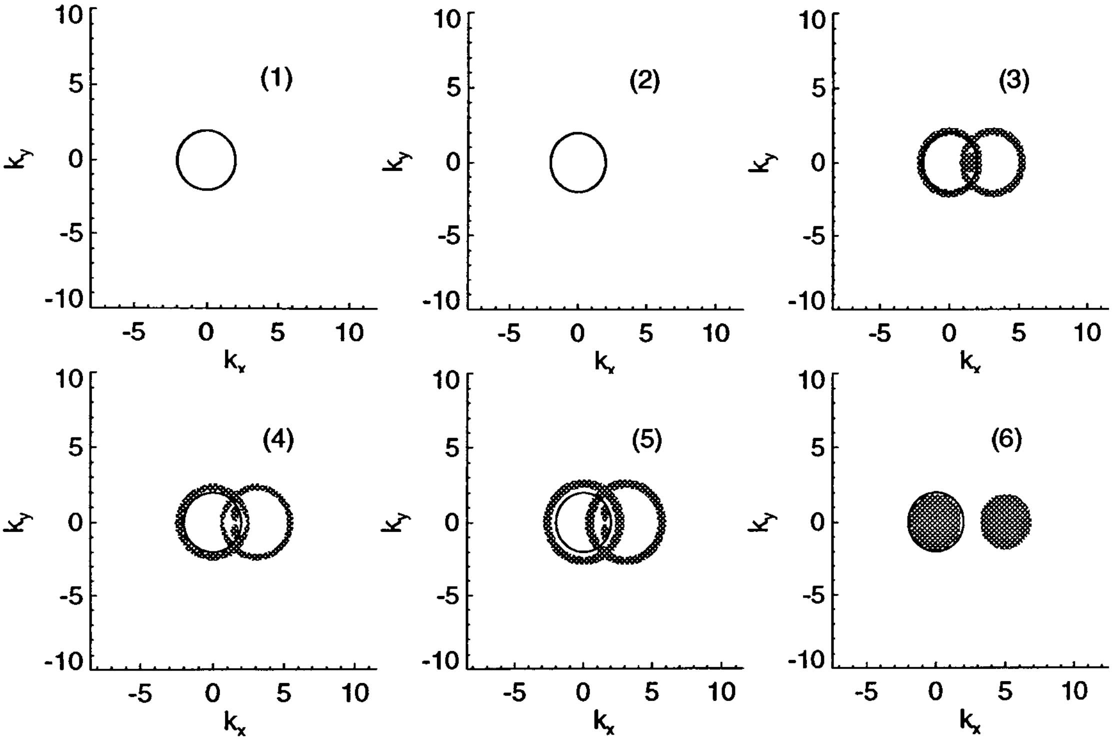

Figure 3.18: The unstable wavevectors in the stability analysis of the travelling waves marked by crosses in the stability diagrams. The shaded areas are wavevectors in the transverse plane which are unstable. Plotted as a full circle is the most unstable band of wavevectors of radius k_c.

instabilities are in the same directions but are to a wavenumber of arbitrary size. The zig-zag instability is to small wavenumbers but at right angles to the direction of the travelling wave.

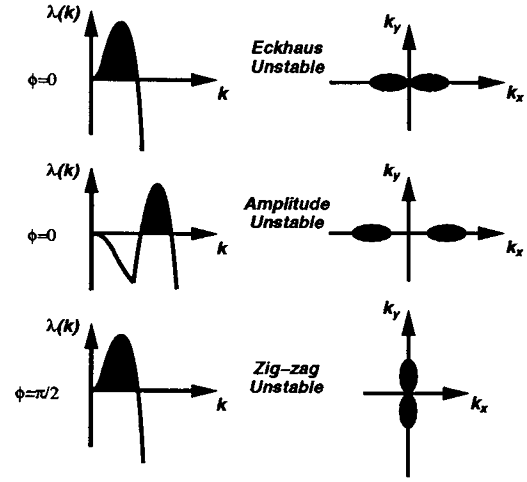

Figure 3.19: A diagrammatic representation of the three types of instability found for travelling waves in the two level laser: Eckhaus, amplitude and zig-zag instabilities.

Before we undertake a numerical simulation of the laser equations to determine the nature of each of these classes of instability, let us pause for a moment to consider the physical mechanisms involved in the instabilities.

In its strive for efficiency the laser always tries to emit in a state which has a transverse wavevector with modulus as close as possible to the most unstable one, k_c. If it is presented with a wavevector not meeting this criterion – roughly speaking that is one not in the Busse balloon – it tries its best to get back into the balloon (back onto the critical circle of radius k_c in k-space). It does this by making the unwanted wavevector unstable, usually to other ones it likes better. These other wavevectors are then seeded and, the laser hopes, will grow to lase efficiently. We can see this very clearly in figure 3.18 in that there is always a band of wavevectors close to the critical circle which go unstable.

By an argument just like this it is easy to see why only wavevectors $k_o < k_c$ are zigzag unstable. Figure 3.20 explains this point. If $k_o < k_c$ then the laser can generate a wavevector, $k_\perp$, perpendicular to k_o which allows it to get back onto the critical circle. If $k_o > k_c$ then no such perpendicular wavevector exists to get back onto the critical circle. In this case, the laser must rely on an instability parallel to the direction of k_o to let it lase nearer to the circle.

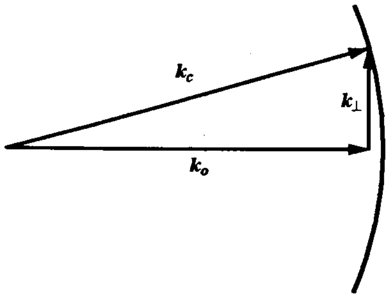

Figure 3.20: A simple explanation of why the zig-zag instability only affects travelling waves with $k_o < k_c$.

Let's now consider numerical simulation of the laser equations to determine exactly what happens to travelling waves unstable in each of the three ways in turn.

3.9.2 Eckhaus Instability

Positions in figure 3.15 which are Eckhaus unstable are, almost always, also amplitude unstable. The features of this instability are considered in the section which deals with the amplitude instability.

3.9.3 Zigzag Instability

Figure 3.21 shows the results of a numerical simulation of the Lorenz equations given an initial condition which is zig-zag unstable. Plotted in the figure is the real part of the electric field, $Re(e)$, and the Fourier transform of e at four points in time. The initial condition is a pure travelling wave – visible as stripes in the real part – plus some additive noise used to seed the instability. After a short time, the stripes start to distort and become bent. This is characteristic of the zig-zag instability. As expected, the Fourier transform shows a broadening in a direction perpendicular to the direction of the travelling wave.

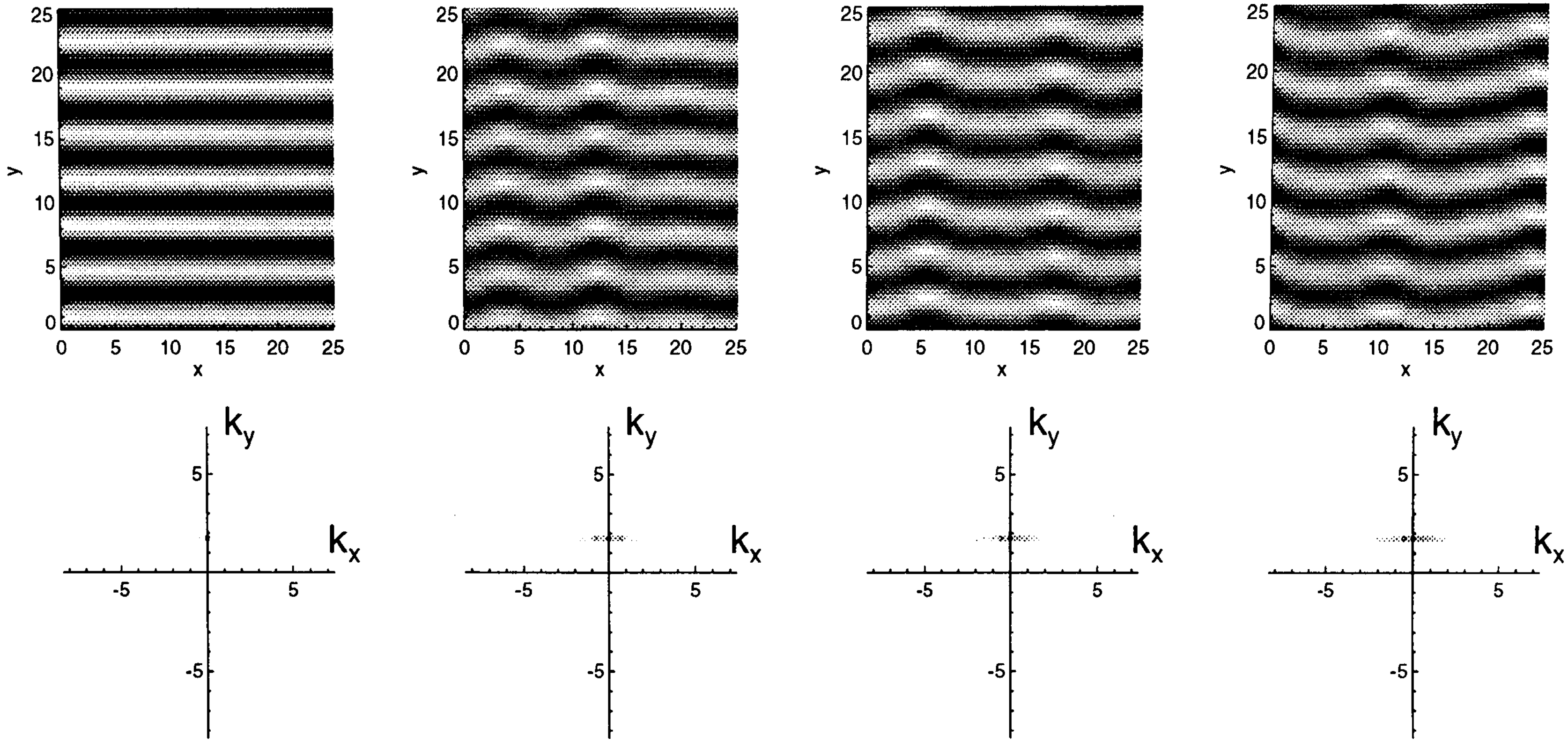

Figure 3.21: A numerical simulation showing the zig-zag instability of a travelling wave. The top row shows the real part of the electric field as a function of the transverse coordinates. The bottom row shows the spatial Fourier transform of the electric field. Images have been produced at times, $t = 0$, $t = 250$, $t = 500$ *and* $t = 1000$.

3.9.4 Amplitude Instability

The amplitude instability can manifest itself in a number of ways. Let's consider first a numerical simulation of the complex Lorenz equations with an initial condition of a travelling wave at position (7) in figure 3.15. This position is both amplitude and zig-zag unstable. The instabilities lead to a redistribution of the energy into other spatial wavevectors. All of these wavevectors can then undergo a complicated nonlinear competition leading to a pattern of large spatio-temporal complexity. Note that the amplitude equations are completely invalid in this case since we are very far from threshold. Figure 3.22 shows the initial condition and asymptotic, but not time independent, state of the simulation.

In contrast to this, position (4) in figure 3.15 is much closer to threshold but, like position (7) is both amplitude and zig-zag unstable. A simulation run for these parameter values and initial conditions gives very different results – see figure 3.23. In this case, the amplitude instability tends to seed a travelling wave lying within the Busse balloon which then starts to dominate the dynamics. The end result is a travelling wave showing only a zig-zag instability.

Look again at the stability diagrams (figures 3.15 and 3.16) and consider the case of positions on the neutral stability curve. At these positions, we are performing the linear stability analysis of a travelling wave with a very small amplitude. Just as in section 3.2 where we performed the stability analysis of the nonlasing solution, we might expect to find instability to wavevectors at $\pm k_c$. This gives us a new way of interpreting the spectra close to the neutral curve. Instead of really being an amplitude instability of a travelling wave, they are the laser trying to seed the spatial frequencies it wants to lase on, namely those on the critical circle of radius k_c.

Simulations close to threshold starting from initial conditions which are so called amplitude unstable, such as position (4), usually evolve towards a travelling wave in the Busse balloon. Far from threshold, such as position (7), the amplitude instability need not seed frequencies which are in the Busse balloon and so the system evolves to a complicated dynamical state. All of this goes to show that linear stability analysis

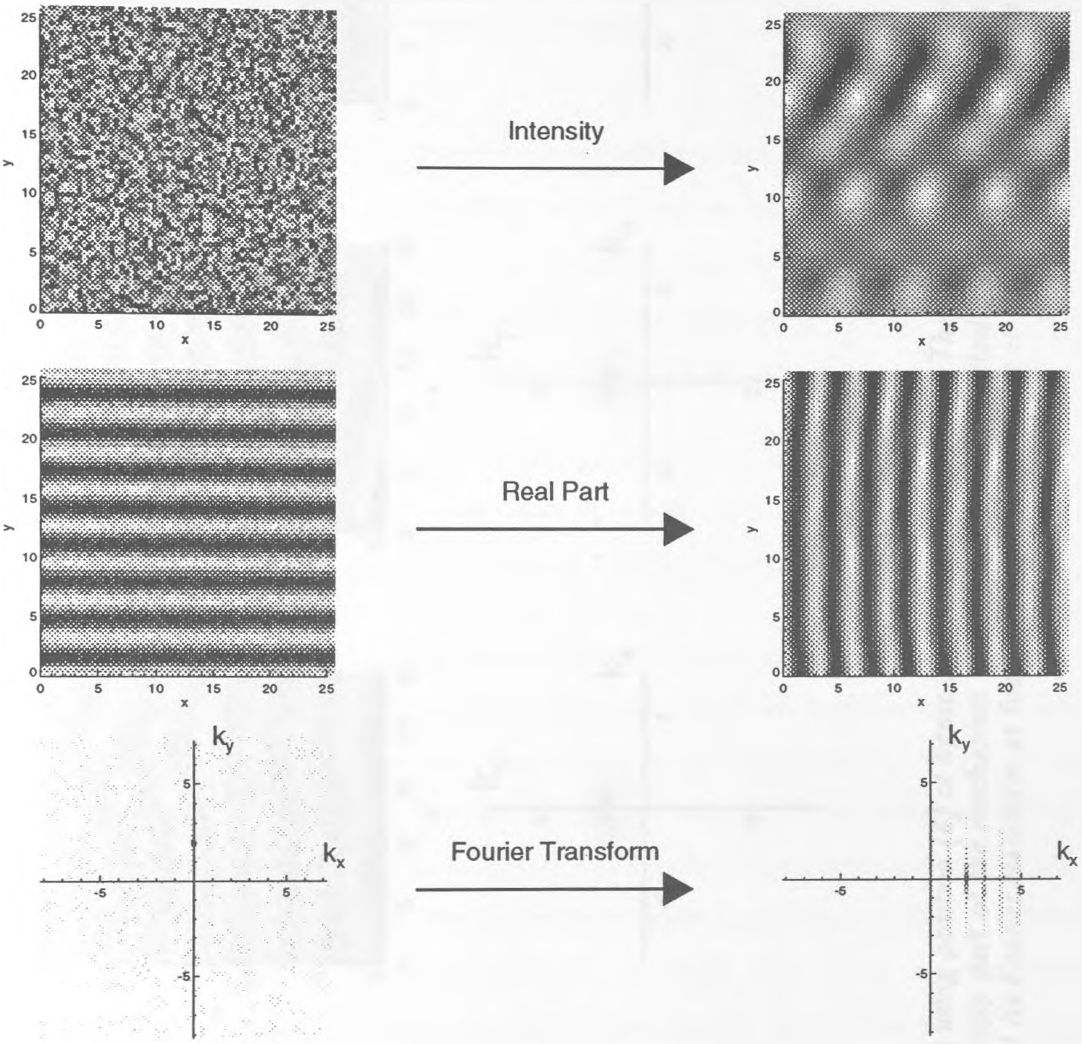

Figure 3.22: The initial condition and asymptotic state of a numerical simulation showing the amplitude instability of a travelling wave at position (7) in figure 3.15. The top row shows the field intensity, the middle row the real part of the field and the bottom row the Fourier spectrum. Parameters are $a = 1$, $b = 1$, $\Delta = 4$, $\sigma = 1$, $r = 25$.

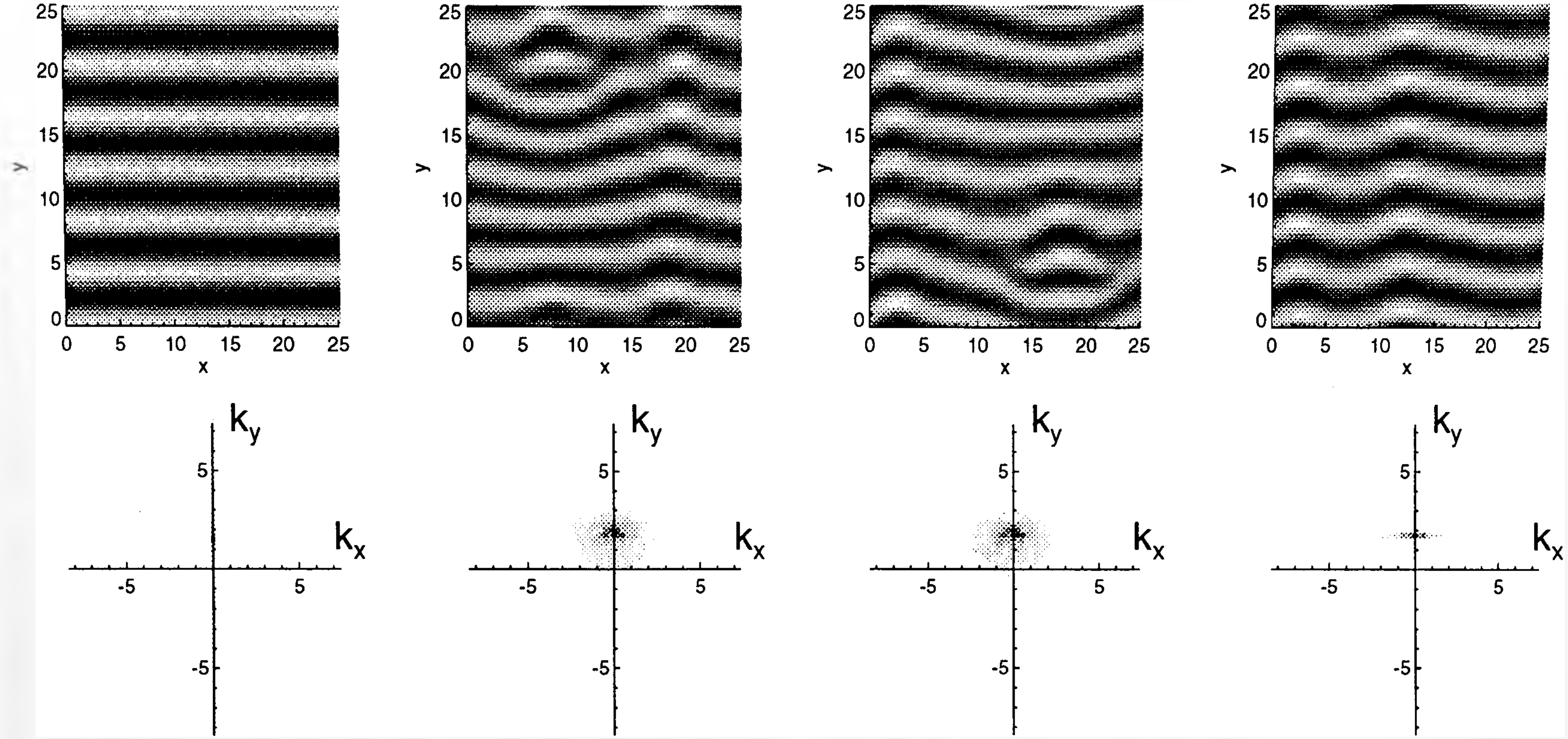

Figure 3.23: A numerical simulation using position (4) of figure 3.15 as the initial point. The amplitude instability has little to do with the final state of the laser and is simply part of the mechanism helping the laser to get itself back into the Busse balloon. Shown are the real part of the electric field and its Fourier transform at four points in time, $t = 0$, $t = 125$, $t = 250$ *and* $t = 600$.

is not really enough to tell the whole story and numerical simulation of the equations is usually one of the only ways of determining the asymptotic state of the system.

3.10 Travelling Wave Defects

In the previous sections we have shown that travelling waves can be selected as the lasing state. The direction of the travelling waves is entirely arbitrary. In the numerics the direction is determined by the noise in the initial condition and in the simulation as it proceeds, the boundary conditions may affect the outcome. In an experiment asymmetries in a cavity may result in certain directions being preferred over others.

If the transverse domain is big enough, then spatially distanced regions do not communicate information about their state and so could, in principle, produce waves travelling in different directions. Let's consider this possibility in 1D.

Figure 3.24 shows the result of a numerical simulation of the Lorenz equations on a very broad periodic domain. The upper row shows the time evolution of the field amplitude and, in the lower row, we have extracted the amplitudes of the forward and backward travelling waves. The grey areas are dominated by waves travelling leftwards, the other areas by waves travelling rightwards. These areas are connected by *defects* of the system[7, 10], shown diagrammatically in figure 3.25. These defects were called *source* and *sink* by Coullet *et al.*[40] when they were studied in the context of coupled Ginzburg-Landau equations with convective terms. The source defect, as its name suggests, is a place from where travelling waves are born and appears as a place where the field intensity passes through zero. The sink defect is a place where they collide and are 'killed'. It appears as a place where there is large modulation of the field intensity. The modulation is due to the interference of two counterpropagating travelling waves. The defects are localised in space because, as we have seen already, the zero solution at the core of the source and the standing waves at the core of the sink are unstable to travelling waves. This is an instance of a common phenomenon in pattern formation. An unstable solution appears at the

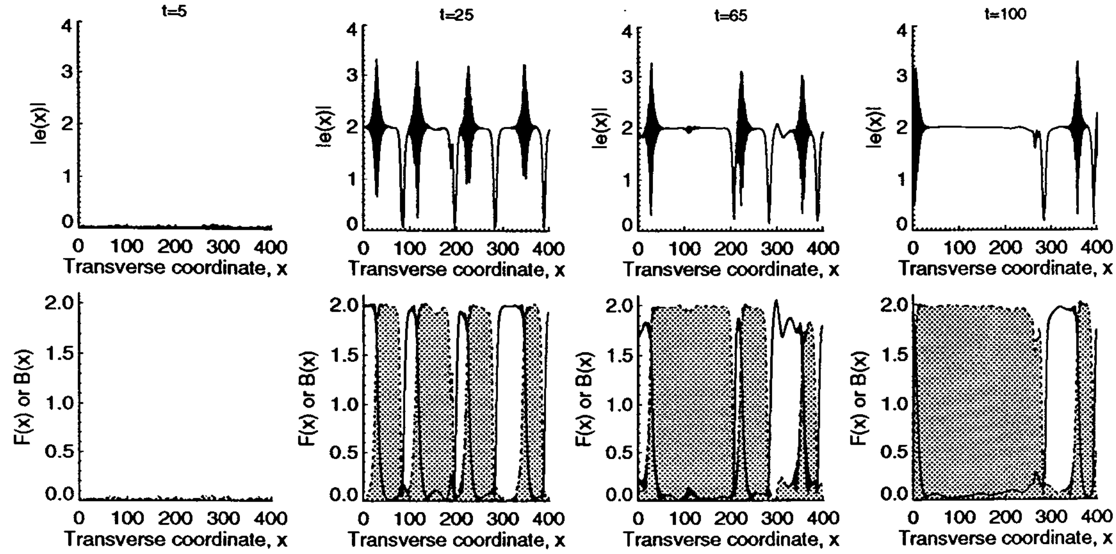

Figure 3.24: A numerical simulation of the complex Lorenz equations in 1D. The output shows regions where waves travel forwards and where they travel backwards (shaded grey). These regions are connected by the source and sink defects. During the time evolution, the defects annihilate simplifying the spatial output.

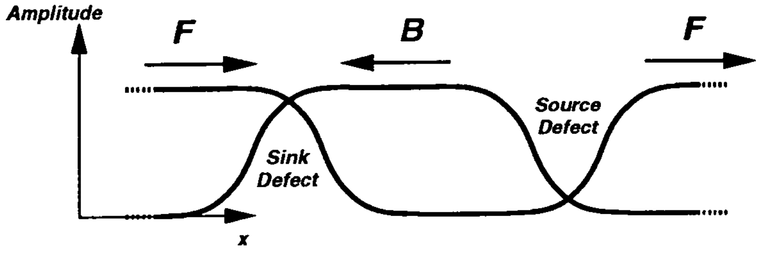

Figure 3.25: A diagrammatic representation of the source and sink defects.

core of a defect[41].

In figure 3.24, as time progresses, the defects feel the others around them and can move slowly, sometimes annihilating with each other, leading to a more ordered transverse output. Similar effects can be seen in 2D simulations but because the defects have two dimensions to move in they usually annihilate much more quickly.

Chapter 4

Effects of Boundaries on Travelling Waves

4.1 Introduction

We have shown in chapter 3 that positively detuned lasers with infinite transverse extent can show travelling waves and rhomboidal patterns. Since not many practical lasers have an infinitely extended transverse plane, at some point we should consider the effects that transverse boundaries have on these patterns. It has been shown in other nonlinear optical systems that such boundary effects may not be trivial[42]. They can greatly alter the range of patterns which can be observed.

A laser cavity typically contains elements which try to confine the laser field close to the optical axis. Elements used frequently are curved cavity mirrors and intracavity apertures. Also, only some finite region of the transverse plane can consist of gain medium and can be fed energy so that it provides gain for the optical field. None of these things have been considered in the study of the travelling waves. The aim of this chapter is to consider the effects that transverse boundaries have on these patterns. We will study three main types of transverse boundary.

Firstly, we will impose the condition that the field be zero at the sides of a given transverse domain. Physically, this corresponds to a laser with perfectly reflecting 'walls'. In 1D the boundaries form a linear domain ; in 2D we can have domains of different shapes – we'll consider a square and a circular domain.

Secondly, we will consider the effects of a finite gain profile on the pattern formation in the system. In just the same way as we did for the gain guided modes in chapter 2 we will make the gain a function of the transverse coordinates. The laser field will be confined to the region where there is gain. This can be shown to be similar to modulating the losses.

Thirdly, we will consider the effects of curved cavity mirrors. We will see that the behaviour in this situation can be fundamentally different to that in the other two cases.

4.2 Reflecting Boundaries

We consider the case of a dielectric waveguide in the appropriate limit so that the laser field, e, obeys the condition $e = 0$ on the boundary [43] ; because they have no driving terms on the boundary, $p(x, y)$ and $n(x, y)$ obey the same condition.

4.2.1 One Transverse Dimension

To get the ball rolling we perform a one transverse dimension numerical simulation of the Lorenz equations with these boundary conditions. A typical asymptotic state of the simulation is shown in figure 4.1. The results show that a localised standing wave appears at one of the boundaries. At the other boundary the field goes to zero without a standing wave. In the centre of the domain there is a backward travelling wave. Remember that a travelling wave consists of only a phase modulation and so appears flat in the output intensity.

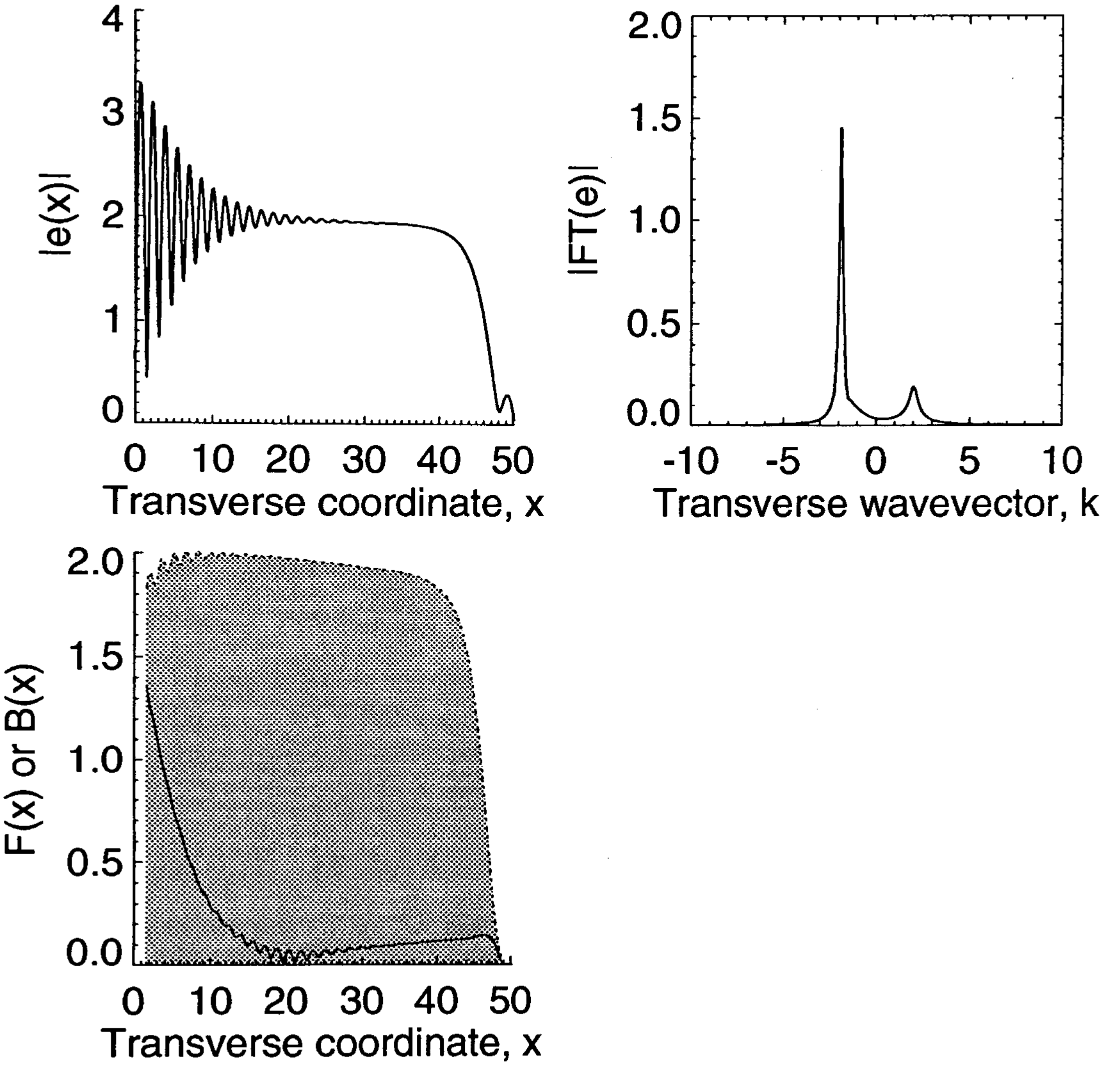

Figure 4.1: Plotted on the left is the modulus of the electric field, $|e|$, as a function of transverse space coordinate, x, for a domain width, $L \approx 50$: $a = 1$, $b = 1$, $\Delta = 4$, $\sigma = 1$, $r = 5$. On the right is the spatial Fourier transform of the pattern showing strong features at $\pm k_c$. In the bottom plot, we have extracted the amplitudes of the forward and backward travelling waves and plotted them as function of the x ; the area under the backward wave amplitude is shaded grey. The backward travelling wave dominates in the centre and a forward travelling wave is generated on reflection at the boundary.

The Fourier transform of the final state is also shown in figure 4.1 and shows strong features at the spatial frequencies corresponding to the forward and backward travelling waves. This gives us some hope that we may be able to explain this asymptotic state in terms of the travelling waves of the infinitely extended system.

To further explain the result, consider, just as in the amplitude equations, the electric field to be a sum of forward and backward travelling waves with amplitudes $F(x)$ and $B(x)$. In figure 4.1 we have extracted these amplitudes from the numerical data and plotted them as a function of the transverse coordinate. The boundary conditions are $e(0) = e(L) = 0$ which are, in terms of the travelling wave amplitudes, $F(x) = -B(x)$ for $x = 0, L$. At the centre of a sufficiently wide transverse domain we expect the system to behave in a similar way to the infinitely extended system, namely that one of the travelling waves will dominate – see figure 4.2. Which one does dominate depends on chance through the the initial conditions in a similar way to that described in section 3.6. In figure 4.1 the backward travelling wave dominates in the centre. As the wave travels backwards it reaches the left hand boundary and reflects, generating a forward travelling wave and so, close to this boundary, we see an area comprising both forward and backward waves. We showed in the previous chapter that standing waves are unstable and so the forward travelling wave is suppressed as it propagates rightwards.

Close to the right hand boundary and in the initial 'switch-on' phase of the laser both forward and backward waves will be generated and the winner will be determined by their nonlinear competition, just as was described in section 3.6. The backward wave is reinforced by the reflection of the forward wave and so dominates, propagating back towards the centre.

This explanation can be clarified somewhat with reference to figure 4.3 which shows the field in figure 4.1 reflected in the left and right boundaries. It is now easy to draw analogies between this and figure 3.24 and so to see the structures at the boundaries as the source and sink defects of the infinitely extended system.

Before going on to discuss the defects further we give a brief indication of what

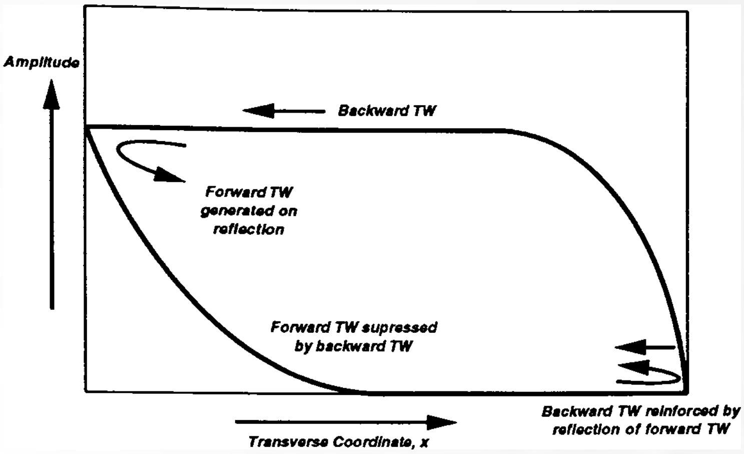

Figure 4.2: A diagrammatic representation of the amplitudes of the forward and backward travelling wave amplitudes as a function of the transverse coordinate, x, and how these amplitudes combine to make the pattern in figure 4.1.

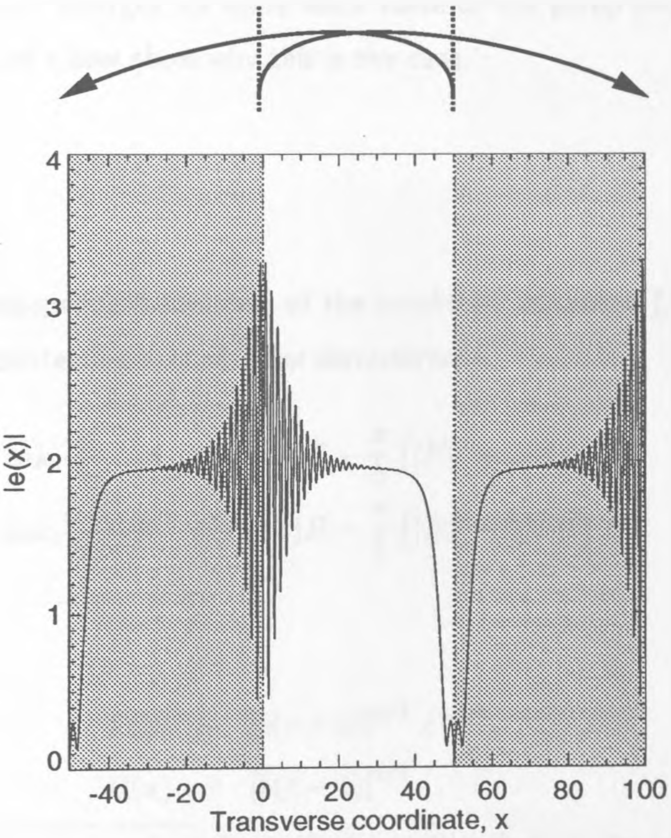

Figure 4.3: The asymptotic state shown in figure 4.1 reflected in the left and right boundaries. The structures at the boundaries reveal themselves as the source and sink defects of the infinitely extended system.

happens in larger aspect ratio simulations. Figure 4.4 shows the results of a simulation with a domain width $L = 400$, eight times that of figure 4.1. This snapshot in time shows a complicated array of source and sink defects which are initially created and then annihilate as part of the dynamics.

Size of the Defects

Since the boundaries confine the transverse domain to a given size we should try to find the transverse extent of the source and sink defects. These defects have been studied by Coullet *et al.*[40] in the context of coupled complex Ginzburg-Landau equations. The source and the sink defect behave very differently. The size of the sink defect diverges as the pump is brought close to threshold, $r \longrightarrow 1$. The source defect's size, however, diverges for some finite value of the pump above threshold, that is as $r \longrightarrow r_c$. Let's now show why this is the case.

Sink Defect

We look for time independent solutions of the amplitude equations (3.22) – (3.23) without the terms containing second order derivatives,[1]

$$\begin{aligned} 2ak_c\frac{\partial F}{\partial x} &= \sigma(r-1)F - \frac{\sigma}{b}\left(|F|^2 + 2|B|^2\right)F \\ -2ak_c\frac{\partial B}{\partial x} &= \sigma(r-1)B - \frac{\sigma}{b}\left(|B|^2 + 2|F|^2\right)B \end{aligned}$$

and substitute

$$\begin{aligned} F(x) &= [b(r-1)]^{1/2}\, e^{-x/l}, \\ B(x) &= [b(r-1)]^{1/2}. \end{aligned} \tag{4.1}$$

---

[1] *The inclusion of other terms from the amplitude equations increases the complexity of the analysis and makes little difference to the end result.*

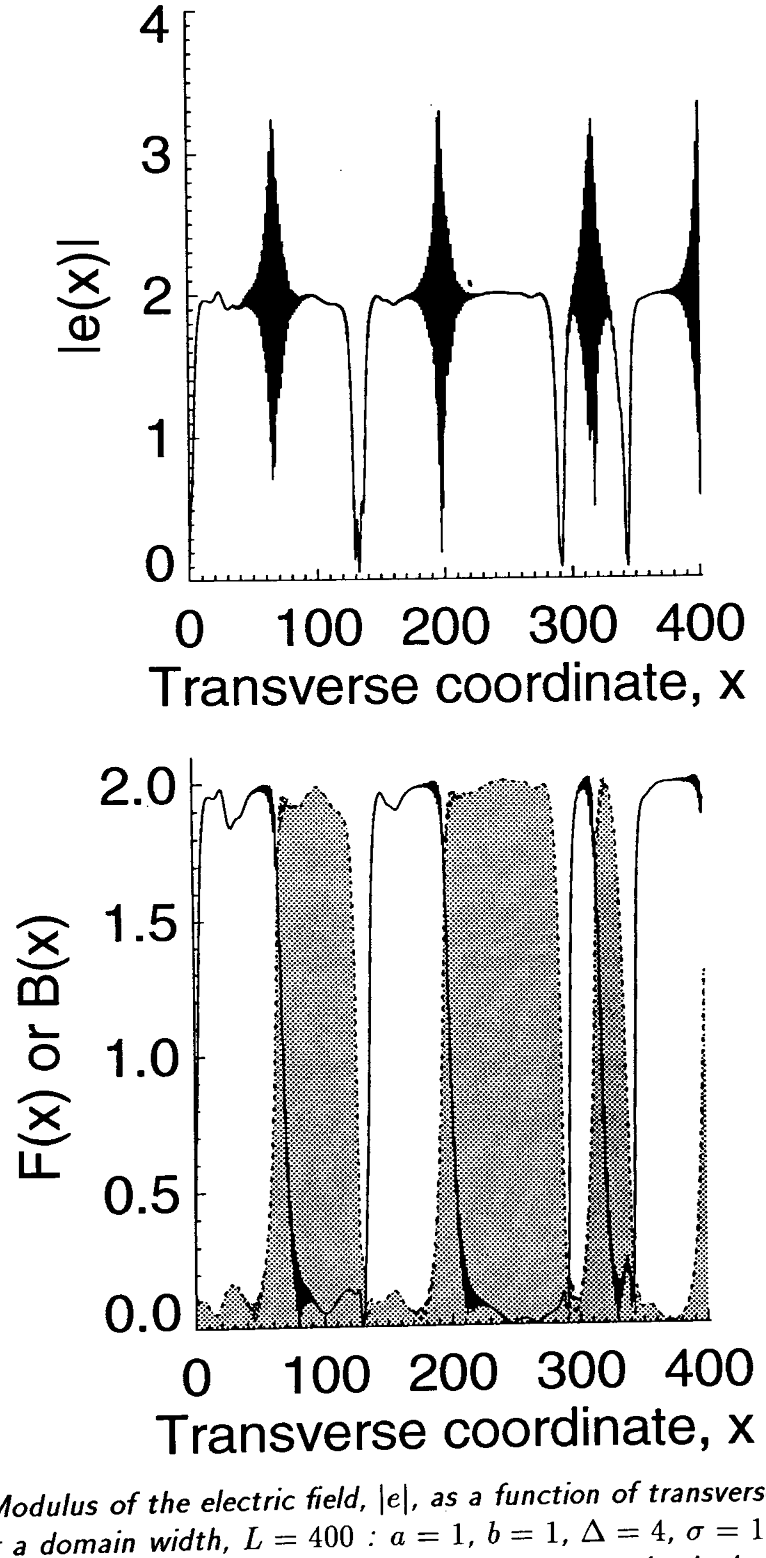

Figure 4.4: Modulus of the electric field, $|e|$*, as a function of transverse space coordinate,* x*, for a domain width,* $L = 400$ *:* $a = 1$*,* $b = 1$*,* $\Delta = 4$*,* $\sigma = 1$*,* $r = 5$*. The areas under the amplitude of the backward wave shaded grey in the lower diagram.*

The linearised equation for F around $F = 0$ now gives an estimate for the size of the sink defect,

$$l \approx \frac{2ak_c}{\sigma(r-1)}.$$

Note that much more complicated methods based on the amplitude equations can be used to estimate the size of the sink, but none give results appreciably better than this. Our criterion for 'better' in this case is a comparison with numerical simulations. Figure 4.5 shows a graph of the sink defect size, l, as a function of the pump parameter, r. For comparison, we performed numerical simulations of the complex Lorenz system, extracted the amplitudes of the forward and backward travelling waves, using a localised Fourier integral method, and found the value of l in (4.1) which gave the best fit to the data. These data points are shown in figure 4.5 as diamonds. The estimates calculated from the amplitude equations do not agree too well quantitatively with the numerics but the qualitative behaviour is correct. The most important point to note is that the size of the sink defect diverges as $r \to 1$.

Source Defect

Consider now the source defect. It is the place where the travelling waves are born from the nonlasing solution and there are two important processes taking place near its core. The laser field is growing and is selecting a transverse wavevector in a very similar way to that discussed in section 3.6. The linear growth term in the amplitude equations is proportional to $(r - 1)$ and so the field grows at a rate proportional to the size of the pump above threshold. We see no standing wave patterns as we did in section 3.6 because, at the core of the defect, oppositely orientated waves soon become spatially separated as they travel away from each other. The second important process taking place is *advection* or the propagation of the travelling waves. We have seen from the nonlinear analysis in section 3.4 and from the exact travelling wave solution given in section 3.3 that their group velocity does not depend on the pump.

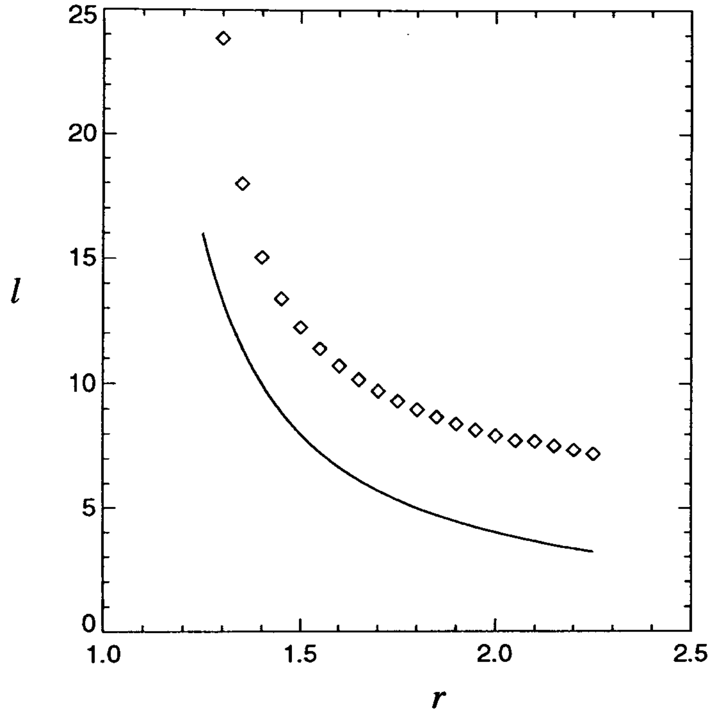

Figure 4.5: The characteristic size, l, of the sink defect extracted from the numerical simulations (diamonds) and computed from the amplitude equations (full line) plotted versus the pump parameter, r. Other parameters are $a = 1$, $b = 1$, $\Delta = 4$, $\sigma = 1$

Under normal circumstances, waves with wavevector k_c are generated at the source, they grow and are transported away at the group velocity. However, if the laser is very close to threshold, the waves are transported away before they have a chance to grow and in this way the size of the source diverges. This is known as a *convective instability*[10, 40] of the source defect. By comparing the coefficients of the amplitude equtaions in reference [40] and those in equations (3.22) – (3.23) it can be shown that the instability manifests itself for values of the pump $r < r_c$ where

$$r_c = 1 + \frac{4a^2k_c^4(\sigma+1)^2}{(\sigma+1)^4 + 16a^2k_c^4\sigma^2}. \tag{4.2}$$

This divergence means, for the laser, that the sink defect will grow in size, switching off the laser as it does so! This leaves the laser in a state very susceptible to noise perturbations and, in fact, any noise in the system will cause the lasing solutions to be reseeded, limiting the size of the source defect. This growth of perturbations from noise is not without side-effects and these appear as the formation of a series of 'blips' which are generated at the source and are advected away with the travelling waves. Such a 'blip' can be seen close to the right hand boundary in figure 4.1. We will discuss these phenomena more fully in section 4.2.3 below.

Transition from TW to SW

Until now, we have considered situations in which the boundaries are 'far apart'. By this we mean that the defects localised at the boundaries do not interact strongly with each other and that there is some region between them where the travelling waves are relatively pure.

If the defects were to be brought 'closer together' then they would interact strongly. In the infinitely extended system we have already seen that such a strong interaction leads to the defects annihilating but, with reflecting boundaries, the defects are 'pinned' on the boundaries and cannot do this. We are now left to define what is meant by 'closer together'. A sensible definition would be to say that if the defects are closer than their transverse size, then they are 'close'. What really matters then is the larger of the two defect sizes. We have already shown that, as the laser is brought very close to threshold, the size of the source defect is fixed by the noise in the system and that the size of the sink defect diverges to infinity. The important size is therefore that of the sink.

Figure 4.6 shows the results of a numerical simulation, close to threshold, in which the size of the sink defect is made comparable to the size of the transverse domain. Indeed, it appears that the sink defect expands to fill the entire domain with standing waves, leaving an output which is symmetrical about its centre.

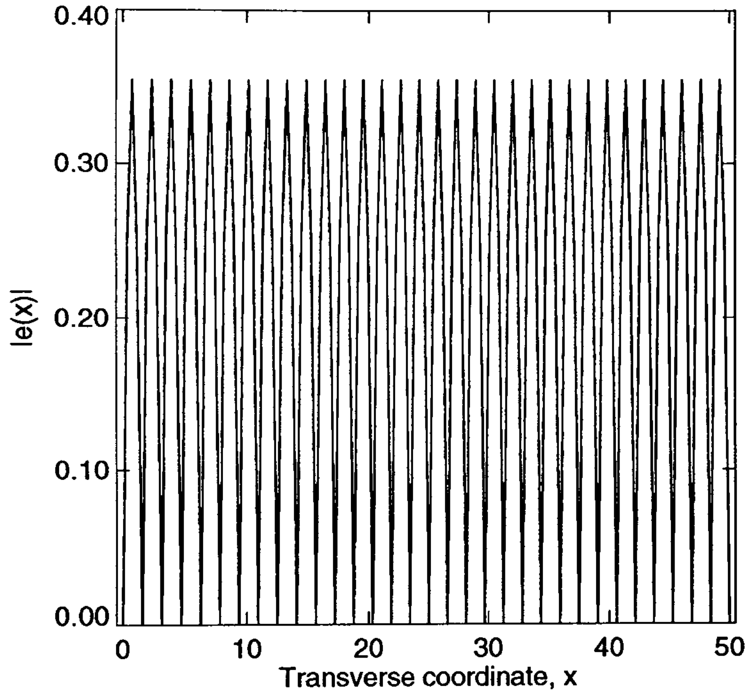

Figure 4.6: Modulus of the electric field, $|e|$*, as a function of transverse space coordinate,* x*. Parameters are* $a = 1$*,* $b = 1$*,* $\Delta = 4$*,* $\sigma = 1$*, domain width,* $L \approx 50$*,* $r = 1.1$

The main aim of this chapter is to study the transition between régimes of essentially travelling wave behaviour – like in figure 4.1 – and standing wave behaviour – like in figure 4.6. The size of the sink defect depends strongly on the value of the pump parameter, r and so if we use this as a control parameter there should be some critical value of $r = r_t$ where there is a transition from standing wave (SW) to travelling wave (TW) behaviour. In this section we attempt to characterise this transition.

To help us do this we require to find some parameter of the final state of the laser which characterises its 'standing wave-ness'. We choose to do this by introducing an 'asymmetry parameter' defined for a transverse domain $[0, L]$ as

$$A = \left| \int_0^{L/2} |e(x)| dx - \int_{L/2}^{L} |e(x)| dx \right| .$$

This parameter gives a measure of the difference in energy between the left and right halves of the transverse domain. If $A = 0$ then the output is probably symmetric[2] and we define it to be of standing wave nature. If $A \neq 0$ then the output is asymmetric and we say it is of travelling wave nature. A similar parameter could be defined characterising the asymmetry of the output profile in Fourier space rather than in real space. We have chosen to use A, defined in real space, because it is easier to extract from the numercal simulations.

Figure 4.7 shows the results of two numerical simulations of the Lorenz equations using reflecting boundaries. We have plotted the asymmetry parameter, A, as a function of time. In simulation *(a)* the laser tends to the symmetric state consisting of standing waves shown in the bottom left of the figure. The value of A tends to zero. In simulation *(b)* the laser tends to the asymmetric state shown in the bottom right of the figure. The corresponding asymmetry parameter tends to a constant non-zero value.

To characterise the transition between the two behaviours, we perform a number of such simulations and plot the resulting asymmetry parameter, A, against the pump parameter, r. Such a plot is shown in figure 4.8. The value of r_t for this size of domain, L, and system parameters is 1.26 ± 0.02.

Given that we now have a method for finding the value of the pump, r_t, where the transition occurs we can find r_t as a function of other system parameters. An important one is the size of the transverse domain, L. In figure 4.9 we show how r_t varies with L. The curve is just as one would expect. Large domains are very like

---

[2] *Note that $A = 0$ is a necessary but not sufficient condition for symmetry.*

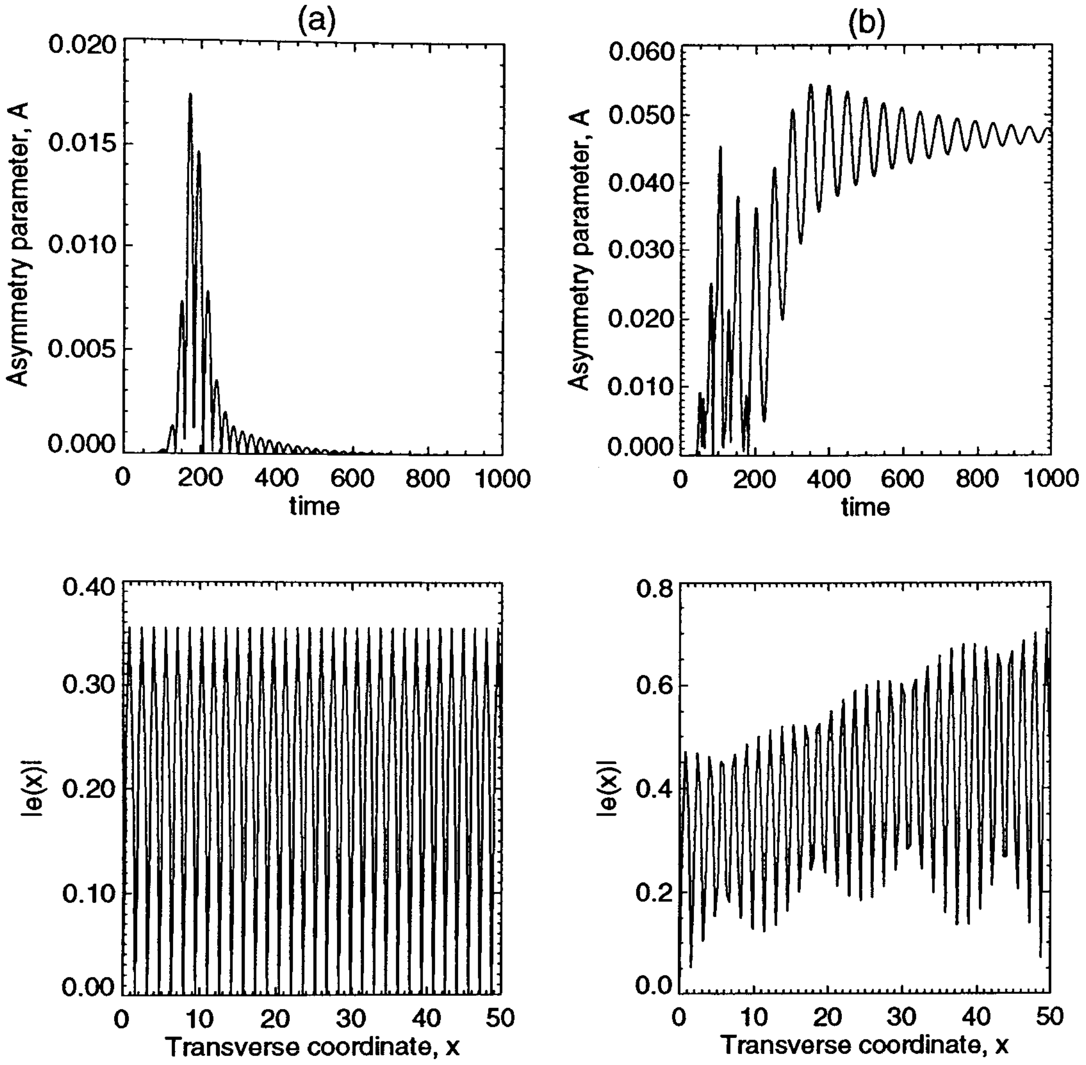

Figure 4.7: The results of two simulations of the Lorenz equations. Parameters are the same as in figure 4.1 except that in (a) $r = 1.1$ *and in (b)* $r = 1.3$. *In (a), the simulation tends to the symmetric output shown in the bottom left and by the asymmetry parameter,* A *tending to zero. In (b), the simulation tends to the asymmetric output shown in the bottom right and by the asymmetry parameter,* A *tending to a finite, non-zero value.*

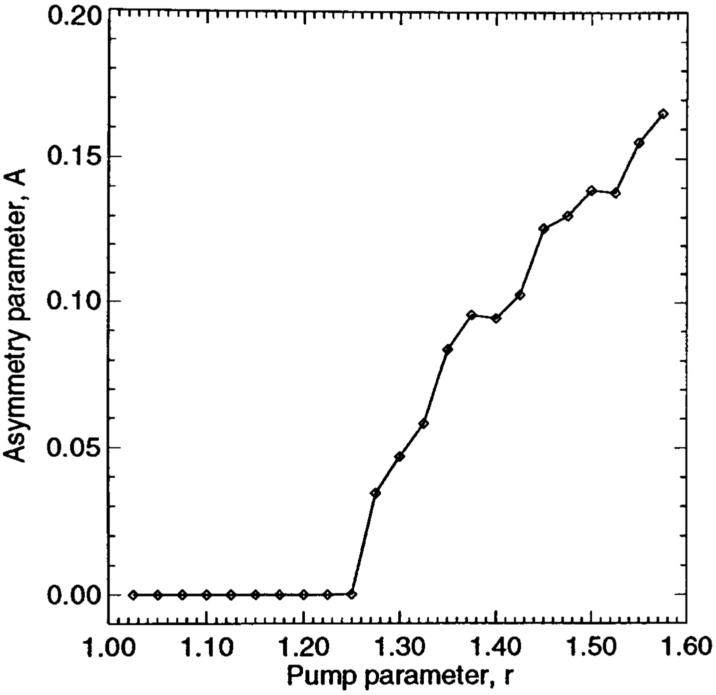

Figure 4.8: The asymmetry parameter, A, as a function of the pump parameter, r. The transition between symmetric and asymmetric output occurs for $r = r_t = 1.26 \pm 0.02$. Other parameters are the same as in figure 4.1.

the infinitely extended system in that travelling wave behaviour is seen for all values of r except those very close to threshold. For smaller domains the boundaries have a strong effect and the laser must be pumped far from threshold to see asymmetries.

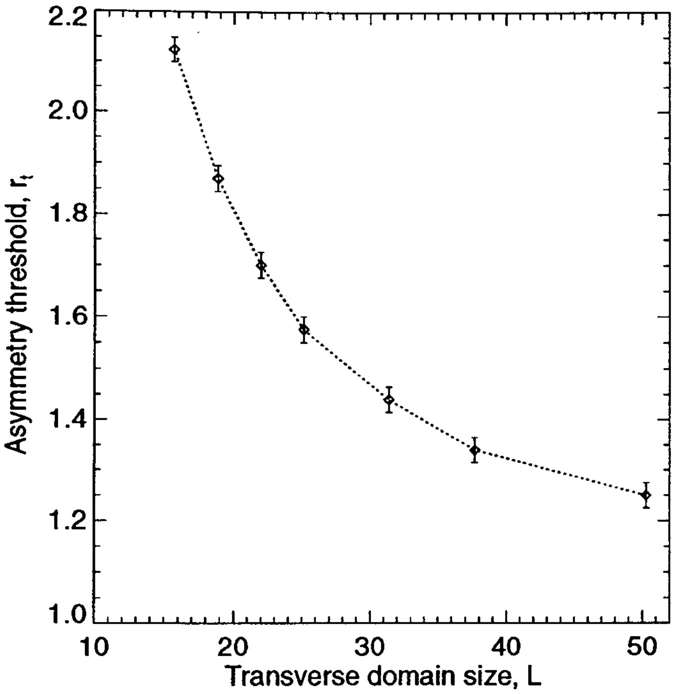

Figure 4.9: The value of the pump, r_t, at which the transition between standing wave and travelling wave behaviour occurs plotted as a function of the size of the transverse domain.

4.2.2 Two Transverse Dimensions

We now consider two-dimensional transverse domains with reflecting boundaries.

Square domain far from threshold

First of all, we will consider a square domain characterised by the cartesian coordinates (x, y). By analogy with the one dimensional problem we expect that, if the pump is above some threshold, we will see some sort of travelling wave behaviour and below the threshold to see standing wave behaviour.

Figure 4.10 is a frame from a movie showing the result of a numerical simulation of the complex Lorenz equations with zero boundary conditions on a square. The size of the transverse domain is approximately 50×50 units and the pump parameter is $r = 5$, so this figure is basically the two transverse dimension analogue of figure 4.1.

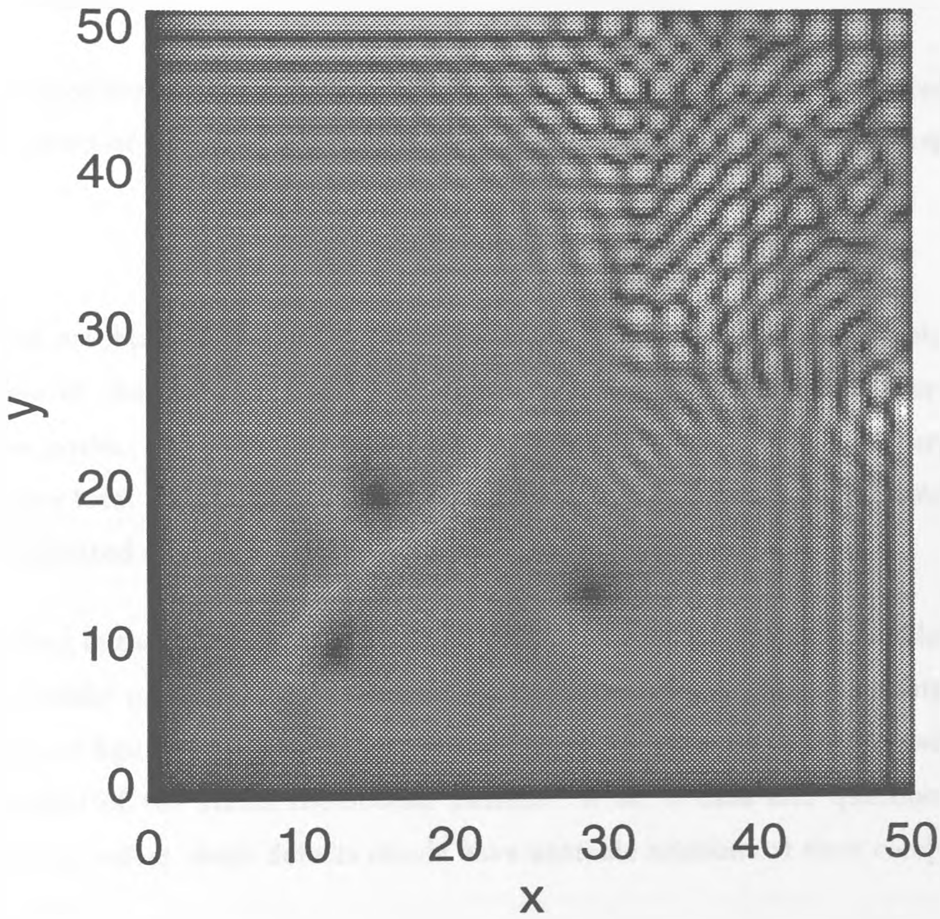

Figure 4.10: Modulus of the electric field, $|e|$, as a function of the two transverse coordinates, (x, y), for a domain width, $L \approx 50$: $a = 1$, $b = 1$, $\Delta = 4$, $\sigma = 1$, $r = 5$. White means high intensity and black means low intensity. The three dark patches at the lower left are vortex defects, which convect with the travelling wave to the sink at the upper right.

It appears that the sink defect is positioned along the upper and right edges of the square ; the source defect is located near the bottom left hand corner. Note that which corners the defects appear in depends entirely on the nature of the initial condition. The sink defect can appear in any of the four corners but the source defect is always found in the opposite corner so that the travelling waves propagate across a diagonal. This can be explained by the fact that the laser likes to lase with the travelling wave solution wherever possible and arranges itself so that the wave can propagate, without impedance, over as long a distance as possible. In a square, this means the direction across the diagonal.

The instability of the source defect manifests itself here as a series of *optical vortices*[44]. An optical vortex of charge Q is a localised region of space around which the integral

$$\oint \nabla \arg(e).d\mathbf{r} = 2\pi Q.$$

The vortices are born at the source and are swept across the domain roughly in the direction of the travelling wave towards the sink. We will comment later on their precise paths. They are born in pairs and the partners have opposite 'charge', conserving the total 'charge' of the whole simulation. Simulations with wider domains exhibit complicated spatial structures which persist for long times.

The sink defect in the upper right of the figure shows more than a passing resemblance to the rhomboidal patterns already seen in the infinitely extended system – compare figure 3.11 and figure 4.10. We should ask ourselves the question, is the standing wave comprised of the stable rhomboidal pattern? If so, it calls into question its description as a defect, since defects should have unstable solutions at their core[41], not stable ones!

The portion of figure 4.10 close to the upper right boundary is indeed comprised mainly of four Fourier amplitudes, placed on the vertices of a square in Fourier space, but an analysis of their relative phases shows that they are not of the stable type (solutions – 5. – as defined in section 3.7). This is to be expected from the simple analysis of the reflections of a travelling wave at a corner shown in figure 4.11. The incident travelling wave has a positive amplitude, indicated by the ⊕ symbol. At every reflection, the sign of the amplitude is reversed, indicated by the ⊖ symbol. The figure shows that the resulting standing wave close to the corner consists of two positive and two negative amplitudes. With reference to section 3.7 we see that this square pattern is an unstable one and this nicely rescues our idea of this localised structure as a defect.

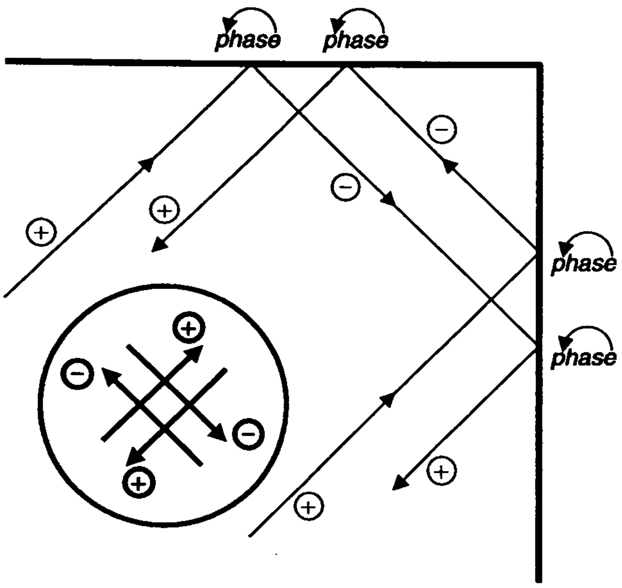

Figure 4.11: A diagrammatic representation of the reflection of a travelling wave at a corner. The standing wave generated consists of waves with phases $++--$.

As a slight aside, to get a point of definition straight, consider positions inside the square domain where the complex field is identically zero. At these positions the phase of the complex field is undefined and consequently they are termed *phase singularities*. There are two classes of such positions. The first is the optical vortex generated by the source. We call this object a *defect* of the travelling waves because it is a localised point whose core contains the nonlasing state (the zero) and is surrounded by a wave of reasonably constant amplitude. We will study the properties of these defects in section 4.2.3. The second class of zeros contains those seen at the nodes of the localised standing wave seen, near the top right of figure 4.10. We do not call these object defects since they are not localised with respect to any flat background.

Both the sink and the source are line defects. We have checked this by performing simulations, like the one in figure 4.12, with the upper and lower domain walls reflecting and the the left and right walls periodic. The simulations show that the sources and sinks line up along the reflecting boundaries and are stable in that position. This situation would not be so if the defects were not lines.

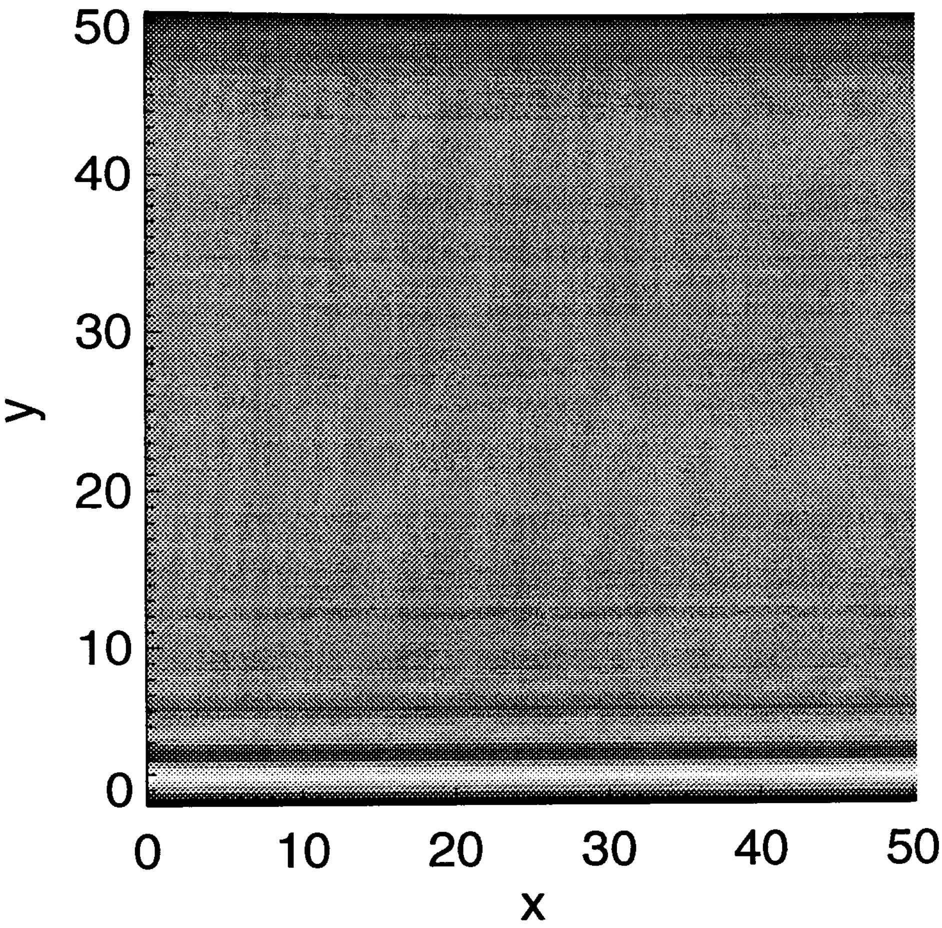

Figure 4.12: Modulus of the electric field, $|e|$, as a function of the two transverse coordinates, (x, y), for a domain width, $L \approx 50$: $a = 1$, $b = 1$, $\Delta = 4$, $\sigma = 1$, $r = 5$. The top and bottom domain walls are reflecting and the left and right walls are periodic. The source is positioned along the top boundary, the sink along the bottom. If the defects were not lines, this configuration would not be stable.

Square domain close to threshold

In the last section we showed the two dimensional analogue of figure 4.1. We will now show the analogue of figure 4.6 where, by making the pump close to threshold, we make the size of the sink defect comparable to the size of the transverse domain. We should expect to see the two-dimensional analogue of the standing-wave and we might expect that it should be more complicated, given the extra degree of freedom another dimension allows.

Figure 4.13 shows the results of four numerical simulations, all close to threshold, and for different random initial conditions. The simulations *(a)* and *(b)* are both for $r = 1.5$ but differ in their initial conditions. Simulation *(b)* has tended to a square pattern. At the centre, the squares are of the stable type discussed in section 3.7. The real part of the field there shows the characteristic flipping between stripes of perpendicular orientation. At the boundary, however, the squares are forced to be of the unstable type, just as we discussed in figure 4.11. The square solutions are preferred over the travelling waves at the centre of the domain because they have the same symmetry as the boundary. Simulation *(a)* shows similar features but consists of two domains of stable squares, π out of phase, and separated by a narrow region of unstable squares. The vertical line down the centre of the square is a *line defect*! This time it separates domains of squares of opposite phases.

The simulation *(c)*, for a pump $r = 1.3$, slightly closer to threshold shows a full domain of stable squares but this time rotated through an angle of 45°. The simulation *(d)*, for $r = 1.2$, shows that very close to threshold the effects of the boundaries are so strong as to forbid the stable squares and enforce a pattern not allowed in the infinitely extended system. In this case, the pattern selected involves 8 wavevectors, orientated as a set of two squares at an angle to one another.

These simulations go to show that the transition from boundary dominated patterns to ones of a travelling wave nature is much more difficult to quantify in 2D than in 1D.

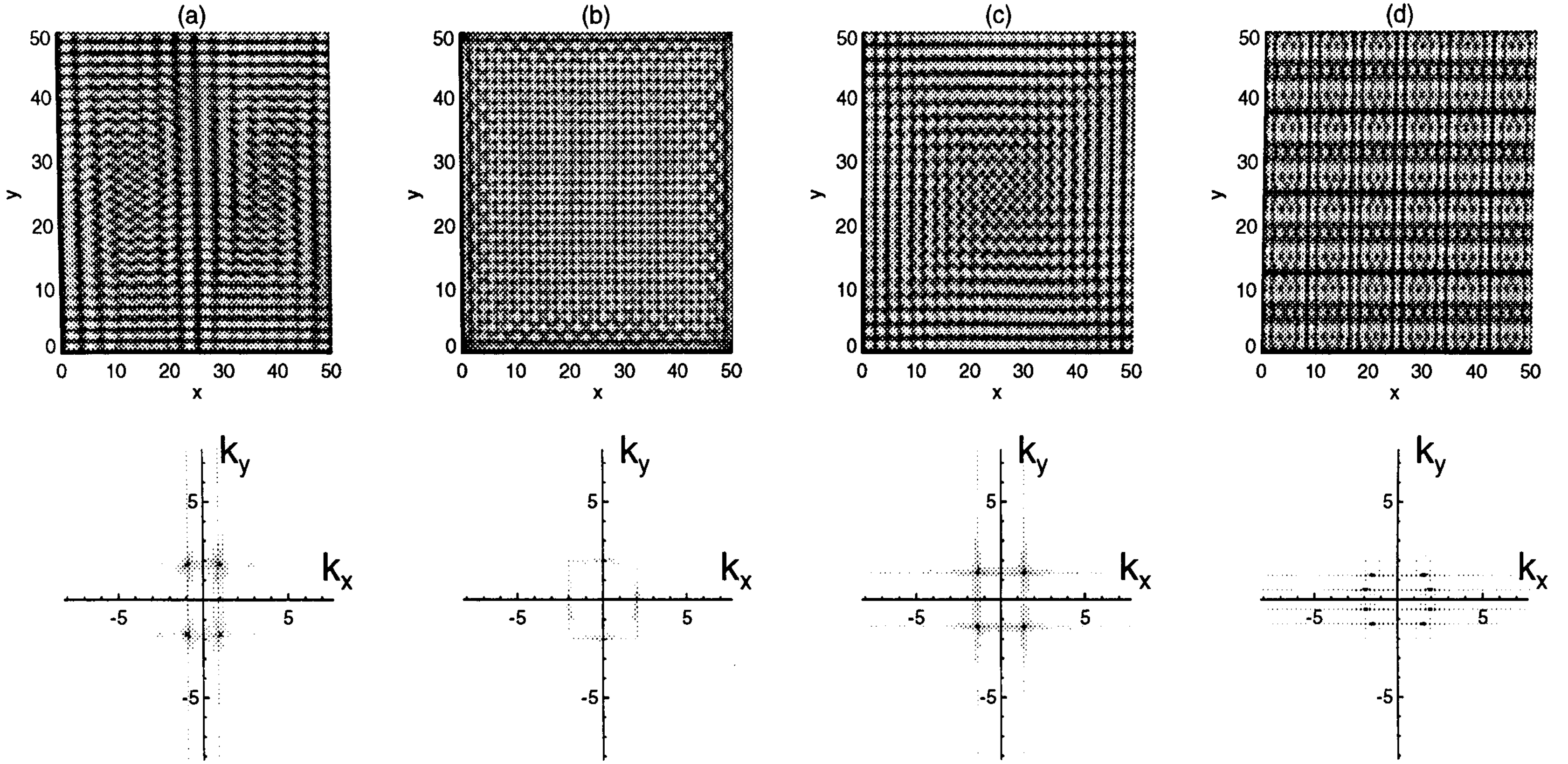

Figure 4.13: Numerical simulations, close to threshold, with reflecting boundaries on a square. (a) and (b) are for $r = 1.5$*, (c) is for* $r = 1.3$ *and (d) is for* $r = 1.2$*. Other parameters are the same as for figure 4.1.*

Circular domain far from threshold

We now consider the problem of reflecting boundaries on the edges of a circular transverse domain. This is, in some way a more physically relevant set of boundary conditions for a laser since, in most practical instances, the transverse confinement has cylindrical symmetry. Figure 4.14 shows the result of such a simulation for a value of the pump above the threshold for travelling wave type behaviour.

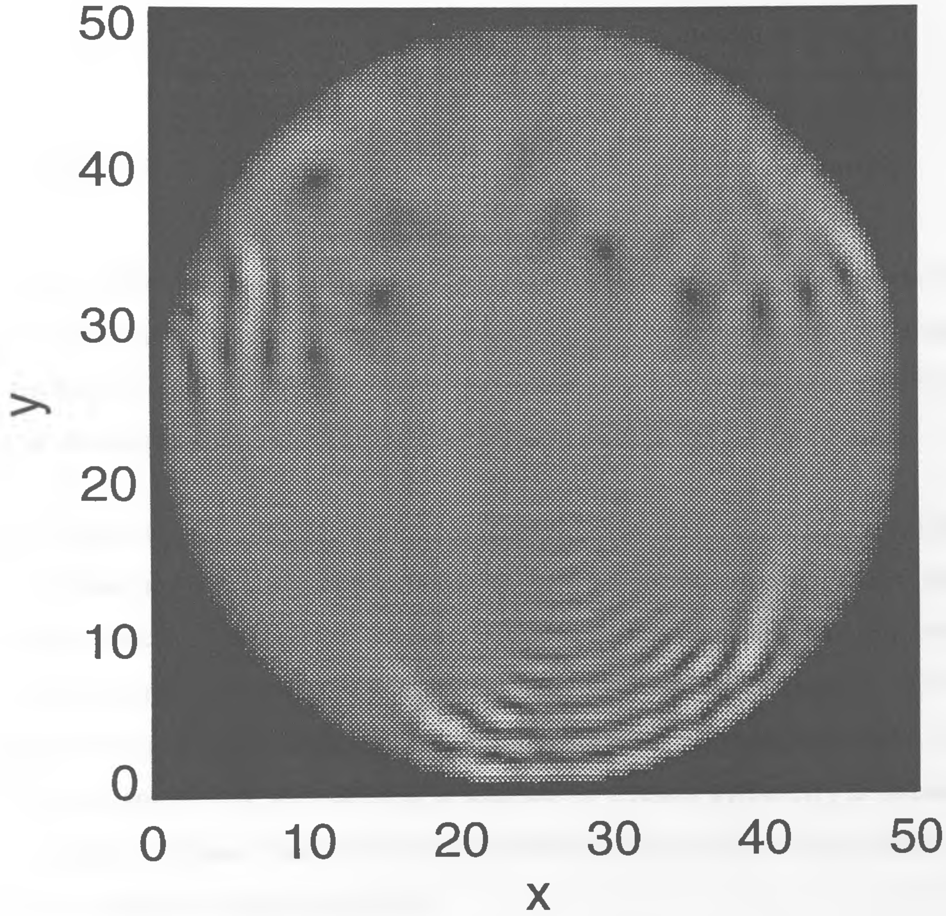

Figure 4.14: The results of a numerical simulation of the laser equations with reflecting boundary conditions on the edge of a circular transverse domain. Parameters are $a = 1$, $b = 1$, $\Delta = 4$, $\sigma = 1$, $r = 10$. *The transverse domain is of diameter* 50.

The source is positioned in the upper half of the image and the sink is positioned near the bottom. Travelling waves are generated at the source and propagate across the domain towards the sink. The dynamics of this simulation can be decomposed into dynamics on two time scales. The source is unstable and so, on relatively short time scales, of order the time taken for the waves to propagate across the domain, it generates a series of optical vortices which are advected along with the travelling waves. On much longer time scales, the source and the sink can undergo a 'walk' round the edge of the circle. This is not surprising since, provided they are diametrically opposite, any orientation of the source and sink is allowed. The noise being amplified because of the instability of the source defect can gently kick the source around on the circumference of the circle, inducing a motion.

Circular domain close to threshold

For the square refelector close to threshold we saw that the square solutions of the infinitely extended system were in some way enhanced by the symmetry of the boundary. No solution of the infinitely extended system posesses circular symmetry and so, for a circular domain we are left with no idea of what will be seen.

Figure 4.15 shows the results of a numerical simulation with $r = 1.2$ for initial conditions of noise around zero. The simulation never[3] reaches an asymptotic state but remains dynamic. Different parts of the pattern appear to rotate about the centre at different rates and in different directions in a very erratic manner. On the right of figure 4.15 we have plotted the time averaged intensity of the dynamical profile. The image shows that something approaching a solution of circular symmetry is obtained after this averaging process. Such phenomena have been observed in experiments on the Faraday instability in fluid layers.[45].

---

[3] *as far as we can tell*

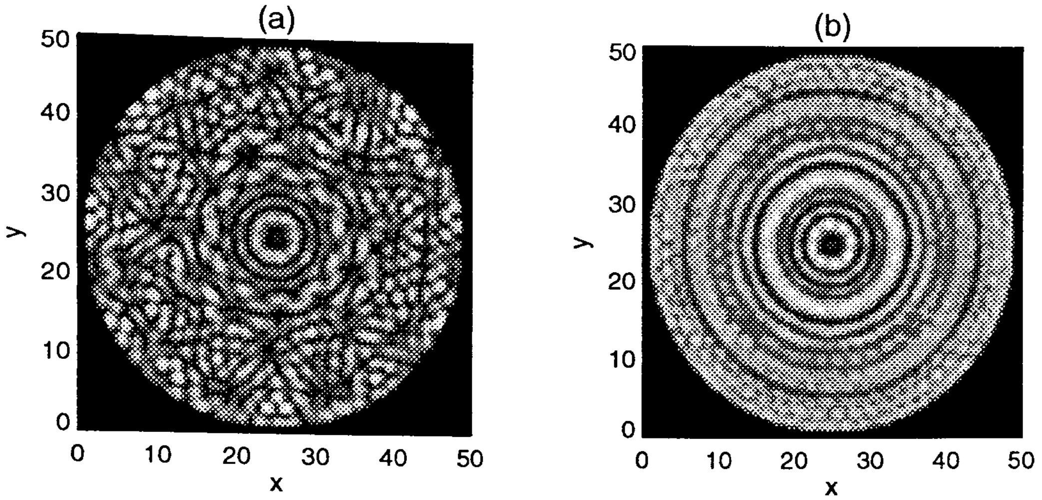

Figure 4.15: The results of a numerical simulation with a circular boundary. The modulus of the field, shown on the left, never settles to an equilibrium pattern. The temporal average of the dynamic profile is shown on the right.

4.2.3 Source Defect Revisited

The main purpose of this chapter is to study of the threshold for the transition between standing wave and travelling wave behaviours, but there are some other interesting phenomena along the way. One of these is the source defect and its instability in 1D. Another point of interest is the nature and propagation of the optical vortices in 2D

Source Instability in 1D

We have already given a brief explanation, based on the amplitude equations, for this instability and we have seen various numerical examples of it – 'blips' in 1D and optical vortices in 2D. The question now is, how good are the amplitude equations at describing the numerics? The answer is: not too good!!

To test this, we have performed a number of 1D numerical simulations with reflecting boundaries, each with size of domain $L \approx 100$ and each with a different value of the pump parameter, r, in the range $[1.5, 8]$. In each simulation we arranged the initial conditions so that, after the transients are over, the output consists of a sink on the left hand boundary and a source on the right. For this range of pump values, the domain is wide enough so that we can neglect any interaction between the defects. The unstable source produces a series of 'blips' in time which propagate leftwards with the travelling waves and so, if we were to position a detector, measuring the field intensity, at a position close to the source we should observe a non-stationary time signal from it. If the source is stable however, the signal from the detector will be constant.

It is very easy to introduce such a 'detector' into the numerical simulations and the results are shown in figure 4.16. On the left, we show the final states of the simulations at each r as shaded horizontal bar. Black means low intensity and white means high. The source defect is at the right and the sink at the left and note that this is a snapshot in time. Most simulations show a dynamical behaviour. The black vertical line shows the position of the detector used to probe this behaviour. Signals from this detector are shown in the bottom diagram. In the diagram on the right, we show the *standard deviation* of the trace from the detector as a function of the pump parameter. A zero value of the standard deviation means that the intensity from the detector is constant and the source is stable ; a non-zero value means there are fluctuations in the intensity and the source is unstable. Note that $t = 0$ in this figure corresponds to a time well into the simulation after the transients are over.

What is the point of all this? I hear you cry. Well, the analysis of the amplitude equations told us that the source defect was unstable for values of the pump less than some critical value r_c given by equation (4.2). For the parameters we have been using, the numerical value of $r_c = 2$. This bears little resemblance to what is seen in the numerics! Why should the numerics and the amplitude equations disagree so vehemently? There are a number of possible reasons. Firstly, the amplitude equations are strictly only valid in a very small range close to threshold – remember we treated $\sqrt{r-1}$ as a smallness parameter in their derivation. For the situations we have been studying, this approximation is broken by a considerable margin! Secondly, and of course related, is the fact that the amplitude equations describe slow spatial and temporal modulations of the amplitudes of the active modes. The defect structures we are attempting to study push the bounds of these approximations also. Lastly,

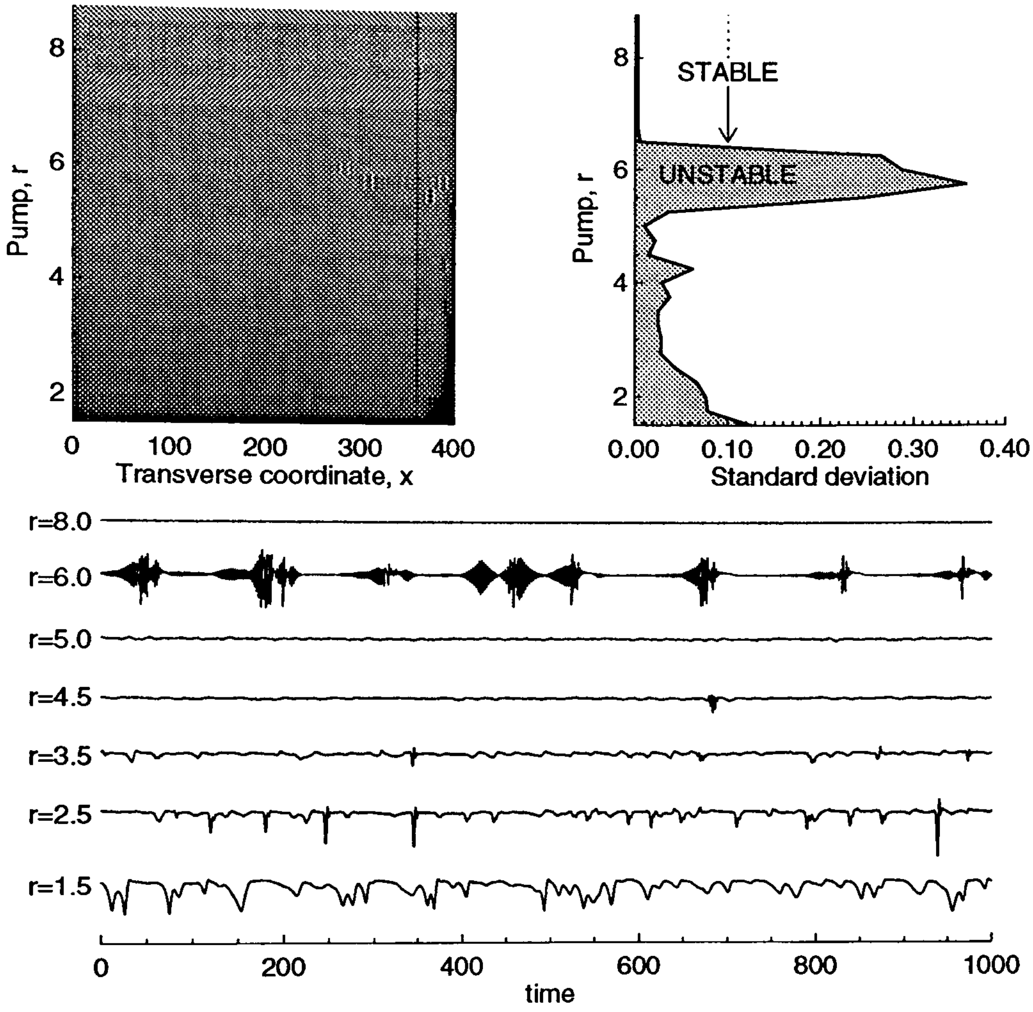

Figure 4.16: Results of numerical simulations characterising the instability of the source defect. The diagram on the left shows the results of thirty 1D numerical simulations for a range of values of the pump, r. The diagram at the bottom shows the time series from the detector positioned close to the source defect. The diagram at the top right shows the standard deviation of these signals, indicative of the stability of the source.

perhaps the amplitude equations do describe the numerics well and, for $r > r_c$ there is another instability mechanism responsible – perhaps the Eckhaus instability of the travelling waves?

The take home message is that the source defect appears to be a very complicated entity indeed!!

Vortices in 2D

We have seen in the numerical simulations that, in 2D, the instability of the source defect results in a series of optical vortices being produced. In this section we briefly characterise these vortices and comment on their trajectories and velocities in the transverse domain.

Firstly, we consider the topological charge of the vortices and their transverse size. Figure 4.17 shows results of numerical simulations with a square reflecting boundary for three values of the pump, $r = 2, 3$ and 5. We do not plot the whole transverse domain, but only a small region close to one of the vortices which have been generated at the source and are being swept across the domain with the travelling waves. To show the nature of the defects more clearly we have plotted the real part of the laser field, $\mathcal{R}e(e)$ as a function of the transverse coordinates. In this way, the vor-

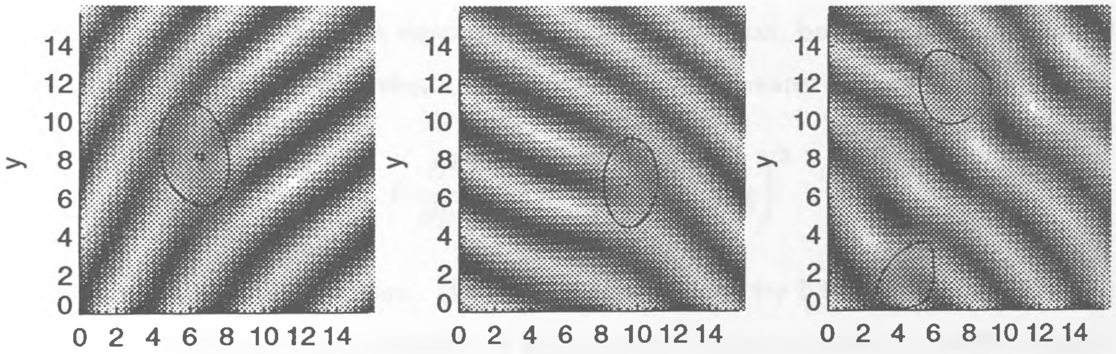

Figure 4.17: A 'close-up' of the optical vortices in a square reflecting boundaries simulation. We plot the real part of the electric field as a function of the transverse coordinates. The areas enclosed within the curves overlayed in black are related to the transverse size of the vortices.

tices appear as dislocations in a pattern of stripes. The orientation of the stripes is perpendicular to the direction of travelling wave propagation. In all the simulations, the dislocation corresponds to the insertion of one extra stripe and this implies that the *topological charge* of the defects is $Q = \pm 1$. The closed curves overlayed on the images show a contour where the modulus of the laser field is half of its maximum value – the contour shows the full-width half-minimum of the dip which is the vortex. The area enclosed by these contours gives an estimate of its size.

Can we obtain an analytical estimate for the size of the vortex as a function of the system parameters? In principle yes. In his Ph.D thesis, Gil[26] demonstrated an analysis technique which he used to obtain information about the nature of the vortex solution in a real CGL equation. The technique is based on deriving a free-energy for the equation (in a similar way to the analysis in section 3.8) and minimising it with respect to changes of the parameters of a trial function inserted for the vortex. In this way it can be shown that the size of the vortex is proportional to $m/(r-1)$, where m is the topological charge of the vortex. It's size, therefore, should depend inversely on the distance above threshold. The slight problem is that the travelling waves in our system are not described by a CGL equation, but by a similar equation containing the Newell-Whitehead derivative[10]. This means replacing

$$\left(\frac{\partial^2}{\partial x^2} + \frac{\partial^2}{\partial y^2}\right) \rightarrow \left(\frac{\partial}{\partial x} + \frac{1}{2ik_c}\frac{\partial^2}{\partial y^2}\right)^2$$

in the standard CGL equation. Because of the asymmetry between the x and the y directions, performing the analysis on this revised equation proves to be too complicated. We hypothesise, however, that one of the consequences of this asymmetry will be that the vortex will have a different size in the x and the y directions. That is to say that the vortex will be 'squashed' in some way by the fact that it is on a travelling wave and not on a uniform background.

The scaling of the size of the vortex with the pump and its 'squashing' are nicely shown in figure 4.17. The area enclosed by the contours becomes larger for decreasing pump and the contours are roughly elliptical in shape, not circular ; the size of the vortex being larger along the direction of propagation of the travelling wave. The vortex sizes are quantified in table 4.1 which gives the area enclosed by the contour for the three pump values.

r=2	r=3	r=5
Area=16.3	Area=11.3	Area=10.2

Table 4.1: The area of the optical vortices generated by the source for three values of the pump.

Next, we consider the motion of the vortices across the domain. Figure 4.18 shows the results of a study of a number of vortex trajectories. We ran the simulation shown in figure 4.10 further in time, taking note of the positions of the vortices at regular intervals. The plot on the left of figure 4.18 shows the vortex trajectories as black lines, overlayed on the image of the initial field modulus for comparison. A few comments about this figure are needed. We have only tracked the vortices in the bottom left triangle of the domain so as to easily distinguish vortices from other zeros of the field associated with the sink defect. Note also that, at any one time, only between two and four vortices were visible in the domain. The large number of trajectories is simply because the simulation was run over a period of time over which there were a large number of vortices generated at the source. The discontinuities in the trajectories are because of the inefficiency of the method we have used to extract the vortex positions.

We notice that the trajectories cross in some places. This shows that the vortices are not moving in a static potential. The paths starting near the source seem to be attracted towards the boundaries before 'breaking free'. This attraction can be explained by the fact that the vortex sees its reflection in the boundary. It's reflection has the opposite topological charge and it has been shown that, just like electrically charged particles, oppositely charged vortices attract[46]. After the vortices 'break free' from the boundary they travel in a spread of directions. This is attributed to a further boundary effect.

What of the vortices' speed? The group velocity of the travelling waves, computed from equation (3.19) for these parameters, is $v_g = 2$. How does the velocity of the vortices, v, compare to this? The middle plot in figure 4.18 shows the components

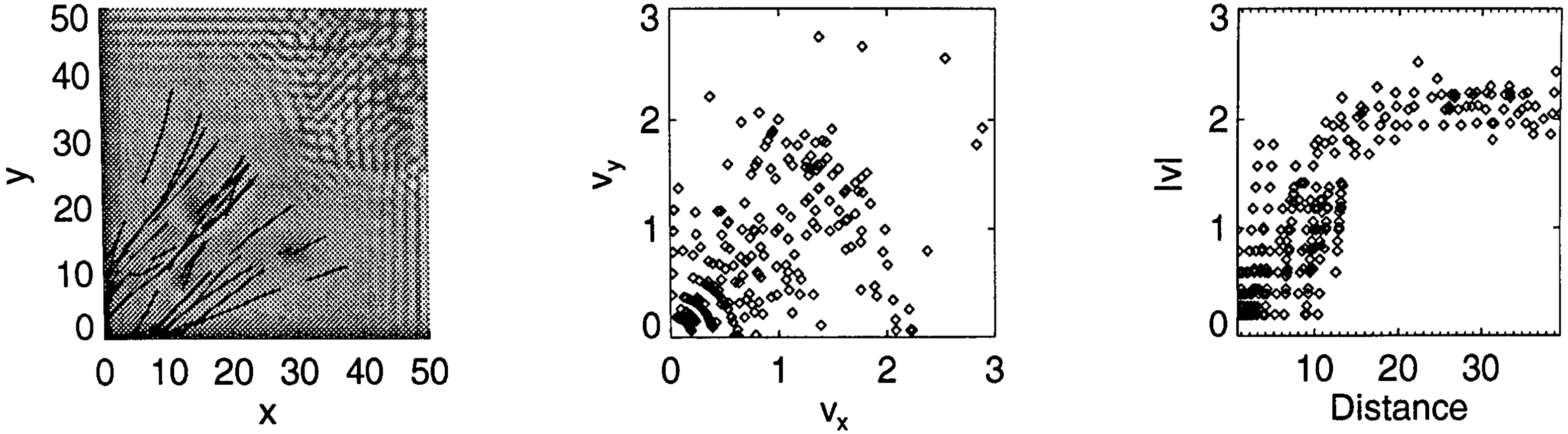

Figure 4.18: Results of a study of the vortex trajectories and speeds. See the text for details.

of the v along the x and y directions for each time interval in the simulation. It appears that, for any given angle of propagation, the vortex speeds are distributed approximately[4] in the range $|\mathrm{v}| \leq 2$. What is the cause of this distribution of speeds?

The plot on the right of figure 4.18 goes some way to answering this. It shows the vortex speed as a function of its distance from the corner. Far away, the vortices move at the group velocity of the travelling waves, $|\mathrm{v}| = v_g$, but close to the source they are slowed down.

4.3 Gain Guiding

In the previous sections we have dealt with the problem of reflecting transverse boundaries. This study, although not particularly physical for many laser systems has let us establish the main factors at work in the way transverse boundaries affect the travelling waves. We have introduced the notion of sources and sinks of travelling waves and how their size and stability affect what is seen in the final output.

In this section we deal with a slightly more physical type of boundary condition in which the lasing is confined to some portion of the transverse domain by restricting the area which is pumped. In chapter 2 we called this *gain guiding*. In the modelling of the microchip laser in that chapter we assumed a gain profile which was a cylindrically symmetric Gaussian. In this section, for computational convenience we have chosen to use a gain profile, $r(x,y)$ based on a hyperbolic tangent function

$$r(x,y) = \Big[1 - \tanh\Big(10(\rho - \rho_1)/CW\Big)\Big]/2$$

where $\rho^2 = x^2 + y^2$ and we have defined

$$\rho_1 = (PW + CW)/2,$$

---

[4] *Speeds outside this range may be due to inaccuracies in the extraction of the vortex positions from the simulations.*

in terms of the *Pumped Width*, PW, and the *Curvy Width*, CW. The pump profile is shown diagrammatically in figure 4.19.

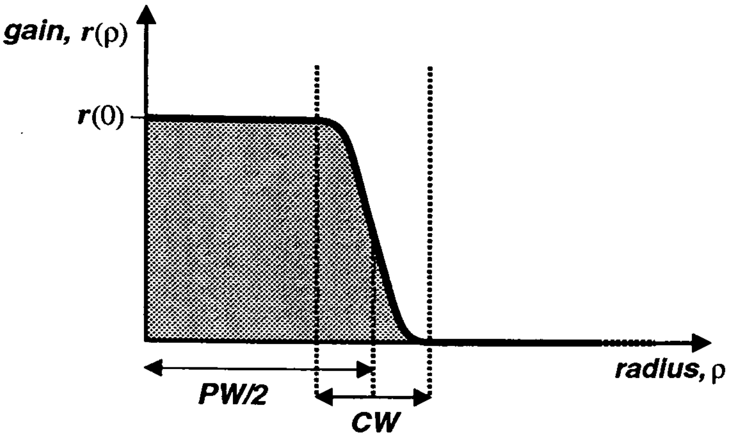

Figure 4.19: The gain profile considered in this section is an hyperbolic tangent function of a width characterised by CW*, and centred on a particular radius characterised by* PW*.*

4.3.1 One Transverse Dimension

In the section on reflecting boundaries we used the pump, r, and the size of the transverse domain, L, as control parameters in looking for the transition between standing wave and travelling wave behaviour. In this section our control parameters will be the pump, r, and the two parameters characterising the pump profile, PW and CW. As a simplifying step we choose to restrict ourselves to the sub-class of these pump shapes with $CW = 0$ – top-hat pumps.

Small aspect ratio

Figure 4.20 shows the results of numerical simulations of the Lorenz equations in one transverse dimension for four values of PW ranging from narrow to broad.

Let us treat each of them in turn. In simulation *(a)* the gain profile is very narrow indeed. In fact, it is so narrow that the field profile has the most fundamental shape

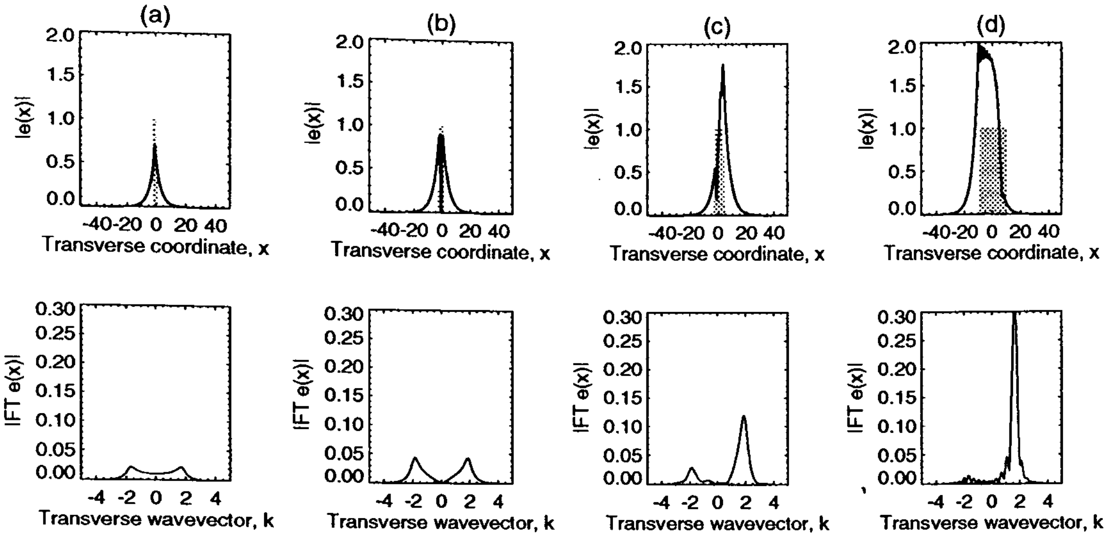

Figure 4.20: The final states of numerical simulations for the four values of the pump width (a) $PW = 1.88$, (b) $PW = 3.14$, (c) $PW = 6.28$, (d) $PW = 18.85$. Other parameter are $a = 1$, $b = 1$, $\Delta = 4$, $\sigma = 1$, $r = 5$. The top row shows the laser field amplitude as a function of the transverse coordinate, x. The shaded areas are those experiencing gain. The bottom row shows the spatial Fourier transform – the far field – of the output profiles.

possible, the one dimensional analogue of the $(0,0)$ gain guided mode discussed in chapter 2 – compare with figure 2.12. Note that the field decays exponentially in the wings just like those in the gain guiding section. It is interesting to look at the far field, the Fourier transform, of this output profile ; the far fields are shown in the bottom row of figure 4.20. Note that, even though for these parameter values the laser output is not in any way travelling-wave like, its far field still consists of two broad peaks roughly peaked at $\pm k_c = 2$. Can we explain this based on the work we did already on the small-aspect-ratio gain guided modes? The answer is yes.

When the gain profile is very narrow, the mode consists mainly of its exponential tails. In section 2.4.1 we obtained expressions for these tails ; we can do a similar analysis here for the Lorenz scaling. We assume one transverse dimension and that the laser is unpumped, $r = 0$. Steady state solutions of the Lorenz equations which satisfy the boundary conditions

$$\lim_{x \to \pm\infty} e(x) = 0$$

are of the form

$$e \sim \exp(\lambda x - i\Omega t),$$

where λ is a root of

$$\lambda^2 + \left(\frac{\Omega + i\sigma}{a}\right). \tag{4.3}$$

For positive detunings these solutions take the form of travelling waves with exponentially decaying amplitudes. Their decay rate is given by the real part of the λ and their wavevector is given by its imaginary part. The two roots of equation (4.3) indicate that left and right travelling waves are possible but, in order to honour the boundary conditions, we are required to choose a backward travelling wave for $x \longrightarrow -\infty$ and a forward travelling one for $x \longrightarrow \infty$. This implies that the pumped region should always act as a net *source* of travelling waves. This is important and we will come back to it shortly.

We have established that the solution in the wings is a travelling wave propagating outwards. For very narrow pump profiles, the laser field is made up mostly of its wings and so it is not surprising that its Fourier transform is strongly peaked at the wavevectors corresponding to the forward and backward waves. The peaks are not sharp because the waves are strongly damped as they propagate into the unpumped region. In the limit $\sigma \ll \Omega$, exactly the one studied for the microchip lasers, the wings become almost flat, the peaks in the Fourier transform become centred at $k = \pm k_c$ and they become narrow.

In simulation *(b)* the gain profile is slightly broader than in *(a)*. As we commented in chapter 2, broadening the gain profile tends to lower the threshold for the higher order transverse modes and, since the parameters here do not strongly disadvantage the higher order modes, the simulation shows a mode corresponding to the next transverse mode, the $(0, 1)$. The Fourier transform still shows a double peaked structure.

In simulation *(c)* the gain profile is sufficiently broad so as to allow the asymmetric mode profile shown. The Fourier transform is also asymmetric. In simulation *(d)* the symmetry is also broken and the final state and its Fourier transform look very similar to those seen for the reflecting boundaries. A travelling wave is born from a source at the left. It propagates across the domain until it reaches the other side of the gain profile. The sharp edge of the gain profile acts as a partially reflecting mirror for the waves, some being reflected to form the localised standing wave and some being transmitted to form the right hand wing of the profile.

The slight problem in this description is that it does not satisfy the condition we established already that, because of the boundary conditions at infinity, the pumped region should act as a net source of waves. This requirement *is*, on closer inspection, met by the results of the simulations. The sources in *(c)* and *(d)* are, in fact, positioned at the left hand extremes of the pumped regions, not at the left hand extreme of the output profile. The waves generated at the source not only propagate forwards across the domain as we have described but also backwards, decaying as they propagate into the unpumped region.

Large aspect ratio

The question now remains to be answered as to what happens in larger aspect-ratio simulations? Figure 4.21 shows the results of two simulations each with the width of the pumped region, $PW \approx 50$ – it is the gain guiding equivalent of figure 4.1. In the simulation on the right, for pump $r = 5$, the field is essentially of travelling wave nature, as described above. In the simulation on the left however, for pump $r = 1.3$, the field has converged to the gain guiding analogue of the reflecting boundaries standing wave. Standing waves are not permitted to uniformly fill the pumped region because, as we showed above, it must act as a net source of travelling waves. Close to threshold, that is for pumps below the threshold for the transition to travelling wave behaviour, these conditions are met by the field profile shown. An extended source-like object at the centre generates waves which propagate away. Because of its extended nature, there is an area near its core which consists of standing waves where the counterpropagating waves interfere. It is unclear whether or not this object

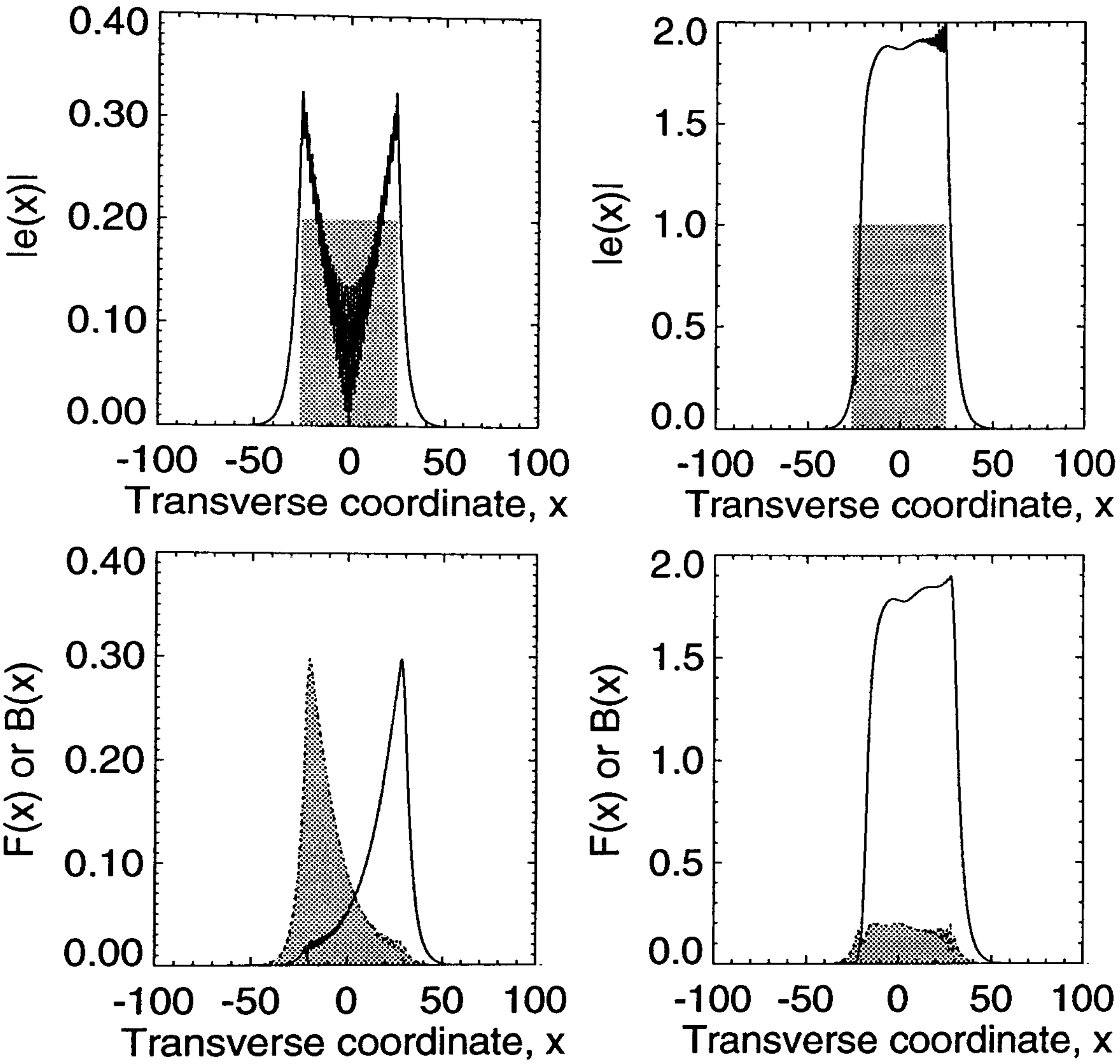

Figure 4.21: The results of two simulations with pump width $PW \approx 50$. On the left, with pump $r = 1.3$, the simulation converges to the gain guiding analogue of the reflecting boundaries standing wave. On the right, with pump $r = 5$, a solution of travelling wave nature is observed. In the top row, the shaded area represents the that which sees gain. In the bottom row, the forward and backward field amplitudes have been extracted ; the areas under the backward wave amplitudes are shaded grey.

can be described as the source defect as its core does not contain the nonlasing state, but instead a standing wave which is not even the unstable one. For these parameter values, the unstable standing wave solution has amplitude ≈ 0.3 and the standing wave at the core of this object has amplitude ≈ 0.05.

4.3.2 Two Transverse Dimensions

In this section we go on to generalise the one dimensional work on gain guiding to two transverse dimensions. We will consider only cylindrically symmetric gain profiles but, as we will see this does not necessarily lead to cylindrically symmetric patterns. We will again consider the case of top-hat pumps given when the parameter $CW = 0$.

Small aspect ratio

Figure 4.22 shows the results of numerical simulations with two transverse dimensions for the same parameters as in figure 4.20. The figure shows the modulus of the electric fieldm its real part and its spatial Fourier transform for four values of the pump width, PW. Similar behaviour to the one dimensional case is observed. For simulations *(a)*, *(b)* and *(c)*, the pump is sufficiently narrow to impose a cylindrically symmetric output shape, effectively quashing the travelling wave nature of the field. In fact, for these three simulations, the output profiles can be represented as simple linear combinations of the gain guided modes described in chapter 2.

An interesting point to note is that, in stark contrast to those for single Gauss-Laguerre modes, the phase singularities we find with gain guided modes have the classic spiral structure in the real part[47]. As shown in appendix B the Gauss-Laguerre modes can be written as a *real* function of the radius multiplying $\exp(im\phi + i\omega t)$ and so modes with nonzero m have a helical phase-fronts. In contrast, and in the limit of large radii, the gain guided modes can be written as a *real* function of the radius multiplying $\exp(im\phi + ikr + i\omega t)$ whose phase-fronts are the precessing spirals shown in figure 4.22.

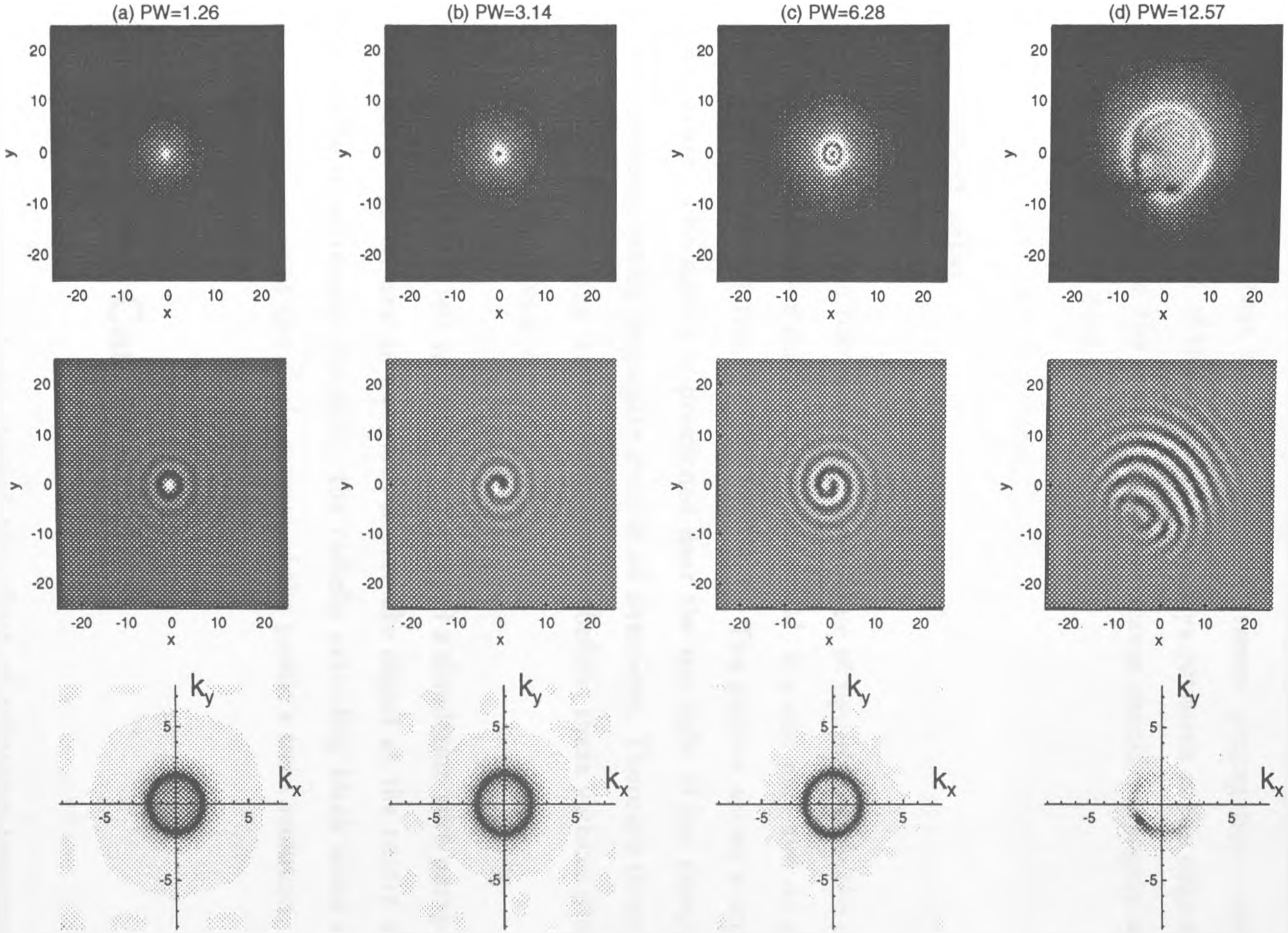

Figure 4.22: The results of four numerical simulations with gain guiding. The top row shows the modulus of the electric field as a function of the transverse coordinates, the middle row the real part of the field and the bottom row, the spatial Fourier transform. Parameters are the same as for figure 4.20.

In simulation *(d)* of figure 4.22, the cylindrical symmetry is broken and the real part of the field and the Fourier transform shows strong evidence for a travelling wave nature to the field. A source of travelling waves is positioned in the lower left of the profile and waves generated there propagate across the domain towards a diametrically opposed sink. Note that the direction of the waves' propagation – perpendicular to the stripes in the plot of the real part – is always outwards at the edge of the pumped region. This satisfies the requirement that waves should propagate away from the pumped region in all directions.

Large aspect ratio

Figure 4.23 shows the two dimensional analogue of figure 4.21. In the column on the right we show the modulus of the electric field, it's real part and its spatial Fourier transform for a simulation with pump $r = 5$. The pattern shows a strong travelling wave nature. The source is positioned near the top right of the pumped region and generates waves which propagate away in all directions. There are three optical vortex defects of the travelling wave visible. Just as before, these vortices propagate across the domain at the group velocity.

In the column on the left we show the results of a simulation with pump $r = 1.3$. Just as in figure 4.21 we see an extended source-like object at the centre of the domain. The profile is extremely dynamic: the radially extending black areas in the top left diagram move around the circle as part of the profile's time evolution.

4.4 Curved Cavity Mirrors

In previous sections we have studied the effect of reflecting transverse boundaries and those imposed by gain guiding. We will now discuss the effect of curved cavity mirrors. As a form of transverse field confinement, curved mirrors is probably the most widespread in laser systems and so their effect on the travelling waves is probably the

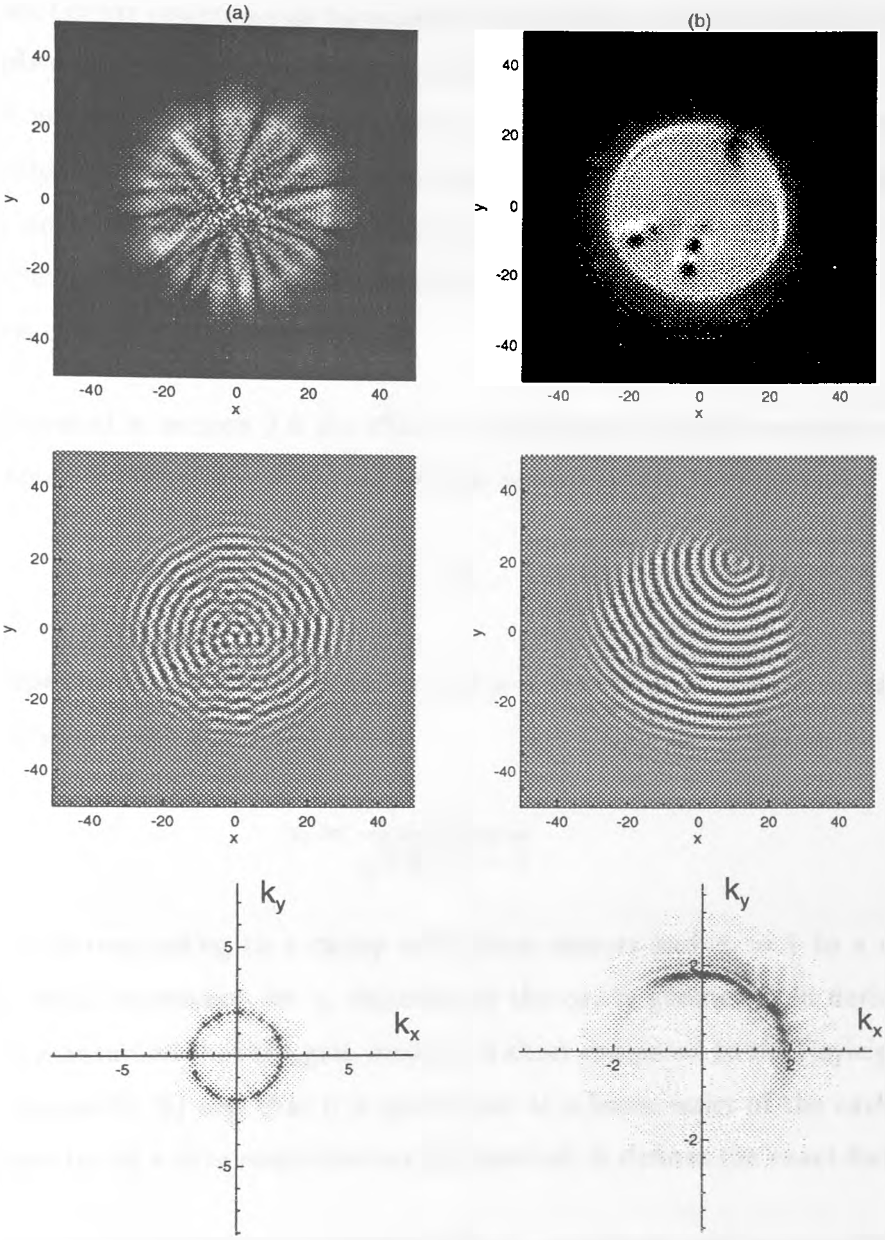

Figure 4.23: The results of two simulations with a pump width $PW \approx 50$. On the left, with pump $r = 1.3$, the simulation converges to the gain guiding analogue of the reflecting boundaries standing wave. On the right, with pump $r = 5$, a solution of travelling wave nature is observed. The top row shows the amplitude of the laser field, the middle row its real part and the bottom row shows its spatial Fourier transform.

most important of any considered here.

The complex Lorenz equations we have used in this thesis up to now have been derived assuming plane-parallel cavity mirrors. To study a different cavity we must go back to appendix A and re-derive the field equation and the mean-field limit for the Maxwell-Bloch equations. The exact procedure is very similar to the one we have already used and so we only give the resulting equations and refer the interested reader to the seminal paper on the subject[2]. For a slightly more illuminating discussion see the Ph.D. thesis of Kent[48].

As we commented in section 2.6 the effect of introducing curved mirrors is to modify the transverse Laplacian in the Maxwell-Bloch equations, (A.34) – (A.36),

$$\nabla_T^2 \rightarrow \tan^{-1}\gamma_c \left[\frac{1}{\gamma_c}\nabla_T^2 - \frac{4\gamma_c k^2}{L^2}\rho^2\right]$$

where γ_c depends on the cavity geometry and ρ is the radius in the transverse plane. For the cavity in figure B.1

$$\gamma_c = \frac{1}{\sqrt{2R_o/L - 1}}$$

with $\gamma_c = 0$ corresponding to a cavity with plane mirrors and $\gamma_c = 1$ to a confocal cavity. The exact expression for γ_c depends on the cavity geometry. In deriving this correction it is assumed that the gain medium is short compared to the Rayleigh range (defined in appendix B) and that it is positioned at a beam waist of the cavity. This final condition is not a firm restriction on the method, it defines the exact form of γ_c.

We insert this correction into the Maxwell-Bloch equations and re-scale them into the complex Lorenz form to obtain our working set of equations for this section

$$\frac{\partial e}{\partial t} = ia\frac{\tan^{-1}\gamma_c}{\gamma_c}\left[\nabla_T^2 - 4\gamma_c^2\rho^2\right]e - \sigma e + \sigma p, \tag{4.4}$$

$$\frac{\partial p}{\partial t} = re - (1 + i\Delta)p - ne, \tag{4.5}$$

$$\frac{\partial n}{\partial t} = -bn + \frac{1}{2}\left(ep^* + e^*p\right). \tag{4.6}$$

Linear Analysis

As a slight review to pave the way for what comes next, recall that in section 3.2, for plane mirrors, we performed a linear stability analysis of the non-lasing state to perturbations with some transverse wavevector, $\mathbf{k}$. These Fourier modes diagonalised the transverse Laplacian and we found the neutral stability curve giving the threshold for an instability to each of these modes. We also found that modes with equal $|\mathbf{k}|$ were degenerate – they had the same threshold and frequency.

We will now perform a similar linear stability analysis, not using Fourier modes, but *Gauss-Laguerre* modes. These modes are eigenfunctions of the operator

$$\left[\nabla_T^2 - 4\gamma_c^2\rho^2\right]$$

just as the Fourier modes are eigenfunctions of ∇_T^2. They are characterised by the indices (p, m) (c.f. chapter 2) and are given by the formula

$$A_{pm} = \sqrt{\frac{(2\gamma_c)^{|m|+1}}{\pi}}\sqrt{\frac{p!}{(p+|m|)!}}\;\rho^{|m|}L_p^{|m|}\left(2\gamma_c\rho^2\right)e^{-\gamma_c\rho^2}e^{im\phi}$$

where $L_p^{|m|}(x)$ are Laguerre polynomials, as defined in appendix B. The associated eigenvalues are

$$-4\gamma_c(2p+|m|+1)$$

just as those for the Fourier modes were $-|\mathbf{k}|^2$. The Gauss-Laguerre modes form a complete orthonormal basis and so any laser profile can be expressed as a linear combination of them. Of course, a very large number may be necessary to represent 'difficult' profiles. The Fourier modes, used in previous sections, also form an orthonormal basis. Projection onto the Fourier modes corresponds to a spatial Fourier transform.

The linear stability analysis of the nonlasing solution follows exactly the same method as in section 3.2 ; we obtain the threshold for each family of modes

$$r = 1 + \left(\frac{4a \tan^{-1} \gamma_c (2p + |m| + 1) - \Delta}{\sigma + 1} \right)^2$$

and the associated frequency

$$\Omega = \left(\frac{4a \tan^{-1} \gamma_c (2p + |m| + 1) + \sigma \Delta}{\sigma + 1} \right).$$

We plot this threshold as a function of the mode family $(2p + |m| + 1)$ in figure 4.24. Compare these expressions with those based on the Fourier modes (3.4) and (3.5).

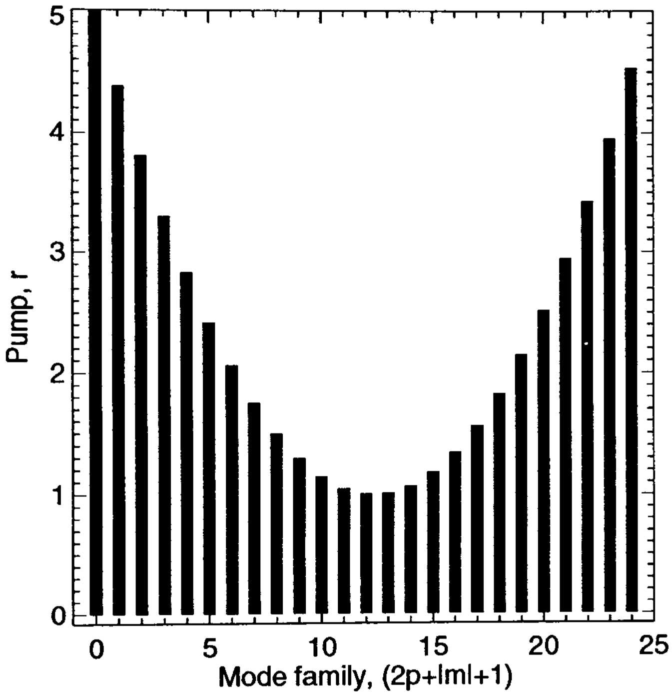

Figure 4.24: The threshold for instability of the nonlasing state to each degenerate mode family characterised by $(2p + |m| + 1)$.

For the case of plane mirrors we saw that all of the degenerate modes with $|\mathbf{k}| = k_c$ showed the lowest threshold for instability. For the curved mirror case, modes with $(2p + |m| + 1)$ closest to the quantity

$$\frac{\Delta}{4a \tan^{-1} \gamma_c}$$

have the lowest thresholds. Just as there was a ring of unstable modes in the flat mirrors case, the linear stability analysis here predicts a degenerate set of unstable Gauss-Laguerre modes. We notice that as $\gamma_c \to 0$, as the mirrors become flat, families of modes with $2p + |m| + 1$ equal to some very large number become excited and, since each family contains $N = 2p+|m|+1$ modes, a large number of Gauss-Laguerre modes are needed to describe the threshold.

Nonlinear analysis

To go any further in the analysis of the curved mirror case, we must derive amplitude equations for these active modes, describing their nonlinear competition. The procedure is basically the same as for the Fourier modes. At first order, the linear problem, we assign an amplitude to each mode in the active set, $\mathcal{A}$, and assume that these amplitudes are functions only of 'slow time'. Following the procedure through we obtain a solvability condition at third order

$$(\sigma + 1)\frac{da_{pm}}{dt} = \sigma(r - r_c)a_{pm} - \frac{\sigma}{b}\left\langle \sum_{(i,j)\in\mathcal{A}} a_{ij}A_{ij} \left| \sum_{(k,l)\in\mathcal{A}} a_{kl}A_{kl}\right|^2 \middle| A^*_{pm}\right\rangle$$

where a_{pm} is the amplitude of the mode $(p,m) \in \mathcal{A}$,

$$\langle X|Y^*\rangle = \int_0^{2\pi} d\phi \int_0^{\infty} \rho d\rho \; XY^*$$

and r_c is the threshold value for the family of modes in $\mathcal{A}$. Thus, we have a set of N coupled amplitude equations. Close to threshold, these equations are identical to those obtained by a simple modal expansion of the laser equations[2].

For two main reasons, these are not so useful as the ones we derived in section 3.4. Firstly, when N is large – that is when γ_c is small – we must consider a very large number of equations. Secondly, the nonlinear terms in the equations involve summing over modes, taking a modulus squared and re-projecting back onto modes again. Such a process is not simple for Gauss-Laguerre modes and so, in all but the simplest cases, the amplitude equations give little physical insight into the mode competitions. For these reasons, in this section we will abandon the use of these amplitude equations and follow an approach similar to that used for reflecting boundries and for gain guiding.

4.4.1 One Transverse Dimension

We consider first the simplifying case of one transverse dimension. The relevant equations therefore have the terms involving ρ replaced by ones involving x

$$\begin{aligned} \frac{\partial e}{\partial t} &= ia\frac{\tan^{-1}\gamma_c}{\gamma_c}\left[\frac{\partial^2}{\partial x^2} - 4\gamma_c^2 x^2\right] e - \sigma e + \sigma p, & (4.7)\\ \frac{\partial p}{\partial t} &= re - (1+i\Delta)p - ne, & (4.8)\\ \frac{\partial n}{\partial t} &= -bn + \frac{1}{2}(ep^* + e^* p) & (4.9) \end{aligned}$$

and the corresponding eigenfunctions of the spatially varying part, the empty cavity modes, are not of Gauss-Laguerre type but are *Gauss-Hermite* modes

$$A_n = \frac{\gamma_c^{1/4}}{\sqrt{2^{n-1} n! \sqrt{2\pi}}}\, H_n\left(\sqrt{2\gamma_c}x\right) e^{-\gamma_c x^2},$$

characterised by their mode index, n ; the corresponding eigenvalues are

$$-2\gamma_c(2n+1).$$

Note that in one transverse dimension, only one mode is excited at threshold – there is no degeneracy in the expression for the eigenvalue.

We now consider numerical simulations of the one transverse dimension equations above. The results are shown in figure 4.25. This is a rather busy figure and requires some explanation. The column on the left, marked *(a)*, shows the results of a simulation with curved mirrors run very close to threshold – the pump $r = 1.05$. The modulus of the electric field is plotted as a function of the transverse coordinate in the top diagram. In the middle row, we have extracted the amplitudes of the

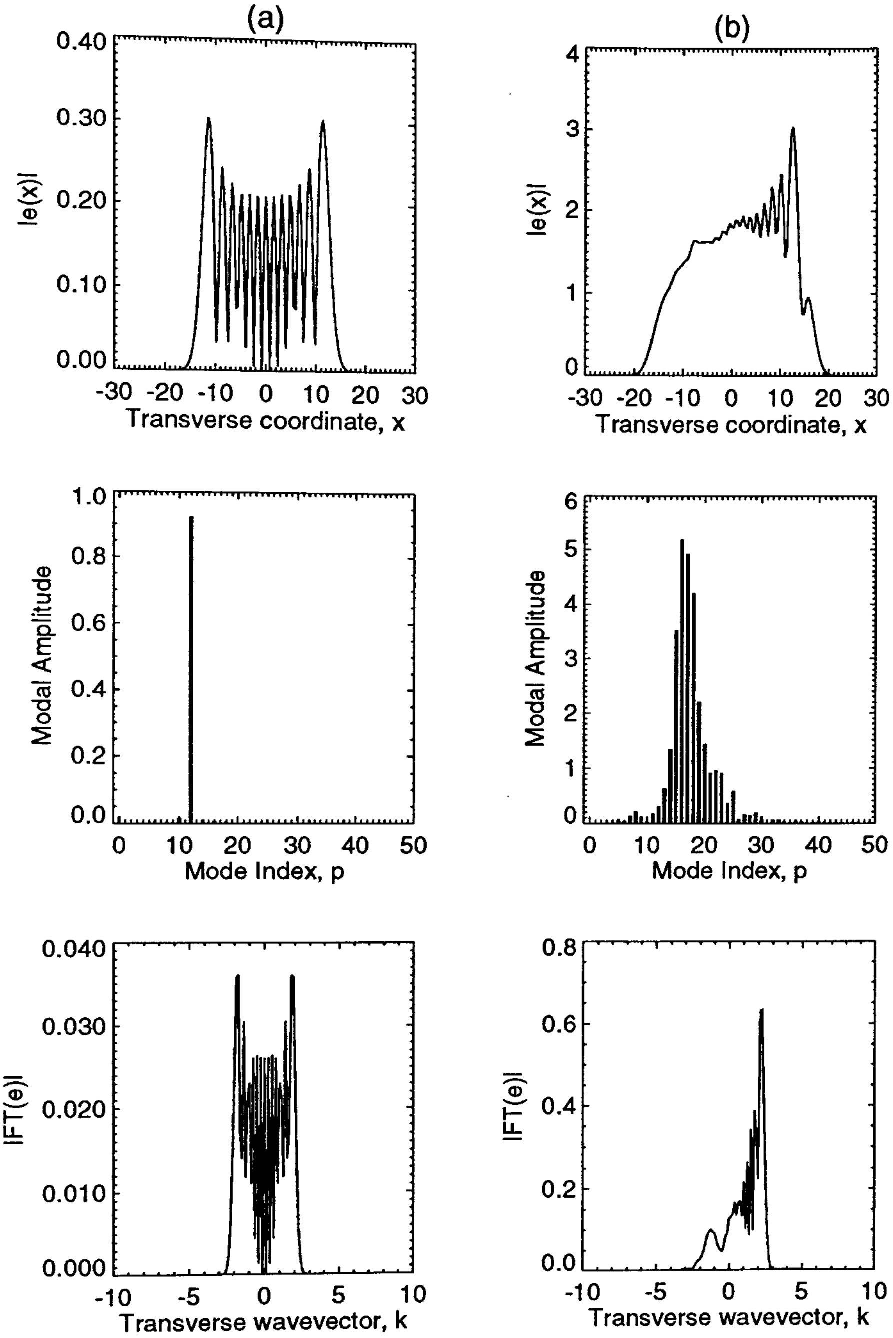

Figure 4.25: Results of two numerical simulations showing output profiles of Gauss-Hermite character and of travelling wave character. (a) is for $r = 1.05$ *and (b) is for* $r = 5.0$. *Other parameters are* $a = 1$, $b = 1$, $\Delta = 4$, $\sigma = 1$, $\gamma_c = 0.08$.

Gauss-Hermite modes making up the profile. Just as expected, the pattern consists almost exclusively of one Gauss-Hermite mode. In the bottom row, we plot the spatial Fourier transform of the output profile. The Fourier transform of a Gauss-Hermite mode is just a Gauss-Hermite mode[5] and so has energy in many Fourier modes.

The column on the right, marked *(b)*, shows essentially the opposite behaviour. It is for a value of the pump $r = 5$ and so, by analogy with the other forms of transverse confinement we have studied, we might expect to see an output of travelling wave nature. This is indeed the case. The modulus of the field at the top shows a striking resemblence to those shown in figures 4.1 and 4.21. Such an output profile is composed of a large number of Gauss-Hermite modes but most of the energy in Fourier space is collected near $k = \pm k_c$ – a description in Fourier space is more sensible. Notice that the output profile shows a distinct source and sink. In fact, for these parameter values, the source is unstable and produces the 'blips' we have seen already.

Transition from Gauss-Hermite modes to TW

In the previous sections we have found similar behaviour: there is some threshold value of the pump parameterm $r = r_t$, at which there is a transition from symmetric to asymmetric output. We now attempt to find this threshold, r_t, for the case of curved mirrors. To help in this, we again define the asymmetry parameter

$$A = \left| \int_0^{L/2} |e(x)| dx - \int_{L/2}^{L} |e(x)| dx \right| .$$

Just as we did in section 4.2.1 we should look at the asymmetry parameter as a function of time for the two simulations shown in figure 4.25. These plots are shown in figure 4.26. As expected, below the threshold for transition to travelling wave behaviour, the asymmetry parameter tends to zero ; above the threshold, A is non-zero. Due to the instability of the source it shows 'noisy' fluctuations in time.

---

[5] *Exactly the reason why they are so useful in describing cavity modes!*

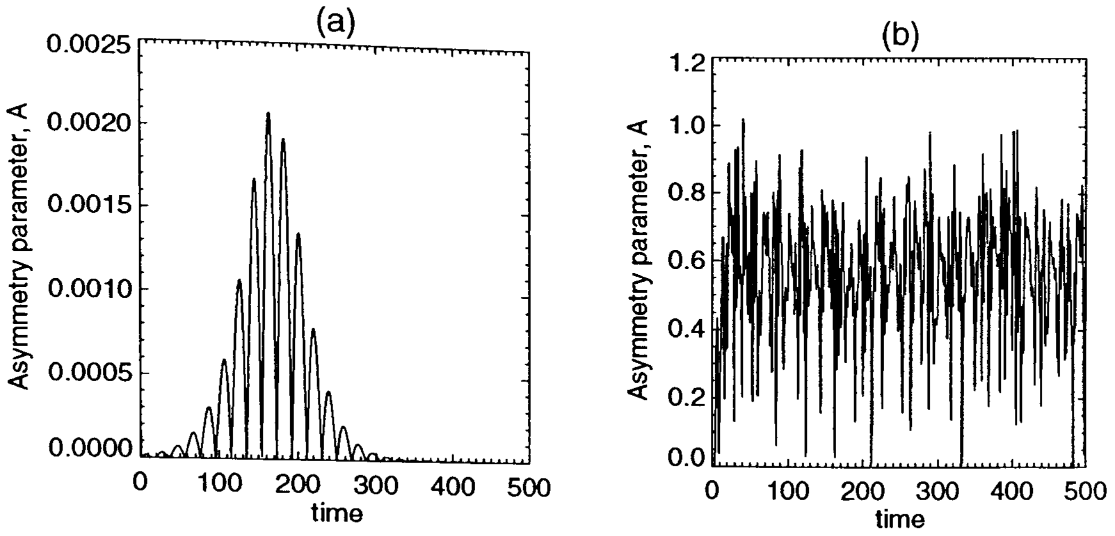

Figure 4.26: The asymmetry parameter, A, as a function of time for the two simulations shown in figure 4.25.

Mirroring the approach used to obtain figure 4.8, we run a number of simulations and plot the resulting asymmetry parameter as a function of the pump. The results are shown in figure 4.27. For this value of γ_c and for these system parameters the transition from symmetric to asymmetric output takes place at $r = r_t = 1.31 \pm 0.01$.

Given that we can find r_t for any set of system parameters we go on to plot, in figure 4.28, the value of r_t as a function of γ_c. The curve is just as we would expect. For small γ_c, that is for mirrors nearly flat, the transition to travelling wave type behaviour occurs for small values of the pump. As the mirrors are made more and more curved, that is γ_c is increased, the threshold for this transition is raised.

4.4.2 Two Transverse Dimensions

In two transverse dimensions we expect to see similar phenomena to those observed in one dimension. We will look for transitions from profiles involving only a few Gauss-Laguerre modes to those of a travelling wave nature. Figure 4.29 shows the results of two numerical simulations, one for a value of the pump below the transition threshold and one above it.

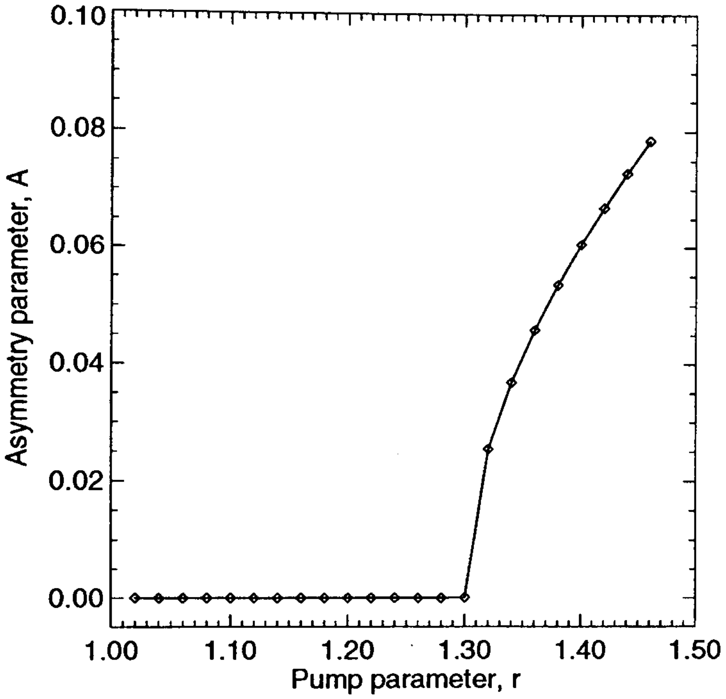

Figure 4.27: The asymmetry parameter, A*, as a function of the pump parameter,* r*. the transition between symmetric and asymmetric output occurs for* $r = r_t = 1.31 \pm 0.01$*. Other parameters are the same as in figure 4.25.*

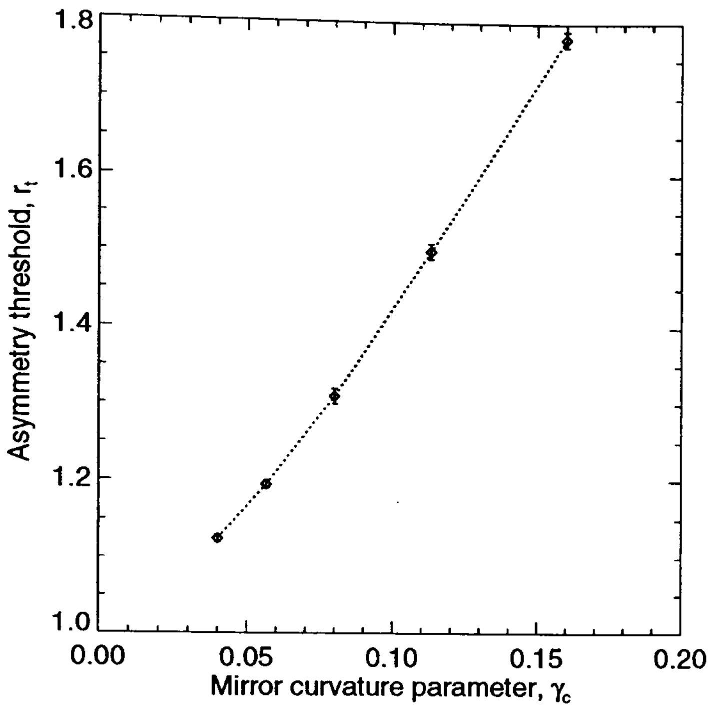

Figure 4.28: The threshold for the transition from a symmetric to an asymmetric output profile, r_t, as a function of the mirror curvature parameter, γ_c.

The column on the left of the figure shows the results of the simulation for $r = 1.05$. In the first row we have plotted the modulus of the electric field as a function of the transverse coordinates and in the second row we have plotted its real part. The profile is stationary in time and can be expressed as a linear combination of few Gauss-Laguerre modes. This is quantified in the third row, where we have plotted the amplitudes of the modes which make up the profile. To represent the amplitude of the mode (p, m) we have plotted a black 'blob' at position (p, m), the size of the blob being proportional to the amplitude. The blobs show that only modes in the family $(2p + |m| + 1) = 12$ have a reasonable amplitude. This is exactly the family of modes predicted, by the linear analysis, to have the lowest threshold. In the bottom row we have plotted the spatial Fourier transform of the output profile. It shows that there are a large number of Fourier modes which have finite energy.

The column on the right of figure 4.29 shows the results for the simulation with pump, $r = 5$. The modulus of the field shows a bright spot in the centre with structure all

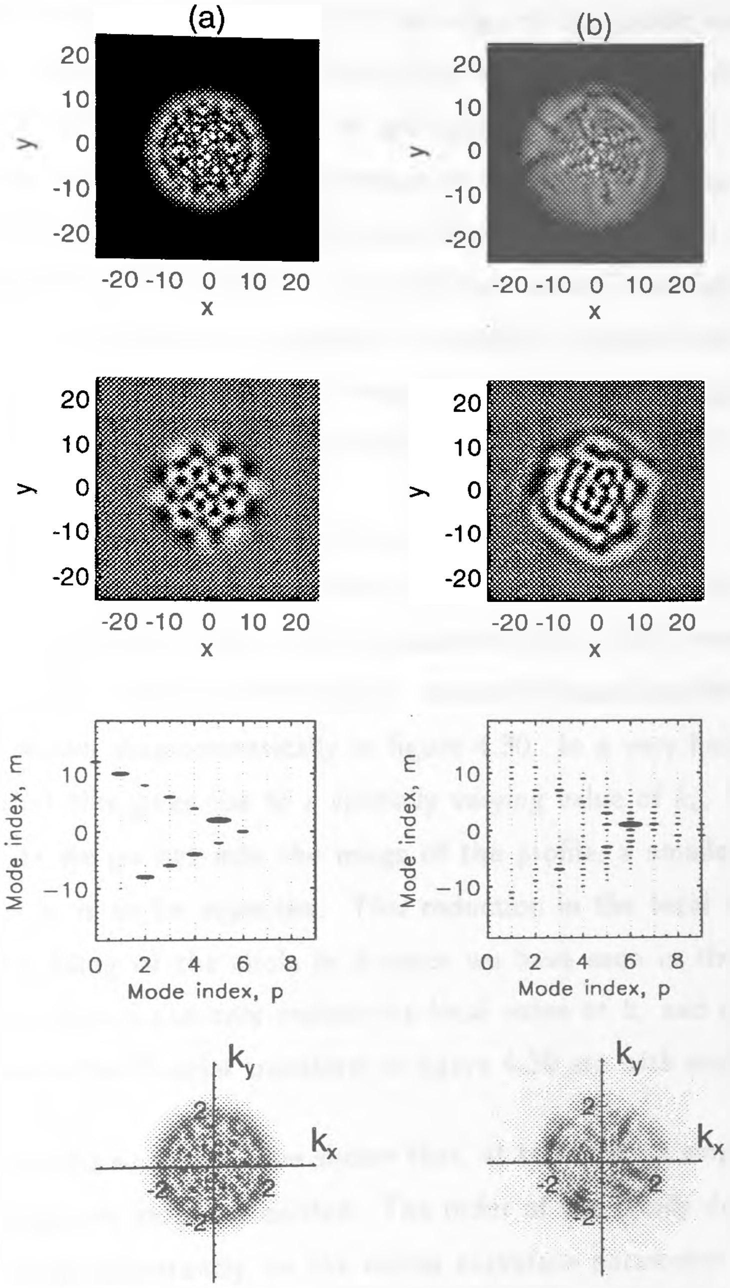

Figure 4.29: The results of two numerical simulations. (a) is for $r = 1.05$ *and (b) is for* $r = 5$*. Other parameters are the same as in figure 4.25. See the text for details.*

around roughly forming rings. The real part shows the existence of stripes, heralding the appearance of travelling waves. The profile is dynamic and appears to be made up of waves which are born at a source on the edge of the profile and propagate inwards towards a sink at the centre. Note that this direction of propagation is exactly the opposite of what is expected for gain guiding. The sink at the centre of the profile appears as a complicated interference of waves and the source round the edge nucleates defects in the way we have described already. All of this goes to make up a very complicated profile indeed! The projection onto Gauss-Laguerre modes shows that a very large number are required to adequately represent the profile. The Fourier transform, however, shows that a large proportion of the energy is in modes inside the circle $|\mathbf{k}| = k_c = 2$ with a few peaks close to the circle itself.

This is a little strange since, when travelling waves are dominating a pattern, we expect the energy to be localised in modes close to the critical circle, not filling it. How can this be explained? The term in equations (4.4) – (4.5) representing the curvature of the mirrors, the one multiplying ρ^2, enters the equations like the spatially varying detuning shown diagrammatically in figure 4.30. In a very handwaving way we can imagine that this gives rise to a spatially varying value of k_c. We see, from figure 4.30, that as we go out into the wings of the profile, a smaller and smaller value of the *local* k_c is to be expected. This reduction in the local value of k_c is responsible for the filling of the circle in k-space we have seen in the simulations. Note that concave mirrors can only *reduce* the local value of k_c and so the highest wavevectors we see in the Fourier transform in figure 4.29 are with modulus k_c.

Summarising the results so far we have shown that, at threshold, a single degenerate family of Gauss-Laguerre modes is excited. The order of the family depends on the parameters and, most importantly, on the mirror curvature parameter, γ_c. If this is very small (nearly flat mirrors) then a family of high order Gauss-Laguerre modes is excited. No matter how small we make $\gamma_c \neq 0$, if we go sufficiently close to threshold then only one family is excited and no travelling waves can be observed ; in this picture, the limit $\gamma_c \to 0$ is singular. However, if we allow the pump to be well above threshold – the meaning of 'well' being determined by the value of γ_c – we can regain a travelling wave description.

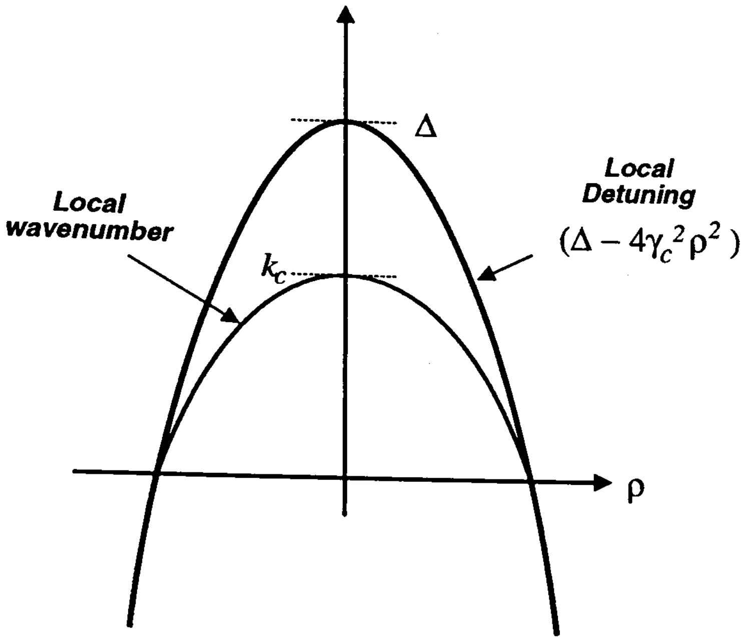

Figure 4.30: A diagrammatic representation of the 'equivalent' spatially dependent detuning, and hence most unstable wavenumber, in a cavity with curved mirrors.

We now go on to look in more detail at the profiles obtained near threshold and far from threshold.

Close to threshold

Figure 4.31 shows the results of three numerical simulations all for values of the pump, r, reasonably close to threshold. On the top row we have plotted the modulus of the electric field and on the bottom its real part. The simulation *(a)* is for $r = 1.05$ and ,as we have seen already, this profile is static and is simply a superposition of Gauss-Laguerre modes in a single family.

Simulation *(b)*, for $r = 1.5$, appears to be symmetric and static but, not immediately obvious from these pictures, is that it is already showing signs of the 'far from threshold' patterns. To make this clearer we have produced figure 4.32. It shows a series of time snapshots of the real part of the field in simulation *(b)*. The real part of the field alternates between a set of stripes orientated in a 'target' pattern and in a 'spokes' pattern. This is the cylindrically symmetric equivalent of the flipping of

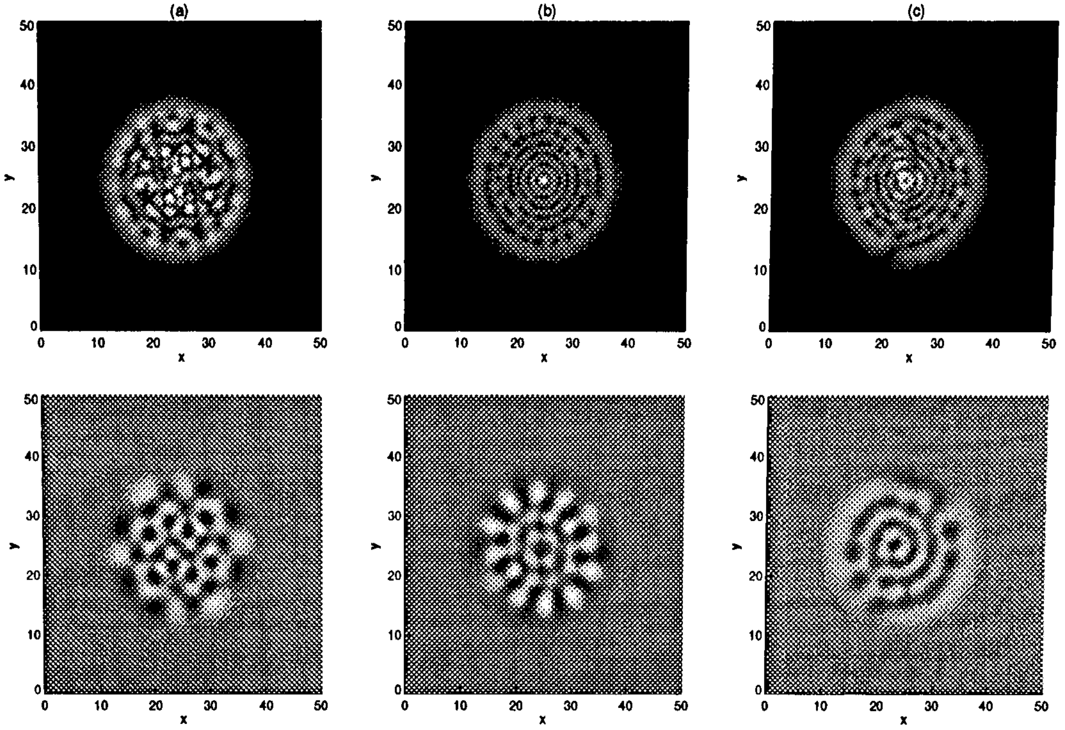

Figure 4.31: Three numerical simulations, all for values of the pump reasonably close to threshold. (a) is for $r = 1.05$*, (b) is for* $r = 1.5$ *and (c) is for* $r = 1.8$*. Other parameters are the same as in figure 4.25. The top row shows the modulus of the field profile, the bottom row its real part.*

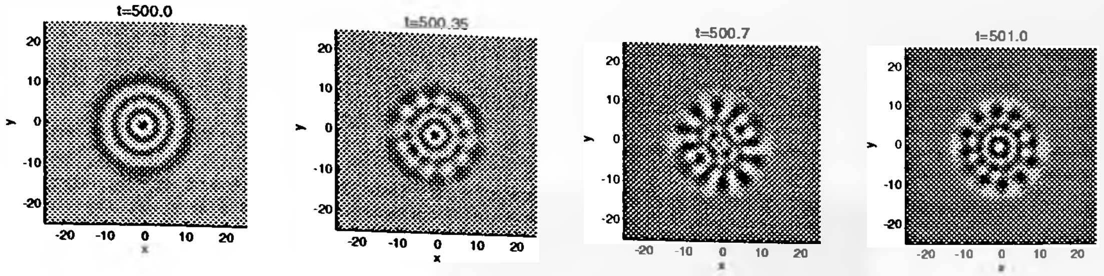

Figure 4.32: A series of snapshots of the real part of the field in simulation (b) of figure 4.31. The real part shows an alternation between a 'target' pattern and a set of 'spokes'.

the rhomboidal pettern in section 3.7 and the squares we say close to threshold for the reflecting boundaries in section 4.2.2.

Simulation *(c)* in figure 4.31 shows similar features to those in simulation *(b)* but instead the real part showing a target pattern as part of its flipping, here it shows a spiral. This can be viewed as a defect of the pattern seen in *(b)*. The entire pattern rotates in time, the direction of rotation being determined by the topological charge of the defect at the centre.

The existence of such patterns near the threshold for transition from a boundary dominated régime to one of travelling waves shows that this transition is much more difficult to quantify in 2D than in 1D.

Far from threshold

We have seen in figure 4.29 that far from threshold we can obtain output showing travelling waves generated at the boundary and propagating towards the centre. In this sense, these far from threshold patterns still retain some cylindrical symmetry. Is this symmetry ever broken, very far from threshold or when γ_c is very small? It appears not. Figure 4.33 shows the results of a simulation for $r = 10$ and $\gamma_c = 0.032$. A number of features in these images are worthy of note. Firstly we see that, even for such a large domain, the boundary is still the source of travelling waves which propagate towards the centre. The sink at the centre appears as a complicated interference between such waves. The strip patterns in the real part show a number

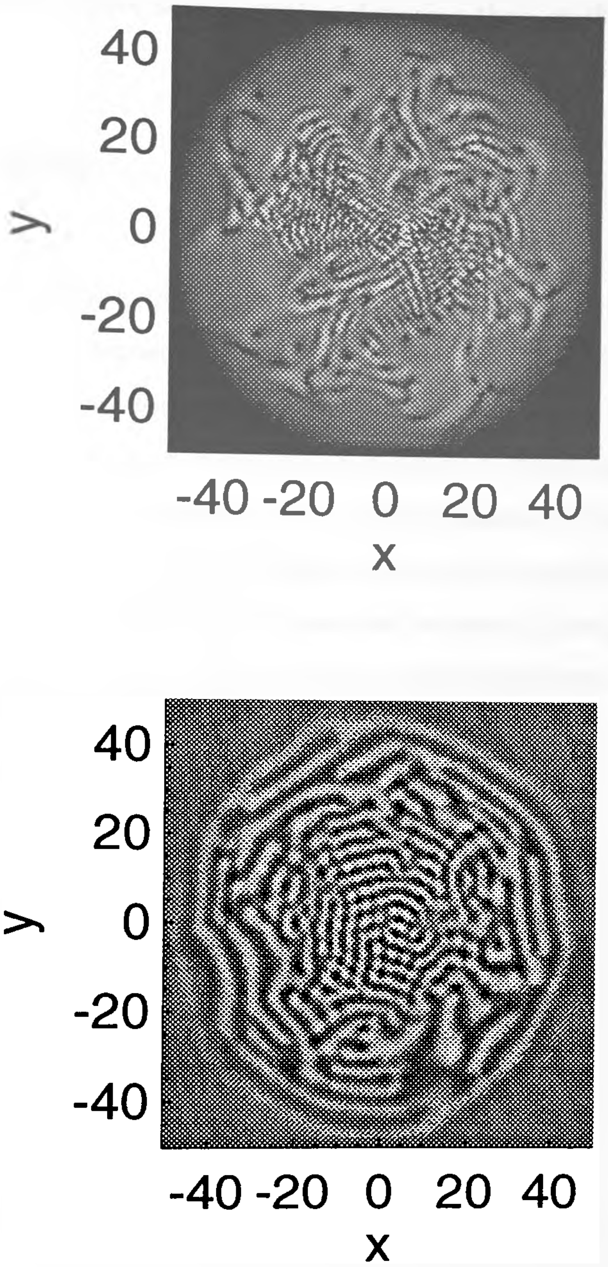

Figure 4.33: The results of a simulation with $r = 10$ *and* $\gamma_c = 0.032$. *Other parameters are the same as in figure 4.25. The image at the top shows the modulus of the electric field and the image at the bottom shows its real part.*

of dislocations, corresponding to optical vortices which have been nucleated at the source. The real part shows very clearly that, near the edge of the domain, the waves have a smaller wavevector (longer wavelength). This can be explained, as above, by saying that the local field there sees a smaller detuning than at the centre.

4.5 Conclusions

In this chapter we have shown that the travelling waves found in infinitely extended laser models are affected by transverse boundaries. The strength of the effects depend on the size of the transverse domain and critically on the pump parameter. For a pump close to threshold, boundary dominated behaviour is always observed but, away from threshold, travelling waves describe the patterns better. In such a régime, we have also identified the source and sink defects as being a useful in the description of the patterns. We have quantified the transition between these two behaviours in one transverse dimension and have shown that, in two dimensions, such a transition is more complicated.

Chapter 5

Conclusions

In this thesis we set out to bridge the gap between the two types of theories of transverse effects in lasers – those based on modes and those dealing with an infinitely extended transverse domain. We have shown that the plethora of complicated behaviours observed between these two limits can, in most cases, be elegantly explained in terms of basic pattern 'building blocks': *travelling waves*, *rhomboids*, and *boundary dominated modes*.

We have shown something of the nature of each of these building blocks: we characterised the gain guided modes of a plane-parallel mirrored microchip laser and gave a brief introduction to empty cavity modes ; we showed the existence of travelling wave and 'rhomboidal' solutions to the laser equations and studied their stability and defects. Furthermore, through the derivation of amplitude equations we have made analogies between laser physics and other branches of nonlinear science.

In the sections on boundary effects we have shown how these building blocks fit together in various situations to give explanations for the highly complicated laser patterns observed. We showed the existence of transitions between régimes where one or more of these building blocks are more appropriate than others.

Appendix A

Derivation of the Maxwell-Bloch equations

The Maxwell-Bloch equations are the basic building blocks for a large portion of all work in dynamical nonlinear optics today. From them can be derived a plethora of related equations. Applications range widely from the description of very short pulses in optical fibres to laser equations to light interaction with nonlinear media and many more.

They are derived based on the fields of electrodynamics and quantum mechanics and they describe the interaction of a light field with an ensemble of atoms. The equations are *semi-classical* in that the electric field is described using Maxwell's equations – purely classically – and the atomic medium using quantum mechanics.

In this section we will derive the Maxwell-Bloch equations for the interaction of a single mode of a cavity with a two-level atom. Many good text books cover the derivation of these equations. This section is included here for completeness.

The approach is outlined in figure A.1. Maxwell's equations are used to derive an equation for the propagation of the electric field given some material polarisation. A quantum-mechanical technique is used to model the effects of this electric field on an atom and a process of statistical averaging is used to infer the macroscopic material polarisation induced by the field. This polarisation is the one used in the field equation, completing the loop and assuring a self-consistent set of equations governing the interaction.

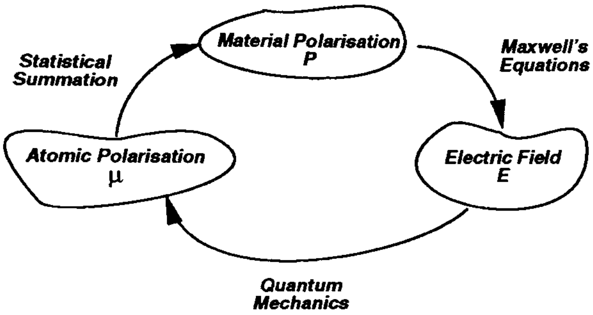

Figure A.1: An outline of the procedure used in the derivation of the Maxwell-Bloch equations

A.1 Field equation

We start with Maxwell's equations for a non-magnetic medium with no free charges,

$$\nabla \times \mathbf{E} = -\frac{\partial \mathbf{B}}{\partial t} \tag{A.1}$$

$$\nabla \times \mathbf{H} = \frac{\partial \mathbf{D}}{\partial t} \tag{A.2}$$

$$\nabla . \mathbf{D} = 0 \tag{A.3}$$

$$\nabla . \mathbf{B} = 0 \ , \tag{A.4}$$

and the constitutive relations

$$\mathbf{D} = \varepsilon_o \mathbf{E} + \mathbf{P} \tag{A.5}$$

$$\mathbf{B} = \mu_o \mathbf{H}. \tag{A.6}$$

The constants of free space, ε_o and μ_o, are, respectively, the electric and magnetic susceptibilities. Taking the curl of (A.1) and substituting (A.2) and (A.6) leads to

$$\nabla \times \nabla \times \mathbf{E} \;=\; -\mu_o \frac{\partial^2 \mathbf{D}}{\partial t^2}.$$

and a well known vector operator identity lets us expand the left hand side yielding

$$\nabla^2 \mathbf{E} - \nabla(\nabla . \mathbf{E}) = \mu_o \frac{\partial^2 \mathbf{D}}{\partial t^2}. \tag{A.7}$$

We now consider the magnitude of the second term on the left hand side of this equation, $\nabla(\nabla . \mathbf{E})$. When light propagates through vacuum or indeed through a homogeneous linear medium the electric displacement vector $\mathbf{D}$ is linearly related to the electric field through the relation

$$\mathbf{D} = \varepsilon \mathbf{E}. \tag{A.8}$$

Given this, it is obvious that the Maxwell equation (A.3) implies that $\nabla . \mathbf{E} = 0$ and so the 'problem' term in (A.7) is identically zero. This is, however, not the case if we consider nonlinear or inhomogeneous media. The 'constant' of proportionality relating $\mathbf{E}$ and $\mathbf{D}$ in equation (A.8) may vary in space or in time or with the electric field itself. Using equations (A.3) and (A.8) lets us write

$$\varepsilon \nabla . \mathbf{E} + \mathbf{E} . \nabla \varepsilon = 0$$

and therefore

$$\nabla . \mathbf{E} = -\frac{\nabla \varepsilon}{\varepsilon} . \mathbf{E} = -\nabla(\ln \varepsilon) . \mathbf{E}$$

Our plan now is to hope that the susceptibility, ε, varies only very slowly in space - that is on a scale many optical wavelengths long - making the gradient of ε small and hence the whole term small. The consolation is that even if ε does change a little more than we'd like, the effect on our problem term is through the logarithm, reducing the effect. We already mentioned that the spatial variations of ε may be due to inhomogeneities on the medium or to nonlinearities. In inhomogeneous media, such as an optical fibres, the refractive index does change slowly on the scale of the wavelength. In nonlinear media, the changes in electric field, $\mathbf{E}$ can affect ε and so we must require that the electric field envelope changes only slowly in space. This boils down to the paraxial approximation. Some optical systems in which the paraxial approximation is invalidated have recently been studied, but work in this field is very limited and complicated and so in all that follows we will consider only *paraxial optics* and we will approximate $\nabla \cdot \mathbf{E} \approx 0$. The details of this approximation have been studied by Lax *et al.*[49]. The wave equation (A.7) now becomes

$$\nabla^2 \mathbf{E} - \mu_o \frac{\partial^2 \mathbf{D}}{\partial t^2} = 0.$$

We now introduce the polarisation into the wave equation through the constitutive relation (A.5) giving

$$\nabla^2 \mathbf{E} - \frac{1}{c^2}\frac{\partial^2 \mathbf{E}}{\partial t^2} = \mu_o \frac{\partial^2 \mathbf{P}}{\partial t^2},$$

where we have defined the speed of light in vacuum, $c = 1/\sqrt{\mu_o \varepsilon_o}$. Until now, we have considered the full vector nature of the electric field and polarisation. In most experimental setups there is some form of polarisation selection ; typical in lasers is the use of Brewster windows to select a single, linear field polarisation. So, in a large subset of optics problems the equations are overly complicated by considering the vector nature of the fields. From now on, we'll consider only linearly polarised fields and so we can drop the vector notation:

$$\nabla^2 E - \frac{1}{c^2}\frac{\partial^2 E}{\partial t^2} = \mu_o \frac{\partial^2 P}{\partial t^2}. \tag{A.9}$$

This is the so-called *scalar wave equation*. It is a partial differential equation for the evolution of the electric field, E, under the influence of the medium's polarisation, P. Both E and P are real quantities in this description. In general, this electric field will in turn affect the medium it propagates through changing, in some way, its polarisation. By writing an equation describing the medium we can quantify these changes to the polarisation and so obtain a self-consistent model for the entire interaction and propagation of the light.

Let us consider a simple example such as propagation of a weak light field through glass. We can assume that, away from any material resonances, the incident field will induce a polarisation of the medium which is linearly related to the field itself - the definition of a linear medium. The constant of proportionality is defined in terms of the *refractive index*, n, of the medium

$$P = \varepsilon_o(n^2 - 1)E. \tag{A.10}$$

The refractive index is a dimensionless constant for a given medium and is defined such that $n \geq 1$, with $n = 1$ for a vacuum. The refractive index of glass is $n \approx 1.5$. Substituting equation (A.10) into the wave equation (A.9) gives

$$\nabla^2 E - \frac{n^2}{c^2}\frac{\partial^2 E}{\partial t^2} = 0. \tag{A.11}$$

In general, we would have to write

$$\nabla^2 E = \left(\frac{\partial^2}{\partial x^2} + \frac{\partial^2}{\partial y^2} + \frac{\partial^2}{\partial z^2}\right) E$$

since E can vary in all three space dimensions but, at this point we will consider E to be propagating along the z–direction and to be independent of the transverse coordinates, (x, y). This is called the *plane wave limit* and we will relax it again later. The wave equation now reads

$$\frac{\partial^2 E}{\partial z^2} - \frac{n^2}{c^2}\frac{\partial^2 E}{\partial t^2} = 0$$

and we can find simple solutions in the form of travelling waves

$$E \propto \exp\left(ikz - i\omega_c t\right) + c.c.$$

where k and ω_c are related through the *dispersion relation*

$$\omega_c = \pm k\frac{c}{n}, \tag{A.12}$$

and *c.c.* denotes the complex conjugate of the preceding expression ; the velocity of propagation is c/n and the plus and minus signs indicate that both forward and backward travelling waves are possible.

Let's now go back to the wave equation and consider some simplifications we might make in the light of this new-found travelling wave solution. We consider writing both the electric field and the polarisation as a product the *fast* travelling wave solution[1] and *slow* amplitudes, $\bar{F}$ and $\bar{P}$

$$\begin{aligned} E &= \bar{F}\exp(ikz - i\omega_c t) + c.c. && \text{(A.13)} \\ P &= \bar{P}\exp(ikz - i\omega_c t) + c.c. \ . && \text{(A.14)} \end{aligned}$$

and we use the dispersion relation we found already, (A.12). Note that we have called the optical frequency ω_c since we will eventually consider the field to be propagating in a cavity. We want to insert these into the wave equation (A.9) and so we will need

$$\begin{aligned} \frac{\partial^2 E}{\partial z^2} &= \left(\frac{\partial^2 \bar{F}}{\partial z^2} + 2ik\frac{\partial \bar{F}}{\partial z} - k^2\bar{F}\right)\exp(ikz - i\omega_c t) + c.c. && \text{(A.15)} \\ \frac{\partial^2 E}{\partial t^2} &= \left(\frac{\partial^2 \bar{F}}{\partial t^2} - 2i\omega_c\frac{\partial \bar{F}}{\partial t} - \omega_c^2\bar{F}\right)\exp(ikz - i\omega_c t) + c.c. && \text{(A.16)} \\ \frac{\partial^2 P}{\partial t^2} &= \left(\frac{\partial^2 \bar{P}}{\partial t^2} - 2i\omega_c\frac{\partial \bar{P}}{\partial t} - \omega_c^2\bar{P}\right)\exp(ikz - i\omega_c t) + c.c. \ . && \text{(A.17)} \end{aligned}$$

where we have defined the *transverse laplacian*

$$\nabla_T^2 = \frac{\partial^2}{\partial x^2} + \frac{\partial^2}{\partial y^2}.$$

We now use the fact that the amplitudes $\bar{F}$ and $\bar{P}$ vary much more slowly that the travelling wave characterised by ω_c in time and k in space. Given this we can see that some terms in these expressions are much larger than others, for example

$$k^2\bar{F} \gg 2ik\frac{\partial \bar{F}}{\partial z} \gg \frac{\partial^2 \bar{F}}{\partial z^2}, \tag{A.18}$$

and similarly for the time derivatives. This is known as the *slowly varying envelope approximation* and it holds true if the field amplitudes are indeed slow with respect

---

[1] *The travelling wave solution is considered fast in time and space because it oscillates at optical frequencies and it changes on the scale of a wavelength*

to the underlying optical fields. Situations in which this breaks down includes the formation of very short pulses in which the field envelopes become comparable to the period of oscillation of the optical field ; in *non-paraxial optics* the fields can be very tightly focussed and diffraction of such fields can lead to large changes in fields over very short propagation distances. We will steer clear of these areas and in all the work reported in this thesis, the inequalities (A.18) will hold good - with a lot to spare in fact! With the aid of these inequalities we can entirely eliminate the second order derivatives from equations (A.15) – (A.17). Substituting all these expressions into the wave equation, (A.9), we obtain the field equation part of the Maxwell-Bloch equations,

$$\nabla_T^2 \bar{F} + 2ik\frac{\partial \bar{F}}{\partial z} + \frac{2ik}{c}\frac{\partial \bar{F}}{\partial t} = -\mu_o \omega_c^2 \bar{P}. \tag{A.19}$$

A.2 Equations for the medium

We have now completed the part of the derivation concerned with the propagation of the electric field through a polarised medium. To obtain a self-consistent set of equations for the entire medium–field interaction we need to describe how the polarisation of the medium is affected by the propagating field. This is modelled by considering the interaction of the classical field, E, with an ensemble of two level, quantum mechanical, atoms.

The time dependent Schrödinger equation for the atomic state $|\psi\rangle$ is as follows

$$i\hbar\frac{\partial}{\partial t}|\psi\rangle = (\mathcal{H}_o + \mathcal{H}_I)|\psi\rangle \tag{A.20}$$

where $\mathcal{H}_o$ is the Hamiltonian of the unperturbed system ; $\mathcal{H}_I$ is the Hamiltonian describing the interaction of the two-level atom with an incident light field – we'll come back to this shortly ; $\hbar$ is Planck's constant. We are considering a two-level system, as in figure A.2, and so the atomic state will be some, perhaps time dependent,

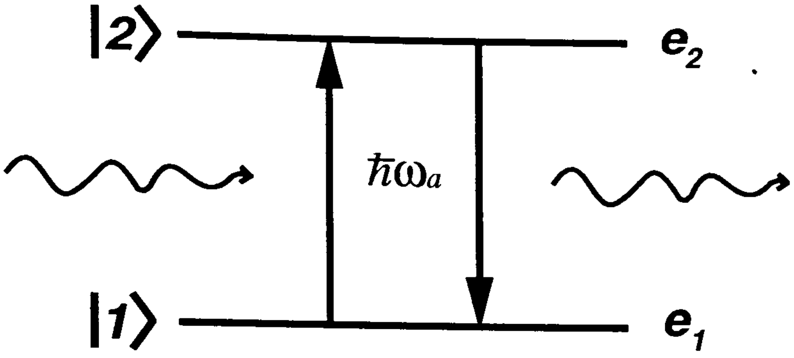

Figure A.2: A diagrammatic representation of a two-level atom under the influence of a perturbing electric field. The upper and lower states, $|1\rangle$ and $|2\rangle$ have energies e_1 and e_2 and the atomic transition frequency is $\omega_a = (e_2 - e_1)/\hbar$.

superposition of the lower and upper states, $|1\rangle$ and $|2\rangle$,

$$|\psi\rangle = a_1(t)|1\rangle + a_2(t)|2\rangle.$$

These states are eigenfunctions of the unperturbed Hamiltonian,

$$\begin{aligned} \mathcal{H}_o|1\rangle &= e_1|1\rangle \\ \mathcal{H}_o|2\rangle &= e_2|2\rangle, \end{aligned}$$

and are normalised so that

$$\langle 1|1\rangle = \langle 2|2\rangle = 1.$$

The probability amplitudes obey the relation $|a_1|^2 + |a_2|^2 = 1$, which is another way of saying that the atom must be in either the lower or the upper level.

Substituting these expressions into the Schrödinger equation and projecting onto the states $|1\rangle$ and $|2\rangle$ yields equations for the time dependence of the probability amplitudes

$$\begin{aligned} i\hbar\frac{\partial a_1}{\partial t} &= a_1 e_1 + a_1\langle 1|\mathcal{H}_I|1\rangle + a_2\langle 1|\mathcal{H}_I|2\rangle \\ i\hbar\frac{\partial a_2}{\partial t} &= a_2 e_2 + a_1\langle 2|\mathcal{H}_I|1\rangle + a_2\langle 2|\mathcal{H}_I|2\rangle. \end{aligned} \tag{A.21}$$

We now require to find a form for the interaction Hamiltonian, $\mathcal{H}_I$. We will assume that the atom can be represented as an electric dipole. Furthermore, atoms are typically of the size of the Bohr radius and the wavelength of light we will consider is many orders of magnitude larger than this, so the atom sees an electric field uniform in space. The potential energy of a dipole in such a vector field, $\mathbf{E}$ is given by

$$\mathcal{H}_I = -e\,\mathbf{d}.\mathbf{E},$$

where e is the charge on the electron and $\mathbf{d}$ is the average displacement of the electrons in the atom. It can be shown that other contributions to the interaction Hamiltonian, such as electric quadrupole and magnetic dipole interactions, are very small [50]. We require to find expressions for the matrix elements of the interaction Hamiltonian

$$\mu_{pq} = \langle p|\mathcal{H}_I|q\rangle$$

in equation (A.21), which involves performing the integrals implied by those elements. A simple symmetry argument will help us get round this problem. The interaction Hamiltonian has odd parity, since reflection through the atomic nucleus reverses the sign of $\mathbf{d}$. As a consequence, the matrix elements

$$\mu_{11} = \mu_{22} = 0.$$

Furthermore, provided the states $|1\rangle$ and $|2\rangle$ have opposite parity then the other two matrix elements will not vanish and we can write

$$\begin{aligned} \langle 1|\mathcal{H}_I|2\rangle &= \mu_{12} \\ \langle 2|\mathcal{H}_I|1\rangle &= \mu_{21} = \mu_{12}^*, \end{aligned}$$

where * represents the process of complex conjugation. It can be shown that by appropriate choice of the phases of the states $|1\rangle$ and $|2\rangle$ we can make the matrix elements real so that

$$\mu_{12} = \mu_{21}.$$

Substituting all these expressions into equations (A.21) yields the final equations for the probability amplitudes

$$\begin{aligned}
\frac{\partial a_1}{\partial t} &= -\frac{i}{\hbar}e_1a_1 + \frac{i}{\hbar}\mu_{12}Ea_2 &\quad (\text{A.22})\\
\frac{\partial a_2}{\partial t} &= -\frac{i}{\hbar}e_2a_2 + \frac{i}{\hbar}\mu_{12}Ea_1. &\quad (\text{A.23})
\end{aligned}$$

At this stage, we introduce the *density operator* formalism in which to describe the interaction of the field with the atom. The benefits of doing this are two-fold. The first is that the elements of the *density matrix* have clear physical interpretations as the atomic polarisation and the population inversion. The second is the ease by which the method produces expressions for the physical quantities which require some form of statistical summation – see, for example, Loudon's book[50].

The density operator is defined

$$\hat{\rho} = |\psi\rangle\langle\psi|$$

and for the case of the two-level atom, its matrix elements have the form

$$\rho = \begin{pmatrix} \rho_{11} & \rho_{12} \\ \rho_{21} & \rho_{22} \end{pmatrix} = \begin{pmatrix} a_1a_1^* & a_1a_2^* \\ a_2a_1^* & a_2a_2^* \end{pmatrix}.$$

The equations of motion for the density matrix elements can be found by using the definitions above and the equations for the probability amplitudes (A.22) and (A.23) to obtain

$$\frac{\partial \rho_{11}}{\partial t} = i\mu_{12}E\left(\rho_{21} - \rho_{12}\right)/\hbar \quad (\text{A.24})$$

$$\frac{\partial \rho_{12}}{\partial t} = i\omega_a\rho_{12} + i\mu_{12}E\left(\rho_{22} - \rho_{11}\right)/\hbar \quad (\text{A.25})$$

The equations for the other two elements can be derived using these two and the expressions $\rho_{21} = \rho_{12}^*$ and $\rho_{11} + \rho_{22} = 1$.

Closer inspection of equation (A.25) shows that it is the equation for a driven, undamped harmonic oscillator whose natural frequency is ω_a. It is now instructive to ask the question, how strong is the forcing? The ratio of the second term to the first is given, in terms of the *Rabi frequency*, $\omega_{rabi} = \mu_{12}E/\hbar$, by ω_{rabi}/ω_a. For almost all nonlinear optical systems, this ratio is very small indeed $(10^{-7} - 10^{-4})$ and so, given this, how will the oscillator ever gain in energy?

The answer lies through the process of resonant forcing. This can be imagined as like a child playing on a playground swing ; the child is the mass on the end of a harmonically oscillating pendulum. If the pendulum has no friction – not very likely in the playground but exactly the situation in equation (A.25) – then a gentle push from a friend, carefully timed to be once every period of the swing, can send the child soaring! In fact, provided friction is not too strong – if the local council oil the swing from time to time – the child can reach an appreciable height from only very gentle pushes. The same applies to equation (A.25). If the second term has contributions which are approximately resonant with ω_a, no matter how small, they can cause ρ_{12} to show *secular growth* – c.f. section 3.5.1. However, only resonant terms can do this. Just as pushing the swing at very irregular times is not likely to please the child, contributions to the second term with frequencies well away from resonance will not give energy to ρ_{12}.

In the search for such resonant terms, we express the electric field as a sum of positive and negative frequency parts, just as we did in the previous section,

$$E = \bar{F}\exp(ikz - i\omega_c t) + \bar{F}^*\exp(-ikz + i\omega_c t).$$

We insert this into the equation of motion for ρ_{12}, equation (A.25), to obtain

$$\frac{\partial\rho_{12}}{\partial t} - i\omega_a\rho_{12} = i\mu_{12}\left(\bar{F}\exp(ikz - i\omega_c t) + \bar{F}^*\exp(-ikz + i\omega_c t)(\rho_{22} - \rho_{11})\right)/\hbar.$$

We now look for terms on the right hand side which are resonant with the characteristic frequencies on the left. If ω_c is close to ω_a then the relevant contribution comes from the term involving $\bar{F}^*$. We assume that the contribution from the $\bar{F}$

term averages to give no net growth for ρ_{12}. This is known as the *rotating wave approximation*. Under this approximation the equations for the evolution of ρ_{12} and ρ_{21} become

$$\begin{aligned}\frac{\partial \rho_{12}}{\partial t} - i\omega_a \rho_{12} &= \frac{i\mu_{12}\bar{F}^*}{\hbar}\left(\rho_{22}-\rho_{11}\right)\exp\left(-ikz+i\omega_c t\right),\\ \frac{\partial \rho_{21}}{\partial t} + i\omega_a \rho_{21} &= \frac{-i\mu_{12}\bar{F}}{\hbar}\left(\rho_{22}-\rho_{11}\right)\exp\left(ikz-i\omega_c t\right).\end{aligned}$$

In order to couple these equations back to the field equation already derived, we need to have an expression for the macroscopic polarisation of an ensemble of such two-level atoms. We will define the polarisation in terms of the atomic density, N and we'll assume that there are a sufficiently large number of atoms in a given volume so that the field sees an average of all the dipole interactions. We therefore define the macroscopic polarisation in terms of the expectation value of the dipole elements

$$P = N\langle \mu \rangle.$$

In the density matrix formalism, this expectation value is computed from the expression

$$\langle \mu \rangle = \mathrm{Tr}(\rho\mu)$$

where $\mathrm{Tr}(A)$ represents the trace of the matrix A, and the equation for the macroscopic polarisation follows,

$$P = N\mu_{12}\left(\rho_{12}+\rho_{21}\right).$$

Recalling the definition for P we made in equation (A.14),

$$P = \bar{P}\exp\left(ikz-i\omega_c t\right) + \bar{P}^*\exp\left(-ikz+i\omega_c t\right) \tag{A.26}$$

allows us to equate these two expressions for P to give

$$N\mu_{12}\left(\rho_{12}+\rho_{21}\right) = \bar{P}\exp\left(ikz-i\omega_c t\right) + \bar{P}^*\exp\left(-ikz+i\omega_c t\right). \tag{A.27}$$

As we have seen already, ρ_{12} has a characteristic frequency of $+\omega_a$ and so it will be the density matrix element which contributes to the equation for $\bar{P}^*$. Correspondingly, ρ_{21} will be relevant for the $\bar{P}$ equation. If we now differentiate both sides of equation (A.27), use the equations of motion we have already derived for the density matrix elements and equate the relevant terms we obtain

$$\frac{\partial \bar{P}}{\partial t} = i(\omega_c - \omega_a)\bar{P} - \frac{iN\mu_{12}^2}{\hbar}\bar{F}\bar{D} \tag{A.28}$$

where we have defined the *population inversion* to be

$$\bar{D} = \rho_{22} - \rho_{11}. \tag{A.29}$$

Differentiating both sides of equation (A.29) and, again, inserting the equations of motion for the density matrix elements gives

$$\frac{\partial \bar{D}}{\partial t} = \frac{-2i}{N\hbar}\left[\bar{F}\,\bar{P}^* - \bar{F}^*\bar{P}\right]. \tag{A.30}$$

We now consider the simple stationary states of equation (A.30) in the absence of an applied electric field, $\bar{F} = 0$. They show that there can be no transitions in the absence of an electric field and the population is trapped where it is. It is well known that this is not the case and so several decay processes not contained in the semi-classical approach need to be included in a phenomenological way. We will consider the effects of spontaneous emission and of *elastic* and *inelastic* collisions between atoms. We can model these processes by introducing phenomenological decay terms into the polarisation and population inversion equations, (A.28) and (A.30),

$$\frac{\partial \bar{P}}{\partial t} = i(\omega_c - \omega_a)\bar{P} - \frac{iN\mu_{12}^2}{\hbar}\bar{F}\,\bar{D} - \gamma_\perp \bar{P}, \tag{A.31}$$

$$\frac{\partial \bar{D}}{\partial t} = \frac{-2i}{N\hbar}\left[\bar{F}\,\bar{P}^* - \bar{F}^*\bar{P}\right] - \gamma_{\|}(\bar{D} - \bar{D}_o). \tag{A.32}$$

Decay of the polarisation is due to processes such as spontaneous emission and collisions between atoms. We have assumed that its decay rate is $\gamma_\perp$. The population inversion decays due to spontaneous emission and only *inelastic* collisions between atoms ; it has an associated rate $\gamma_{\|}$. The value of D_o gives the equilibrium population inversion in the absence of any laser field ; its value is set by the strength of the pumping.

It should be noted that spontaneous decay and its associated rate are predicted in a fully quantum-mechanical model of the atom-field interaction, but the phenomenological approach in the semi-classical treatment gives identical results[50].

A.3 Maxwell-Bloch equations

We have now derived the Maxwell-Bloch equations. We re-write equations (A.19), (A.31) and (A.32) for clarity:

$$\begin{aligned}
\nabla_T^2 \bar{F} &+ 2ik\frac{\partial \bar{F}}{\partial z} + \frac{2ik}{c}\frac{\partial \bar{F}}{\partial t} = -\mu_o \omega_c^2 \bar{P}, \\
\frac{\partial \bar{P}}{\partial t} &= -i\delta_{ac}\bar{P} - \frac{iN\mu_{12}^2}{\hbar}\bar{F}\bar{D} - \gamma_{\perp}\bar{P}, \\
\frac{\partial \bar{D}}{\partial t} &= \frac{-2i}{N\hbar}\left[\bar{F}\bar{P}^* - \bar{F}^*\bar{P}\right] - \gamma_{\|}\left[\bar{D} - \bar{D}_o\right].
\end{aligned}$$

Note that we have defined the atomic detuning $\delta_{ac} = \omega_a - \omega_c$. We now perform some rescaling of the equations to get them into a more manageable and dimensionless form. Defining new variables, F, R, and D as

$$\begin{aligned}
\bar{F} &= \frac{\hbar(\gamma_{\|}\gamma_{\perp})^{1/2}}{2\mu_{12}} F e^{i(\omega_c - \omega_l)t} \\
\bar{P} &= \frac{-iN\mu_{12}}{2}\left(\frac{\gamma_{\|}}{\gamma_{\perp}}\right)^{1/2} R e^{i(\omega_c - \omega_l)t} \\
\bar{D} &= D
\end{aligned}$$

gives

$$\begin{aligned}
\nabla_T^2 F &+ 2ik\frac{\partial F}{\partial z} + \frac{2ik}{c}\frac{\partial F}{\partial t} - \frac{2\delta_{cl}k}{c}F = 2igkR \\
\frac{\partial R}{\partial t} &= -i\delta_{al}R + \gamma_{\perp}FD - \gamma_{\perp}R
\end{aligned}$$

$$\frac{\partial D}{\partial t} = -\frac{\gamma_{\|}}{2}\left[FR^* + F^*R\right] - \gamma_{\|}\left[D - D_o\right]$$

where

$$g = \frac{N\mu_{12}^2\omega_c}{2\hbar c\gamma_\perp \varepsilon_o}$$

is the amplitude gain per unit length and

$$\begin{aligned} \delta_{al} &= \omega_a - \omega_l, \\ \delta_{cl} &= \omega_c - \omega_l \end{aligned}$$

are defined in terms of the frequency, ω_l, at which the laser field is oscillating. It does not matter at this stage that we do not know this frequency.

A.4 Mean-field limit in a ring cavity

In their 'raw' format, the Maxwell-Bloch equations given above are very complicated. They are partial differential equations describing the evolution of the electric field and the material polarisation and population inversion as functions of three space coordinates, (x, y, z) and time. In most cases, such complication is beyond the scope of current analysis techniques and is too complicated for numerical simulation in a reasonable time. We obviously need to make some simplifying approximations. One we might consider immediately would be to assume that the variables are uniform in the transverse plane, reducing the dimensionality of the problem by two(!) but, since we hope to study pattern formation in just this plane, such an approximation is not too appropriate!

Another approximation which is valid in a large number of optical systems is the *mean-field limit*[27, 2]. This assumes that the dependence on the propagation direction, z, has little effect on its transverse behaviour. This is true when the field changes only very slowly along the z-direction, and can usually be applied in high finesse cavities. In this section we will derive the mean-field limit to remove the z-dependence in the

Maxwell-Bloch equations.

Consider a ring cavity almost completely filled with a laser gain medium, as shown in figure A.3.

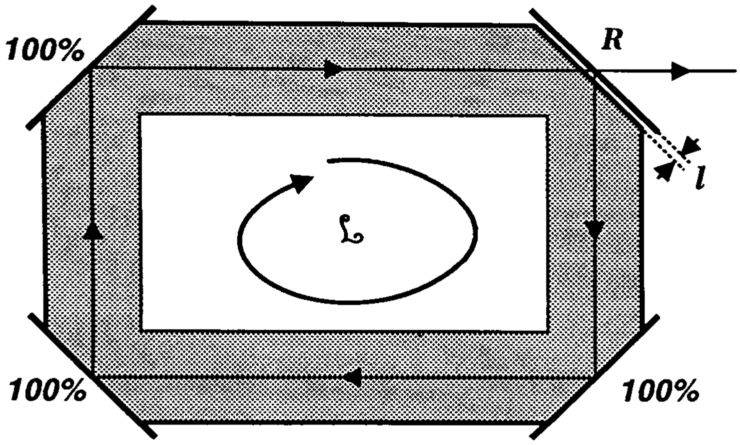

Figure A.3: A ring cavity of length $\mathcal{L}$, almost filled with gain medium of length $L = \mathcal{L} - l$. Three of the mirrors have 100% reflectivity and the fourth has intensity reflectivity, $\mathcal{R}$, close to 100%.

We assume that the longitudinal coordinate, z, has its origin at the entrance to the gain medium, just after the small empty length l. The longitudinal boundary condition for the field is

$$F(x, y, z = \mathcal{L}, t) = F(x, y, z = 0, t) \tag{A.33}$$

because the positions $z = 0$ and $z = \mathcal{L}$ are equivalent in the cavity. We now write

$$F(x, y, z = \mathcal{L}, t) = F(x, y, z = L, t - l/c)\mathcal{R}^{1/2} e^{ikl - i\delta_{cl} l/c}$$

and if we assume that $l \to 0$ so that the field amplitude does not change over the distance l we can recast the boundary condition (A.33) as

$$F(x, y, 0, t) = F(x, y, L, t)\mathcal{R}^{1/2}.$$

We now make a change of variables, effectively distributing the losses throughout the cavity, so that the boundary conditions become periodic in the longitudinal coordinate,

$$\begin{aligned} \tilde{F} &= \exp\left[\frac{z}{2L}\ln\mathcal{R}\right]F, \\ \tilde{R} &= \exp\left[\frac{z}{2L}\ln\mathcal{R}\right]R, \\ \tilde{D} &= D. \end{aligned}$$

We substitute these into the Maxwell-Bloch equations to give

$$\begin{aligned} \nabla_T^2\tilde{F} &- \frac{2ik\ln\mathcal{R}}{2L}\tilde{F} + 2ik\frac{\partial\tilde{F}}{\partial z} + \frac{2ik}{c}\frac{\partial\tilde{F}}{\partial t} - \frac{2\delta_{cl}k}{c}\tilde{F} = 2igk\tilde{R}, \\ \frac{\partial\tilde{R}}{\partial t} &= -(\gamma_\perp + i\delta_{al})\tilde{R} + \gamma_\perp\tilde{F}\tilde{D}, \\ \frac{\partial\tilde{D}}{\partial t} &= -\frac{\gamma_\parallel}{2}\left[\tilde{F}\tilde{R}^* + \tilde{F}^*\tilde{R}\right]\exp\left[\frac{-z}{L}\ln\mathcal{R}\right] - \gamma_\parallel\left[\tilde{D} - \tilde{D}_o\right]. \end{aligned}$$

At this stage we make the mean-field limit. We want to be able to neglect the term involving $\partial/\partial z$ in the field equation and therefore to say that the variables are independent of the longitudinal coordinate[2]. In order to make this approximation we need to say that the other terms in the field equation only give very small contributions to $\partial/\partial z$. We quantify this in terms of a *smallness parameter*, the mirror transmittivity, $T = 1 - \mathcal{R} \approx -\ln\mathcal{R}$,

$$\begin{aligned} T &\ll 1, \\ gL \sim \mathcal{O}(T) &\ll 1, \\ \delta_{cl} &\ll c/L, \\ \frac{LK^2}{k} &\ll 1. \end{aligned}$$

What do these assumptions mean physically? The transmittivity, $T \ll 1$, means that the cavity losses must be small. This is obviously a necessary requirement for having the field changing slowly in z. The gain per pass, $gL \ll 1$, is the same condition but for the gain. The third and fourth conditions are linked. The third is

---

[2] *Note that we say this for the rescaled variables $\tilde{F}$, $\tilde{R}$ and $\tilde{D}$, so we have accounted for the cavity losses.*

that the laser field must have a frequency close to that of the nearest longitudinal cavity mode. If this detuning becomes close to the free spectral range, then the field's phase will change appreciably over the cavity length. The fourth condition is similar, but restricts the size of the transverse cavity wavevectors, K, which can be excited. Large transverse wavevectors have large frequency shifts with respect to plane wave fields and we have seen that as soon as these frequency shifts become comparable to the free spectral range then the mean field assumptions are invalidated.

Given these assumptions, the mean field equations for the ring cavity are

$$\begin{aligned}
\nabla_T^2 \tilde{F} &+ \frac{ikT}{L}\tilde{F} + \frac{2ik}{c}\frac{\partial \tilde{F}}{\partial t} - \frac{2\delta_{cl}k}{c}\tilde{F} = 2igk\tilde{R}, && \text{(A.34)}\\
\frac{\partial \tilde{R}}{\partial t} &= -(\gamma_\perp + i\delta_{al})\tilde{R} + \gamma_\perp \tilde{F}\tilde{D}, && \text{(A.35)}\\
\frac{\partial \tilde{D}}{\partial t} &= -\frac{\gamma_\parallel}{2}\left[\tilde{F}\tilde{R}^* + \tilde{F}^*\tilde{R}\right] - \gamma_\parallel \left[\tilde{D} - \tilde{D}_o\right]. && \text{(A.36)}
\end{aligned}$$

A.5 Mean-field limit in a Fabry-Perot cavity

The microchip lasers discussed in chapter 2 use a Fabry-Perot cavity, rather than a ring. In such a cavity, the fields counterpropagate, generating standing waves and for a laser this causes a longitudinal modulation of the population inversion through the process of *spatial hole-burning*. These variations are on the scale of the wavelength and such fast variations readily invalidate the mean field approximations made above. All is not lost because the mean-field limit can be rescued if we assume that some diffusion process is present in the gain medium to 'wash out' this grating in the population inversion. In gas lasers this is justifiable but for lasers using solid state materials, such as microchip lasers, there exists no such diffusion process. This leaves us with somewhat of a problem.

Haelterman *et al.*[51], for a Kerr medium in a mean-field Fabry-Perot cavity, derived a model equation using a technique developed for a nonlinear prism coupler and based on a pole analysis. Their equation is identical to one derived in a ring cavity by applying the mean-field limit. This is the first evidence for why we expect the Fabry-Perot cavity to be modelled by the same equation as a ring. Note that, since this system is a passive one, the comparisons are not directly applicable to the laser. Work by Lugiato *et al.*[27, 52] has shown similar results.

Our second piece of evidence comes from the experiments on microchip lasers. The approximations made basically mean that the laser field should change slowly with the longitudinal coordinate. If it doesn't, that is if the mean-field limit isn't working, then how is such a rapidly changing field seen in the laser output? The answer is that the laser operates on a number of longitudinal modes. This is not observed for these microchip lasers and so this can be seen as some evidence for the validity of the mean-field limit in their description.

Appendix B

Modes of Empty Cavities

Consider an arrangement of curved cavity mirrors, with radius of curvature, R_o, separated by a distance, L, as shown in figure B.1.

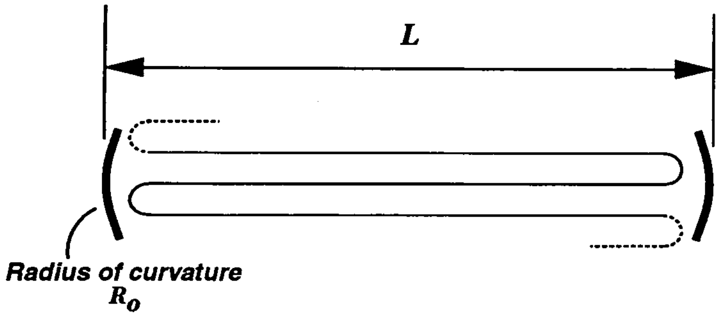

Figure B.1: An arrangement of perfectly reflecting, curved mirrors forming an optical cavity.

What do we mean by the *modes* of this cavity? We define them to be field distributions which, on propagating once round the cavity, are unchanged other than by a phase shift. If this phase shift is arranged to be an integer multiple of 2π, then the field after one roundtrip will positively reinforce itself leading to a *resonance*. This is why cavity modes are sometimes referred to as cavity resonances. Note that some arrangements of mirrors cannot lead to the localisation of the optical field into such modes - for example, a cavity formed from convex mirrors. For stable cavities, there exists a discrete set of cavity modes and it is these modes and their resonant frequencies we would like to find in this section.

Consider the paraxial wave equation already derived in appendix A as equation (A.19),

$$\nabla_T^2 \bar{F} + 2ik\frac{\partial \bar{F}}{\partial z} + \frac{2ik}{c}\frac{\partial \bar{F}}{\partial t} = -\mu_o \omega_c^2 \bar{P}. \tag{B.1}$$

This equation describes the evolution of the complex field amplitude, $\bar{F}$ in the presence of a material polarisation, $\bar{P}$. Let's consider this equation for propagation in free space, ($\bar{P} = 0$). Transforming the equation into a reference frame moving at the speed of light, c,

$$\frac{\partial}{\partial z} + \frac{1}{c}\frac{\partial}{\partial t} \rightarrow \frac{\partial}{\partial \xi},$$

gives

$$\nabla_T^2 \bar{F} + 2ik\frac{\partial \bar{F}}{\partial \xi} = 0.$$

It can be shown[53] that this equation has solutions of Gauss-Laguerre form

$$\begin{aligned} \bar{F} &= \bar{F}_o \frac{w_o}{w(\xi)}\left(\frac{2r^2}{w^2(\xi)}\right)^{\frac{|m|}{2}} L_p^{|m|}\left(\frac{2r^2}{w^2(\xi)}\right) \\ &\times \exp\left(\frac{-r^2}{w^2(\xi)} - \frac{ikr^2}{2R(\xi)} - ik\xi + i(2p+|m|+1)\eta\right)e^{im\phi}, \end{aligned} \tag{B.2}$$

parameterised by

$$\begin{aligned} w(\xi) &= w_o\sqrt{1+\xi^2/\xi_o^2}, \\ R(\xi) &= \xi\left(1+\xi_o^2/\xi^2\right), \\ \eta(\xi) &= \tan^{-1}(\xi/\xi_o), \\ \xi_o &= w_o^2 k/2, \end{aligned}$$

and by the mode indices (p, m). These parameters are depicted in figure B.2 and explained in the following paragraph. The parameter $w(\xi)$ is the width of the fundamental Gaussian transverse envelope - also known as the *spot size* - at any point along the propagation direction, ξ. It measures the distance in the transverse plane at which the field intensity is $1/2e$ times smaller than at beam centre. The parameter w_o is the minimum spot size, that is $w_o = w(\xi = 0)$. The parameter, ξ_o, is known as the *Rayleigh range* and is the propagation distance at which the beam has diffracted so that its spot size is double its initial value. The parameter $R(\xi)$ is the curvature of the parabolic phase fronts ; they are parabolic only as a consequence of the paraxial approximation and in actual fact they should be spherical. The distinction is unimportant since we will only consider fields close to the optical axis, where a sphere is approximated very well by a parabola. The parameter, $\eta(\xi)$, is a phase shift induced by the transverse confinement of the field. Notice that this contribution vanishes in the plane wave limit, $w_o \to \infty$. We have seen, in equation (B.2) and in figure B.2, how these solutions vary in ξ, and how their transverse width changes but what effect do the transverse mode indices, p and m, have on their shape? Consider, for the moment, the shape of the solutions at $\xi = 0$

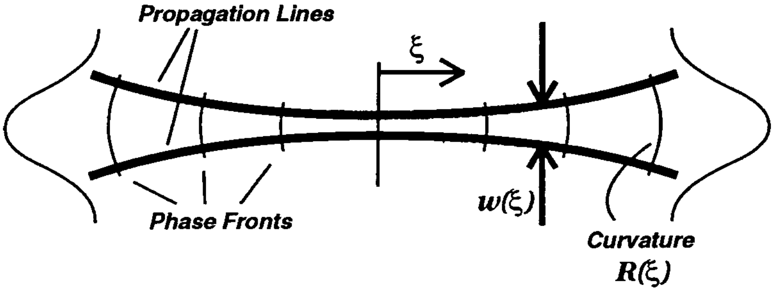

Figure B.2: A Gaussian beam propagating in free space according to the paraxial wave equation.

$$\bar{F} = \bar{F}_o \left(\frac{2r^2}{w_o^2}\right)^{\frac{|m|}{2}} L_p^{|m|}\left(\frac{2r^2}{w_o^2}\right)\exp\left(\frac{-r^2}{w_o^2}\right)e^{im\phi}. \qquad \text{(B.3)}$$

These are *Gauss-Laguerre* functions, so named because they are a product of a Gaussian and a Laguerre polynomial, $L_p^{|m|}(x)$. The first few Laguerre polynomials are as follows

$$\begin{aligned} L_0^0(x) &= 1 \\ L_0^1(x) &= 1 \\ L_1^0(x) &= 1 - x \end{aligned}$$

$$\begin{aligned} L_1^1(x) &= 2 - x \\ L_1^2(x) &= 3 - x \\ L_2^0(x) &= 1 - 2x + x^2/2 \\ L_2^1(x) &= 3 - 3x + x^2/2 \end{aligned}$$

and, in general, they are defined

$$L_p^{|m|}(x) = \sum_{n=0}^{p} \frac{(-1)^n}{n!} \begin{pmatrix} p + |m| \\ p - n \end{pmatrix} x^n.$$

Figure B.3 shows the transverse profiles of the first few Gauss-Laguerre functions. The mode index, p, gives the number of zeros of the amplitude in the radial direction and the index, m, gives the number of zeros in the azimuthal direction.

We hope to find the *modes* of the cavity shown in figure B.1. Note that the following analyses can be performed, almost as easily, in cavities with more mirrors, all with different radius of curvature if necessary. For simplicity, in this section, we will consider only the symmetric cavity shown.

We consider first the *longitudinal modes* of the cavity. Such modes are familiar even to high school physics students in the context of vibrating strings fixed at each end. The example of a guitar string is often used and we will use it to illustrate the main principles. The vibrations of the guitar string are analogous to the electric field 'vibrations' in the cavity and the fixing of the guitar strings at the bridge and on the fretboard correspond to the boundary conditions imposed on the field at the cavity mirrors. These boundary conditions force the string to oscillate only at distinct frequencies - a real boon for the guitar player! In fact, twice the string length must be an integer multiple of the wavelength. In a guitar, the sound produced is a superposition of the lowest possible frequency (the fundamental) and integer multiples (harmonics) of it. In a laser cavity, however, because of the very short wavelength of laser light compared with typical cavity lengths, the harmonics excited are of very high order.

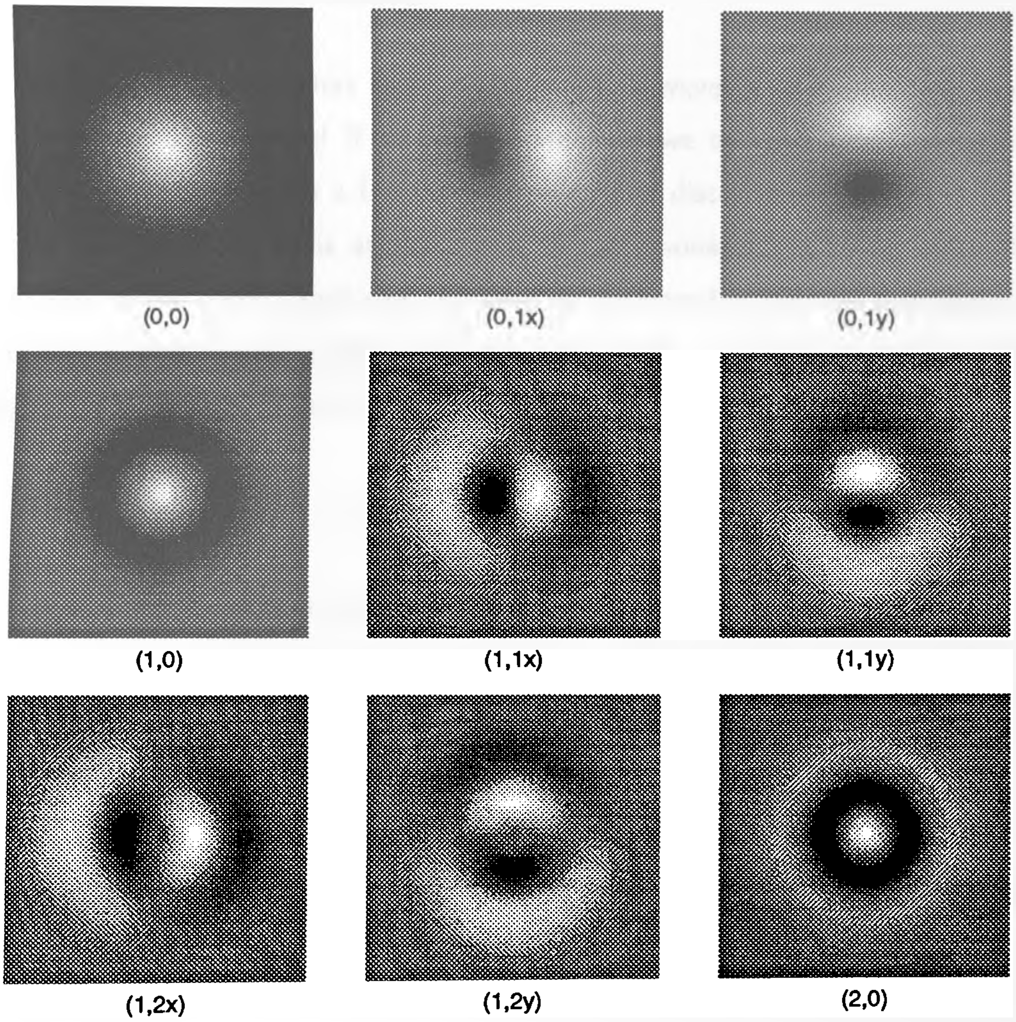

(0,0) (0,1x) (0,1y)

(1,0) (1,1x) (1,1y)

(1,2x) (1,2y) (2,0)

Figure B.3: Transverse profiles for the first nine Gauss-Laguerre modes.

Writing all this down a little more mathematically, the longitudinal mode frequencies are

$$\omega_q = \frac{\pi c q}{L}$$

where q is the longitudinal mode index (the 'harmonic' in the case of the guitar string) which is usually a very large number.

This mode analysis so far has been based on plane wave fields in the cavity. Are the frequencies shifted, and if so by how much, if we consider other cavity field distributions? Let's consider a Laguerre Gaussian field distribution like that in (B.2), with the origin of the ξ-axis at the centre of the resonator. If we choose a field distribution of the correct spot size, w_o, then by the time the field has propagated to one of the mirrors its phase front curvature will exactly match the curvature of the cavity mirrors. That is to say that $R(\xi = L/2) = R_o$, implying

$$\frac{L}{2}\left(1 + \frac{\xi_o^2}{(L/2)^2}\right) = R_o$$

which gives the condition on the Rayleigh range,

$$\xi_o^2 = \left(\frac{2R_o}{L} - 1\right)(L/2)^2, \tag{B.4}$$

and therefore on the spot size at $\xi = 0$,

$$w_o^4 = (2R_oL - L^2)/k^2. \tag{B.5}$$

We want to obtain the cavity resonances for these Gauss-Laguerre functions. To do this we consider the definition of frequency,

$$\omega = \frac{d\varphi}{dt},$$

as a change in phase over one cavity roundtrip divided by the roundtrip time. Let's consider, firstly, how the phase of a Gauss-Laguerre function, (B.2), is affected by propagation once round the cavity. In going from the centre of the cavity to one mirror the phase shift is

$$\varphi = kL/2 + (2p + |m| + 1)\tan^{-1}\left(\frac{L/2}{\xi_o}\right)$$

which, on substituting the Rayleigh range for the matched mode, (B.4), and multiplying by 4 to obtain the phase shift for a full cavity roundtrip, becomes

$$\varphi = 2kL + 4(2p + |m| + 1)\tan^{-1}\left(\frac{1}{\sqrt{2R_o/L - 1}}\right).$$

The first term, $2kL$, is the phase shift felt by a plane wave in the cavity, the one we have already considered. The second term is the correction due to the Gauss-Laguerre nature of the field.

Dividing by the cavity roundtrip time, $t_R = 2L/c$, allows us to compute the resonant frequencies

$$\omega_{q,p,m} = \frac{\pi c q}{L} + \frac{2c}{L}(2p + |m| + 1)\tan^{-1}\left(\frac{1}{\sqrt{2R_o/L - 1}}\right), \tag{B.6}$$

where we have written $q = 2L/\lambda$.

Having derived the mode resonance frequencies let us now look at some typical cavities as examples.

1) In a *confocal cavity,*

$$R_o = L$$

which gives the following expression for the resonant frequencies

$$\omega_{q,p,m} = \frac{\pi c}{2L}(2q + (2p + |m| + 1)). \tag{B.7}$$

Figure B.4 shows the frequencies of the modes given by the indices q, p, m. It is interesting in this case to compute the beam waist of the cavity modes at the mirrors, w_{mirror}. Using the expressions already obtained for the matched mode we obtain

$$w^2_{mirror} = w^2(\xi = L/2) = \frac{2R_o}{k}\frac{1}{\sqrt{2R_o/L - 1}},$$

which has a minimum value when $R_o = L$. This is to say that the confocal cavity is the configuration which minimises the spot size on the mirrors.

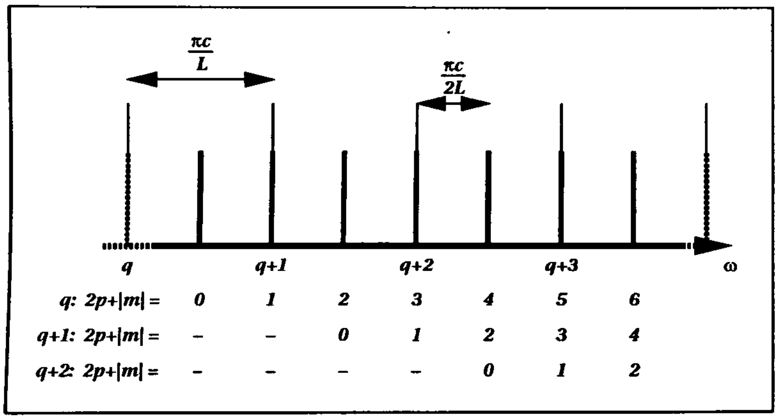

q: $2p+\|m\| =$	0	1	2	3	4	5	6
$q+1$: $2p+\|m\| =$	-	-	0	1	2	3	4
$q+2$: $2p+\|m\| =$	-	-	-	-	0	1	2

Figure B.4: The mode frequencies for a confocal cavity as a function of the longitudinal mode index, q, and the transverse mode indices, p and m.

2) In a *concentric cavity,* as the name suggests, the centres of curvature of the mirrors are coincident and so

$$R_o = L/2.$$

The expression for the matched beam waist, (B.5), shows that the waist should shrink to zero size. This is not physical and indicates that this cavity does not permit a confined mode.

3) In a near planar cavity, $R_o \gg L$, the expressions for the resonant frequencies are

$$\omega_{q,p,m} = \frac{\pi c q}{L} + \frac{2ac}{L}(2p + |m| + 1),$$

where we have defined the factor $a = \tan^{-1}\left(\frac{1}{\sqrt{2R_o/L-1}}\right)$, which is determined solely by the cavity geometry. Figure B.5 shows the frequencies of the modes given by the indices q, p, m. Note that the transverse modes all lie to the right of the longitudinal mode resonance and that as the mirrors become flatter, the transverse mode separation tends to zero so that, in the limit, of a planar cavity the transverse modes are degenerate.

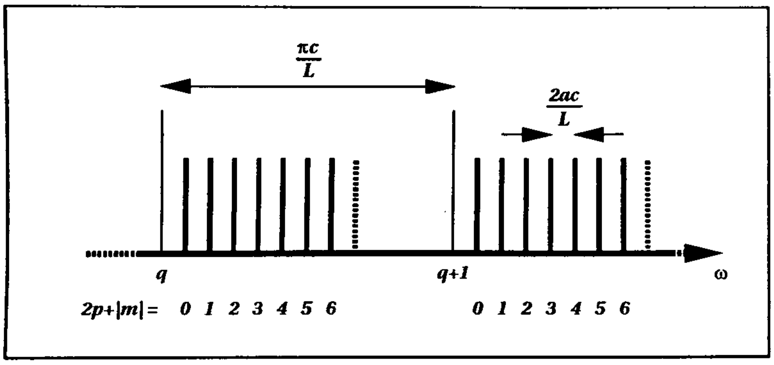

Figure B.5: The mode frequencies for a near planar cavity as a function of the longitudinal mode index, q, and the transverse mode indices, p and m. In the limit of the mirrors becoming perfectly flat, the transverse modes become degenerate.

The planar cavity and the concentric cavity mark the boundaries for cavity stability. A cavity supports transverse modes if and only if the condition

$$L/2 < R_o < \infty$$

is met. Unstable optical resonators, that is ones which do not meet this condition, are sometimes used in laser systems[53] for certain applications but we will not consider resonators of this type.

Appendix C

Numerical Methods

It seems to be the case in science that the equations we derive to model all but the simplest of physical phenomena are much too complicated for the techniques of analysis of the day. This is probably a good thing in that it drives us to come up with innovative and novel methods!

This is true in optics as much as in any other branch of science. Take the example of the Maxwell-Bloch equations we derived in appendix A. The raw equations are far too complicated to be tackled and so we made a mean-field assumption to eliminate the dependence on one of the space dimensions. Even after doing this, the equations are too complicated to be solved exactly and, in chapter 3, we resorted to the derivation of amplitude equations guided by the linear analysis of the problem. This further restricted the applicability of the results we obtained.

The study of a set of equations can often be aided by a computer[1]. In most cases, by using numerical methods we can tackle more complicated problems than we can analytically and so the computer becomes a useful tool in the analysis of physical models and of the approximations we make on them. To take full advantage of the computer in this way requires the development of efficient and accurate numerical

---

[1] *Some would, of course, argue with this point saying that computers are more bother than they are worth.*

methods. In this appendix, we describe such a method, useful for the numerical solution of a class of partial differential equations (pde's) often found in optics. It is called the *split-step Fourier method.*

We consider a pde of the form[6]

$$\frac{\partial \mathbf{u}}{\partial t} = \left(\hat{\mathcal{L}} + \hat{\mathcal{N}}(t)\right) \mathbf{u} \tag{C.1}$$

where $\hat{\mathcal{L}}$ is some linear operator and $\hat{\mathcal{N}}$ is some nonlinear operator, perhaps time dependent.

Given an initial condition $\mathbf{u}(t)$ at time t we can solve this equation, at least formally, to obtain the solution at some advanced time $t + \Delta t$,

$$\mathbf{u}(t + \Delta t) = \exp\left(\Delta t \hat{\mathcal{L}} + \int_t^{t+\Delta t} \hat{\mathcal{N}}(t')dt'\right) \mathbf{u}(t). \tag{C.2}$$

We now consider expanding the exponential operator in the above expression as

$$\exp\left(\Delta t \hat{\mathcal{L}} + \int_t^{t+\Delta t} \hat{\mathcal{N}}(t')dt'\right) \approx \exp(\hat{\mathcal{L}}\Delta t)\exp(\hat{\mathcal{P}}(t))$$

where we have defined the operator,

$$\hat{\mathcal{P}}(t) = \int_t^{t+\Delta t} \hat{\mathcal{N}}(t')dt'.$$

Note that, for operators, this expansion is not necessarly exact as it is for numbers. The leading term in the error introduced is related to the commutator of the operators

$$\varepsilon \approx \frac{(\Delta t)^2}{2} \left[\hat{\mathcal{L}}, \hat{\mathcal{P}}(t)\right].$$

This means that we obtain a solution which is accurate to $\mathcal{O}(\Delta t)$ and if we choose Δt appropriately we can obtain results to arbitrary accuracy. This may take some time of course because a small Δt means we may have to evaluate the operators many times to obtain the solution at times $t \sim \mathcal{O}(1)$.

A clever idea is to expand the exponential operator in equation (C.2) in a different way,

$$\exp\left(\Delta t\hat{\mathcal{L}} + \int_t^{t+\Delta t} \hat{\mathcal{N}}(t')dt'\right) \approx \exp(\hat{\mathcal{L}}\Delta t/2)\exp(\hat{\mathcal{P}}(t))\exp(\hat{\mathcal{L}}\Delta t/2), \qquad \text{(C.3)}$$

and it can be shown that, by this method, we obtain results which are accurate to $\mathcal{O}(\Delta t^2)$. This allows us to make Δt bigger and still obtain the same accuracy – obviously an advantage!

Let's now remove some of the generality and consider the case of the complex Lorenz equations (3.1) – (3.3). We will take $\mathbf{u} = (e, p, n)^T$, $\hat{\mathcal{L}} = ia\nabla_T^2$ and $\hat{\mathcal{P}}$ to contain everything else. The solution one time step Δt on is now given by the three consecutive parts in equation (C.3),

$$\mathbf{u}(t + \Delta t) = \exp(ia\nabla_T^2\Delta t/2)\exp(\hat{\mathcal{P}}(t))\exp(ia\nabla_T^2\Delta t/2)\mathbf{u}(t). \qquad \text{(C.4)}$$

The beauty of the split-step method for this type of equation is that the first and third parts, those involving $\exp(\nabla_T^2)$, can be solved in a trivial way by using a Fourier transform. As an example, the equation

$$\frac{\partial E}{\partial t} = ia\nabla_T^2 E$$

has formal solution

$$E(t) = \exp(ia\nabla_T^2 t)E(0)$$

which, in Fourier space, becomes

$$\tilde{E}(t) = \tilde{E}(0)\exp(-iak^2 t).$$

Consider now the second part of scheme (C.4), that involving the operator $\hat{\mathcal{P}}(t)$. The operator involves an integral over the time interval and so makes the scheme implicit. We overcome this by replacing $\hat{\mathcal{P}}(t) \approx \hat{\mathcal{N}}(t)\Delta t$ which is the same as assuming that the nonlinear operator does not change appreciably over the time step Δt. For the

Lorenz system, we notice that the operator $\hat{\mathcal{P}}$ is independent of space – all the space dependence is wrapped up in the $\hat{\mathcal{L}}$ operator. This means that the second part in equation (C.4) is an infinite set of *decoupled* ordinary differential equations (ode's) and there are a host of numerical routines specifically designed to integrate these[25]. On a computer we must discretise the transverse plane and so this infinite set will become finite in number.

Given these things we are left with the following scheme to advance the variables of the Lorenz system forward in time

$$\mathbf{u}(t+\Delta t) = (\widehat{FFT})^{-1}\left[e^{-iak^2\Delta t/2}\;(\widehat{FFT})\left[e^{\Delta t\hat{\mathcal{N}}}\;(\widehat{FFT})^{-1}\left[e^{-iak^2\Delta t/2}\;(\widehat{FFT})\,[\mathbf{u}(t)]\right]\right]\right].$$

The operator $(\widehat{FFT})$ represents the *Fast Fourier Transform.*

As an example of this method, hopefully less mathematical looking, we write an algorithm for advancing the variables of the complex Lorenz equations on by one time step Δt.

1. Take the Fourier transform of the field e using an FFT package,
2. Multiply through by the phase factor $\exp(-iak^2\Delta t/2)$,
3. Take the inverse Fourier transform of e,
4. Treat the variables e, p and n at each grid point as the initial conditions for an ode package to integrate the nonlinear terms over a time interval Δt,
5. Take the Fourier transform of the field e using an FFT package,
6. Multiply through by the phase factor $\exp(-iak^2\Delta t/2)$,
7. Take the inverse Fourier transform.

Note that if this procedure is being repeated a number of times the steps 5,6,7,1,2,3 can be replaced by doing the FFT, multiplying by the phase factor twice, that is multiplying by $\exp(-iak^2\Delta t)$, and then doing the inverse FFT. This saves doing two FFT's, reducing computational overheads by about half.

It is well known that in most explicit finite difference schemes, the stability of the method dictates that the time step be made smaller than some value depending on the space step. Is this also the case for this method? The answer is yes and it is much easier to see why in this method than in most. For the complex Lorenz equations we will study, the condition comes from the steps used to evaluate the effect of the diffraction operator. In these steps we multiply the field in Fourier space by the complex exponential $\exp(-iak^2\Delta t)$. This exponential function is periodic in the interval $[0, 2\pi)$ and so if Δt is big enough to invalidate the condition

$$ak_{max}^2\Delta t < \pi$$

then this leads to aliasing of Fourier modes with magnitude greater than k_{max}. The Fourier mode of largest wavevector on a periodic grid with space step Δx is that with $k_{max} = \pi/\Delta x$..

What about transverse boundary conditions? Due to the fact that the FFT works in a periodic domain, the method is automatically set up for periodic transverse boundary conditions. Other conditions where the field is zero on a square or ones where the normal derivative of the field is zero can also be handled by replacing the FFT by a *Fast Sine* or *Cosine Transform*[25]. Boundary conditions on other shape domains can be imposed by handling them in the nonlinear step rather than in the propagation one. For the laser, the process is equivalent to having an absorber of infinite 'absorbing power' outside the region of interest. This is the way we have handled the zero boundary conditions on a circle in the simulations presented in this thesis. At each nonlinear step we simply set the field to zero outside the circle. This method is more difficult to justify in a rigorous way but we have checked its results by using it to integrate on a square domain and comparing the results with those using the sine transform.

Bibliography

[1] A. E. Siegman, *Lasers* (Oxford University Press, Oxford, 1986).

[2] L. A. Lugiato *et al.*, *"Instabilities and spatial complexity in a laser"*, J. Opt. Soc. Am. B, Vol. **7**, No. 6, pp.1019–33 (1990).

[3] A. B. Coates *et al.*, *"Dynamical transverse laser patterns. II. Experiments"*, Phys. Rev. A, Vol. **49**, No. 2, pp.1452–1466 (1994).

[4] M. Brambilla *et al.*, *"Dynamical transverse laser patterns. I. Theory"*, Phys. Rev. A, Vol. **49**, No. 2, pp.1427–1451 (1994).

[5] G.-L. Oppo, G. D'Alessandro, and W. J. Firth, *"Spatiotemporal instabilities of lasers in models reduced via center manifold techniques"*, Phys. Rev. A, Vol. **44**, No. 7, pp.4712–20 (1991).

[6] J. V. Moloney and A. C. Newell, *Nonlinear Optics* (Addison-Wesley, Redwood City, CA, 1991).

[7] M. C. Cross and P. C. Hohenberg, *"Pattern formation outside of equilibrium"*, Rev. Mod. Phys., Vol. **65**, p.851 (1993).

[8] A. C. Newell, T. Passot, and J. Lega, *"Order parameter equations for patterns"*, Annu. Rev. Fluid Mech., Vol. **25**, p.399 (1993).

[9] P. K. Jakobsen, J. V. Moloney, A. C. Newell, and R. Indik, *"Space-time dynamics of wide-gain-section lasers"*, Phys. Rev. A, Vol. **45**, No. 11, pp.8129–8137 (1992).

[10] P. Manneville, *Dissipative structure and weak turbulence* (Academic Press, San Diego, U.S.A., 1990).

[11] H. Kogelnik, "*On the propagation of Gaussian beams of light through lenslike media including those with a loss or gain variation*", Am J. Phys., Vol. **4**, No. 12, pp.1562–9 (1965).

[12] W. J. Firth, "*Propagation of laser beams through inhomogeneous media*", Opt. Comm., Vol. **22**, No. 2, pp.226–30 (1977).

[13] J. J. Zayhowski and A. Mooradian, "*Single-frequency microchip Nd lasers*", Opt. Lett., Vol. **14**, No. 1, pp.24–26 (1989).

[14] J. J. Zayhowski and A. Mooradian, "*Frequency-modulated Nd:YAG microchip lasers*", Opt. Lett., Vol. **14**, No. 12, pp.618–620 (1989).

[15] J. J. Zayhowski, J. Ochoa, and A. Mooradian, "*Gain-switched pulsed operation of microchip lasers*", Opt. Lett., Vol. **14**, No. 23, pp.1318–1320 (1989).

[16] J. J. Zayhowski, "*Polarization-switchable microchip lasers*", Appl. Phys. Lett., Vol. **58**, No. 24, pp.2746–2748 (1991).

[17] F. Zhou and A. I. Ferguson, "*Tunable single frequency operation of a diode laser pumped Nd:YAG microchip at* $1.3\mu m$", Elect. Lett., Vol. **26**, No. 7, p.490 (1990).

[18] N. MacKinnon and B. D. Sinclair, "*Pump power induced cavity stability in lithium neodymium tetraphosphate (LNP) microchip lasers*", Opt. Comm., Vol. **94**, pp.281–288 (1992).

[19] N. MacKinnon and B. D. Sinclair, "*A laser diode array pumped, ND:YVO*$_4$*/KTP, composite material microchip laser*", Optics Comm., Vol. **105**, pp.183–187 (1994).

[20] J. J. Zayhowski, in *Advanced Solid State Lasers* (OSA Proceedings Series, Optical Society of America, Washington, D.C., 1991), Vol. 10, p.265.

[21] W. J. Firth, B. S. Wherrett, and D. Weaire, "*Theory of spin-flip laser modes - I: Threshold modulation and tuning behaviour*", IEEE J. Quantum Electronics, Vol. **12**, No. 4, pp.218–225 (1976).

[22] W. J. Firth, L. C. Simmons, D. L. Weaire, and B. S. Wherrett, "*Theory of spin-flip laser modes - II: higher modes and saturation effects*", IEEE J. Quantum Electronics, Vol. **QE-14**, No. 7, pp.517–26 (1978).

[23] S. Longhi, "*Theory of transverse modes in end-pumped microchip lasers*", JOSA B, Vol. **11**, No. 6, pp.1098–1107 (1994).

[24] E. Kreyszig, *Advanced Engineering Mathematics* (John Wiley and Sons, Inc., New York, 1988).

[25] W. H. Press, B. P. Flannery, S. A. Teukolsky, and W. T. Vetterling, *Numerical Recipes: The Art of Scientific Computing* (Cambridge University Press, Cambridge, 1986).

[26] L. Gil, Ph.D. thesis, University of Nice, 1988.

[27] L. A. Lugiato and C. Oldano, "*Stationary spatial patterns in passive optical systems—2-level atoms*", Phys. Rev. A, Vol. **37**, No. 10, pp.3896–08 (1988).

[28] G. D'Alessandro and G.-L. Oppo, "*Gauss-Laguerre modes - a sensible basis for laser dynamics*", Opt. Comm., Vol. **88**, p.130 (1992).

[29] A. C. Newell and J. A. Whitehead, "*Finite bandwidth, finite amplitude convection*", J. Fluid Mech., Vol. **38**, pp.279–303 (1969).

[30] L. A. Segel, "*Distant sidewalls cause slow amplitude moduluation of cellular convection*", J. Fluid Mech., Vol. **38**, pp.203–224 (1969).

[31] M. Silber and E. Knobloch, "*Hopf bifurcation on a square lattice*", Nonlinearity, Vol. **4**, pp.1063–1107 (1991).

[32] M. Silber, H. Riecke, and E. Knobloch, "*Symmetry-breaking hopf bifurcation in anisotropic systems*", Physica D, Vol. **61**, No. 1–4, pp.260–278 (1992).

[33] P. LeGal, A. Pocheau, and V. Croquette, "*Square versus roll pattern at convective threshold*", Phys. Rev. Lett., Vol. **45**, No. 23, pp.2501–2504 (1985).

[34] Q. Feng, J. V. Moloney, and A. C. Newell, "*Transverse Patterns in Lasers*", preprint, Vol. (1994).

[35] M. C. Cross and A. C. Newell, "*Convection patterns in large-aspect-ratio systems*", Physica D, Vol. **10**, p.229 (1984).

[36] J. Lega, P. K. Jakobsen, J. V. Moloney, and A. C. Newell, "*Nonlinear transverse modes of large-aspect-ratio homogeneously broadened lasers: II. Pattern analysis near and beyond threshold*", Phys. Rev. A, Vol. **49**, No. 5, pp.4201–4212 (1994).

[37] Q. Feng, J. V. Moloney, and A. C. Newell, "*Amplitude instabilities of transverse traveling waves in lasers*", Phys. Rev. Lett., Vol. **71**, No. 11, pp.1705–1708 (1993).

[38] F. H. Busse, "*Nonlinear properties of thermal convection*", Rep. Prog. Phys., Vol. **41**, p.1929 (1978).

[39] W. Eckhaus, *Studies in Nonlinear Stability* (Springer Verlag, New York, 1965).

[40] P. Coullet, T. Frisch, and F. Plaza, "*Sources and sinks of wave patterns*", Physica D, Vol. **62**, pp.75–79 (1993).

[41] S. Ciliberto *et al.*, "*Defects in roll-hexagon competition*", Phys. Rev. Lett., Vol. **65**, p.2370 (1990).

[42] F. Papoff, G. D'Alessandro, G.-L. Oppo, and W. J. Firth, "*Local and global effects of boundaries on optical pattern formation in Kerr media*", Phys. Rev. A, Vol. **48**, No. 1, pp.634–641 (1933).

[43] K. D. Laakmann and W. H. Steier, "*Waveguides: characteristic modes of hollow rectangular dielectric waveguides*", Applied Optics, Vol. **15**, No. 5, pp.1334–1340 (1976).

[44] P. Coullet, L. Gil, and F. Rocca, "*Optical vortices*", Opt. Comm., Vol. **73**, p.403 (1989).

[45] B. J. Gluckman, P. Marcq, J. Bridger, and J. P. Gollub, "*Time averaging of chaotic spatiotemporal wave patterns*", Phys. Rev. Lett., Vol. **71**, No. 13, pp.2034–2037 (1993).

[46] S. Rica and E. Tirapegui, "*Dynamics of defects in the complex Ginzburg-Landau equation*", Physica D, Vol. **61**, No. 1–4, pp.246–252 (1992).

[47] L. Gil, K. Emilsson, and G.-L. Oppo, "*Dynamics of spiral waves in a spatially inhomogeneous Hopf Bifurcation*", Phys. Rev. A, Vol. **45**, No. 2, pp.567–70 (1992).

[48] A. J. Kent, Ph.D. thesis, University of Strathclyde, 1994.

[49] M. Lax, W. Louisell, and W. McKnight, "*From Maxwell to paraxial wave optics*", Phys. Rev. A, Vol. **11**, No. 4, pp.1365–1370 (1975).

[50] R. Loudon, *The Quantum Theory of Light*, 2nd ed. (OUP, Oxford, 1983).

[51] M. Haelterman, G. Vitrant, and R. Reinisch, "*Transverse effects in nonlinear planar resonators. I. Modal theory*", JOSA B, Vol. **7**, No. 7, pp.1309–1318 (1990).

[52] L. A. Lugiato and L. M. Narducci, "*Nonlinear dynamics in a Fabry-Perot resonator*", Z. Phys. B, Vol. **71**, p.129 (1988).

[53] A. Yariv, *Quantum Electronics*, 3rd ed. (John Wiley & Sons, Inc., New York, 1989).